New Jersey Institute of Technology

Digital Commons @ NJIT

8-31-2021

Advances in modeling gas adsorption in porous materials for the characterization applications

Max A. Maximov
New Jersey Institute of Technology

Recommended Citation

ABSTRACT

ADVANCES IN MODELING GAS ADSORPTION IN POROUS MATERIALS FOR THE CHARACTERIZATION APPLICATIONS

by
Max A. Maximov

The dissertation studies methods for mesoporous materials characterization using adsorption at various levels of scale and complexity. It starts with the topic introduction, necessary notations and definitions, recognized standards, and a literature review.

Synthesis of novel materials requires tailoring of the characterization methods and their thorough testing. The second chapter presents a nitrogen adsorption characterization study for silica colloidal crystals (synthetic opals). These materials have cage-like pores in the range of tens of nanometers. The adsorption model can be described within a macroscopic approach, based on the Derjaguin-Broekhoff-de Boer (DBdB) theory of capillary condensation. A kernel of theoretical isotherms is built and applied to the solution of the adsorption integral equation to derive the pore-size distribution from experimental data. The technique is validated with a surface modification of the samples so that it changes the interaction but not the pore size.

The second chapter deals with the characterization of three-dimensional ordered mesoporous (3DOm) carbons. Similar to opals, these materials have cage-like mesopores, however, these pores are connected with large windows. These windows affect the adsorption process and calculated pore-size distributions. The grand canonical Monte Carlo simulations with derived solid-fluid potentials, which take into account the 3DOm carbons geometry, confirm the critical role of interconnections, their size, and number, for correct interpretation of adsorption data for the PSD calculations.

The fourth chapter discusses a method for the pore size estimation that can serve as an alternative to the adsorption isotherms analysis. It is based on measurements of elastic properties of liquid that can be useful for the pore size estimation. A Vycor glass sample, a disordered mesoporous material with channel-like pores having a characteristic size of ca. 6-8 nm, is considered. The changes in longitudinal and shear moduli from the experimental data and molecular simulations are predicted with a near-quantitative agreement. Then, it follows by their relation of the moduli to the pore size, which is promising for characterization.

The last fifth chapter considers a promising Monte Carlo method, the Kinetic Monte Carlo (kMC) algorithm. This method is efficient for the vapor-liquid equilibrium prediction in dense regions. This chapter shows a benchmark with conventional Metropolis et al. algorithms as well as a parallelization scheme of the kMC algorithm.

ADVANCES IN MODELING GAS ADSORPTION IN POROUS MATERIALS FOR THE CHARACTERIZATION APPLICATIONS

by
Max A. Maximov

A Dissertation
Submitted to the Faculty of
New Jersey Institute of Technology
in Partial Fulfillment of the Requirements for the Degree of
Doctor of Philosophy in Chemical Engineering

Department of Chemical and Materials Engineering

August 2021

ADVANCES IN MODELING GAS ADSORPTION IN POROUS MATERIALS FOR THE CHARACTERIZATION APPLICATIONS

Max A. Maximov

Dr. Gennady Y. Gor, Dissertation Advisor   Date
Assistant Professor of Chemical Engineering, NJIT

Dr. Edward L. Dreizin, Committee Member   Date
Distinguished Professor of Chemical Engineering, NJIT

Dr. Alexei Khalizov, Committee Member   Date
Associate Professor of Chemical Engineering, NJIT

Dr. Joshua Young, Committee Member   Date
Assistant Professor of Chemical and Materials Engineering, NJIT

Dr. Christopher Rasmussen, Committee Member   Date
Senior Scientist, Zymergen, Emeryville, CA

BIOGRAPHICAL SKETCH

Author: Max A. Maximov

Degree: Doctor of Philosophy

Date: August 2021

Undergraduate and Graduate Education:

- Doctor of Philosophy in Chemical Engineering,
  New Jersey Institute of Technology, Newark, NJ, 2021

- Master of Science in Applied Math and Physics,
  St Petersburg University, St Petersburg, Russia, 2013

- Bachelor of Science in Physics,
  St Petersburg University, St Petersburg, Russia, 2011

Major: Chemical Engineering

Publications:

Maximov M. A., Molina M., and Gor G. Y., "The Effect of Interconnections on Gas Adsorption in Materials with Spherical Mesopores: a Monte Carlo Simulation Study," *The Journal of Chemical Physics*, vol. 154, 11, 114706, 2021.

Emelianova A., Maximov M. A., and Gor G. Y., "Solvation Pressure in Spherical Mesopores: Macroscopic Theory and Molecular Simulations," *AIChE Journal*, vol. 67, 3, e16542, 2020.

Maximov M. A., Galukhin A. V., and Gor G. Y., "Pore-Size Distribution of Silica Colloidal Crystals from Nitrogen Adsorption Isotherms," *Langmuir*, vol. 35, 47, 14975–14982, 2020.

Maximov M. A. and Gor G. Y., "Molecular Simulations Shed Light on Potential Uses of Ultrasound in Nitrogen Adsorption Experiments," *Langmuir*, vol. 34, 51, 15650–15657, 2018.

Dobrzanski C. D., Maximov M. A., and Gor G. Y., "Effect of Pore Geometry on the Compressibility of a Confined Simple Fluid," *The Journal of Chemical Physics*, vol. 148, 5, 054503, 2018.

Pham Q. L., Rodrigues L. N., Maximov M. A., Chandran V. D., Bi C., Chege D., Dijamco T., Stein E., Tong N. A. N., Basuray S., Voronov R. S., "Cell Sequence and Mitosis Affect Fibroblast Directional Decision-Making During Chemotaxis in Microfluidic Mazes," *Cellular and Molecular Bioengineering*, vol. 11, 6, 483–494, 2018.

Presentations:

Maximov M. A., Galukhin A. V., and Gor G. Y., "Pore-Size Distribution of Silica Colloidal Crystals from Nitrogen Adsorption Isotherms," *Oral Presentation*, AIChE Annual Meeting, online, 2020.

Maximov M. A. and Gor G. Y., "Pore-Size Estimation from Ultrasonic Measurements During Nitrogen Adsorption Experiment," *Oral and Poster Presentation*, AIChE Annual Meeting, Orlando, FL, 2019.

Maximov M. A. and Gor G. Y., "Ultrasound Propagation in Fluid-saturated Nanoporous Media," *Poster Presentation*, Transport In Disordered Environments, Princeton, NJ, 2019.

Maximov M. A. and Gor G. Y., "Molecular Simulations Shed Light on Potential Uses of Ultrasound in Nitrogen Adsorption Experiments," *Poster Presentation*, The 22nd Meeting of the North-East Corridor Zeolite Association, Philadelphia, PA, 2018.

Maximov M. A. and Gor G. Y., "Analysis of Ultrasonic Measurements During Nitrogen Adsorption Experiments," *Poster Presentation*, 1st North American Symposium on Dynamic Vapor Sorption Science, Philadelphia, PA, 2018.

Maximov M. A. and Gor G. Y., "Kinetic Monte Carlo Methods for Calculation of Fluid Phase Equilibria," *Oral Presentation*, Molecular Simulations Mini-Workshop, Newark, NJ, 2018.

Maximov M. A. and Gor G. Y., "Compressibility of Nitrogen Adsorbed in Vycor Glass," *Poster Presentation*, 8th International Workshop "Characterization of Porous Materials: From Ångströms to Millimeters", Delray Beach, FL, 2018.

Maximov M. A. and Gor G. Y., "Argon Adsorption in Three-Dimensional Ordered Mesoporous (3DOm) Carbons: Monte Carlo Molecular Simulation Study," *Poster Presentation*, Annual Meeting of the APS Mid-Atlantic Section, Newark, NJ, 2017.

To my parents, friends, and all people who helped me through life.

ACKNOWLEDGMENT

I would especially want to thank my advisor, Dr. Gennady Gor, for his help, support, and making everything possible. I express gratitude to my committee, Dr. Edward Dreizin, Dr. Alexei Khalizov, Dr. Joshua Young, and Dr. Christopher Rasmussen, for reviewing the document. Also, thanks to Dr. Robert Barat, my former committee member before his retirement, for reviewing my qualifying exam and proposal documents.

My work in 4th year was generously supported by "Molecular Dynamics Simulations of Calcium Carbonate-Arginine-Dentin System" grant from Colgate Palmolive Research Center. Travel for CPM-8 conference was supported by the National Science Foundation.

Special thanks to Andrei Galukhin for experimental collaboration on the Opals project (Chapter 2), Marcos Molina for working on 3DOm carbon simulations (Chapter 3), Alina Emelianova for her artistic talent and making fantastic graphical abstracts for my papers, Christopher Dobrzanski for his extraordinary ability to ask excellent questions during my presentations, to John Beamish for providing additional details on the ultrasonic measurements from [1] for Chapter 4. Multiple discussions during my presentations and paper review with Christopher Dobrzanski, Alina Emelianova, Ella Ivanova, Marcos Molina, Nicholas Corrente, Taylor Kvist are very much appreciated.

TABLE OF CONTENTS

LIST OF TABLES

LIST OF FIGURES

Figure   **Page**

Figure   **Page**

Figure   **Page**

CHAPTER 1

INTRODUCTION

1.1   Nanoporous Materials

Nanoporous materials, defined as porous materials with a pore size less than 100 nm [2], are important in various areas and aspects of chemical engineering and nature. They have unique features, such as a high surface area and porosity. For these reasons, they are widely used as adsorbents, catalysts, filters, and membranes; they are also used for drug delivery [3]. These materials also broaden horizons for the development of various fast response humidity sensors [4], solid natural gas storage [5], supercapacitors [6], and next-generation non-volatile memory [7, 8].

1.2   Adsorption

Adsorption is defined as the enrichment of molecules in the vicinity of an interface [2]. In the case of gas and liquid adsorption, we consider the solid-fluid interface, where the solid is called the adsorbent, and the fluid is called adsorptive or adsorbate. The amount adsorbed depends on the absolute temperature, the vapor pressure, and the fluid-fluid and solid-fluid interaction potentials, which in turn depend on the choice of adsorbent and adsorbate, adsorbent geometry (in the case of porous material, pore size), and other factors [9]. It is worth mentioning the difference between physisorption and chemisorption. The latter term includes chemical bonding of adsorbed molecules [3]. In this dissertation, chemisorption will not be considered, and the terms physisorption and adsorption will be used interchangeably. Adsorption is usually described by an isotherm, which is the amount adsorbed measured as a function of the adsorbate vapor pressure at a constant temperature. Specific plots and the features for certain materials will be shown and discussed later.

1.3   Characterization of Porous Materials

The overall surface area, pore-size distribution, geometry, and pore connectivity determine the fluid adsorption and transport [10]. Thus, the materials are routinely characterized with respect to those properties in order to determine their suitability for engineering applications. For example, materials with large channels and smaller pores in the channel walls can have a high surface area and fast transport, whereas relatively large porous materials typically have fast transport but the lower surface area, and small pores typically have a high surface area but slow transport.

To facilitate characterization, the International Union of Pure and Applied Chemistry (IUPAC) [2, 13] standardized the terminology and divided these materials into three distinct categories by pore size: microporous with the pore size less than 2 nm, mesoporous with the size between 2 and 50 nm, macroporous with the size between 50 and 1000 nm. In Figure 1.1, it is shown that the pore structure can also be ordered (e.g., silica colloid crystals [14, 15], CMK-5 [11], or three-dimensional ordered mesoporous (3DOm) carbons [16, 5]) or disordered (e.g., Vycor glass [17]). Finally, the pore geometry may fall into one of a few common types convenient to approximate:
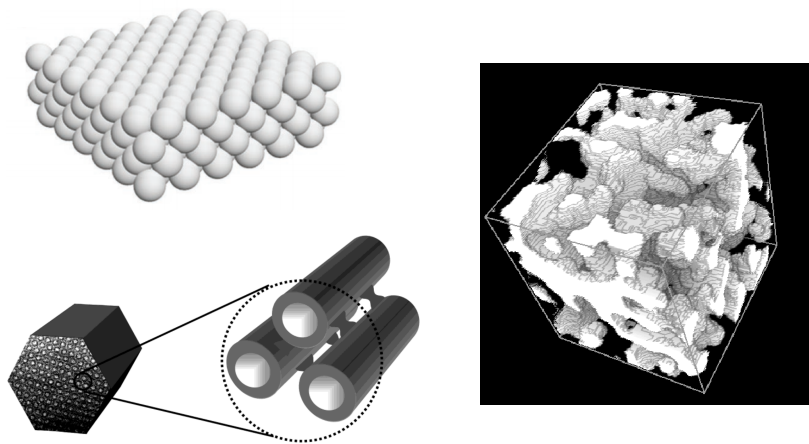
Figure 1.1 Reconstructed 3D images of ordered (left) and disordered materials (right).
Source: Top left: silica opal [4], bottom left: CMK-5 [11], right: Vycor glass [12].

spherical, cylindrical, or slit. Depending on the model one chose, the pore size, also sometimes in the literature referred to as the pore width, could be explicitly defined as the diameter for spherical and cylindrical models, and the distance between the walls in the slit model.
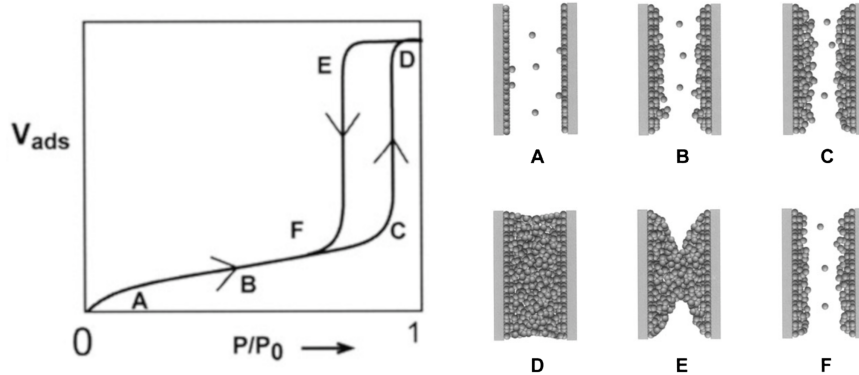
Figure 1.2   The effect of capillary condensation and evaporation in a cylindrical mesopore. As relative pressure p/p_0 goes up to saturation pressure, the corresponding adsorption isotherm (A-D) is formed, and as p/p_0 goes back, the capillary evaporation (D-F) forms a desorption isotherm (D-F). Overall, the connected A-F curve form a hysteresis loop of adsorption and desorption isotherms. Specifically, point A corresponds to an adsorbed monolayer, B to the multilayer formation, C to the critical film thickness, D is a point after the condensation, E is a receding meniscus, F is a point after the evaporation.
Source: [9].

There are many experimental methods to characterize porous materials: X-ray or neutron scattering, mercury porosimetry, scanning electron microscopy (SEM), thermoporometry, and NMR [9]. The gas adsorption technique does not have some drawbacks of SEM and small-angle X-ray diffraction. Specifically, SEM provides information only about the surface, whereas small-angle X-ray diffraction results are hard to interpret for disordered materials. A typical adsorption isotherm for a mesoporous material and its most important features are illustrated in Figure 1.2. Typically, to simplify the analysis and modeling as well as to improve the penetration in the pores, adsorption of simple gases like argon, nitrogen, and carbon dioxide is used for pore characterization. The choice to divide nanoporous materials into micro, meso,

and macro was made rather arbitrarily based on adsorption isotherm analysis. Most microporous isotherms show continuous gradual pore filling, while mesoporous show clear phase transition (capillary condensation) at $p < p_0$, and macroporous ones have the point of capillary condensation at $p \approx p_0$, where p is the equilibrium pressure, p_0 is the saturation pressure. Adsorption in micropores is mainly governed by solid-fluid interaction, whereas in mesopores, in addition to solid-fluid, the fluid-fluid interactions take an important role because of multilayer formation [9]. Representative isotherms for different systems are shown in Figure 1.3, the dependence of the point of capillary condensation on pore size is shown in Figure 1.4. Thus, even just by looking at an isotherm without a sophisticated quantitative analysis, we can often estimate the sample pore size and extract some information about the isotherm. These and other deviations can be used for characterization by comparing experimental isotherms for similar materials or from theory. In this dissertation, we are going to focus on the retrieval of the pore-size distribution using adsorption isotherms from experimental data and theoretical methods, including simulations, and propose alternative methods to extract information about the pore-size distributions.

To predict a theoretical isotherm of a certain pore size, there exist plenty of techniques: Monte Carlo methods, density functional theory (DFT), the Derjaguin-Broekhoff-de Boer (DBdB) Theory [19], etc. One of the simplest ways to estimate the mean pore size is to pick an isotherm from a series of theoretical isotherms, the kernel, by matching the points of capillary condensation. To obtain pore-size distribution, one can solve an adsorption integral equation, an approach to solve the equation and the related issues are thoroughly discussed in Chapter 2. A simplified scheme is described in Figure 1.5.
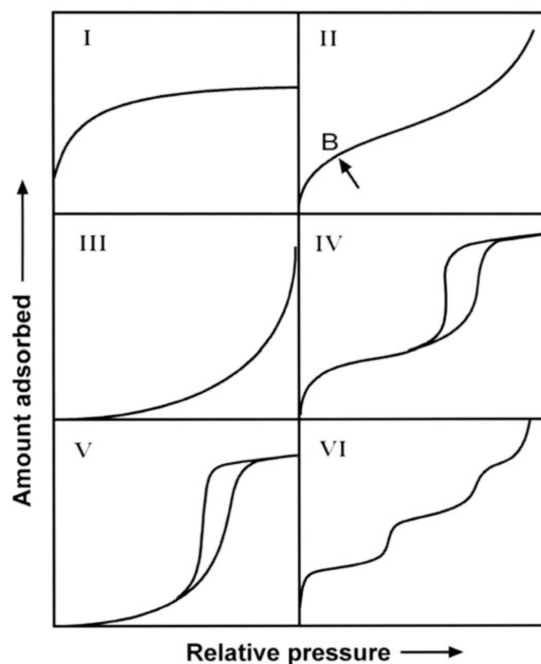
Figure 1.3 Six isotherm types by IUPAC nomenclature. Briefly, type I corresponds to a typical isotherm on a microporous surface. II is a typical nonporous or macroporous isotherm. III occurs when the adsorbate-adsorbent interaction is weak in comparison to adsorbate-adsorbate (no pronounced layer formation). Type IV is a typical mesoporous isotherm with hysteresis. V is similar to IV, but the adsorption initial part is from type III. VI corresponds to stepwise adsorption on a highly uniform nonporous surface. *Source: [2, 13].*

1.4 Open Questions

Our common goal is to find the answer to the series of questions related to theoretical methods for pore-size distribution estimation in nanoporous materials. The first open problem is related to the fact that currently there is a myriad of emerging materials that require tailored methods and tools for their precise characterization. Unfortunately, in order to characterize them precisely, there is no generic method that is applicable in every case. Therefore, one needs to build a series of theoretical isotherms for the emerging materials (corresponding, for example, to a different pore size), which we call custom or *tailored kernels.* A specific example is silica colloidal crystals, commonly known as opals, covered in Chapter 2. Characterization of these materials can be
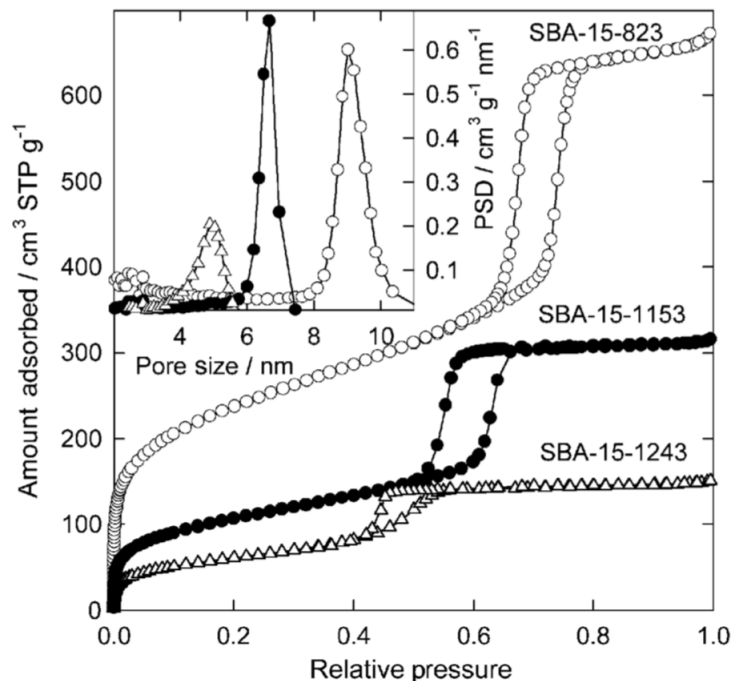
Figure 1.4 Dependence of adsorption isotherms on the pore size for very similar materials. One can see here that the pore size affects not only in the total amount adsorbed, but it also results in the shift of points of capillary condensation and evaporation.

Source: [18].
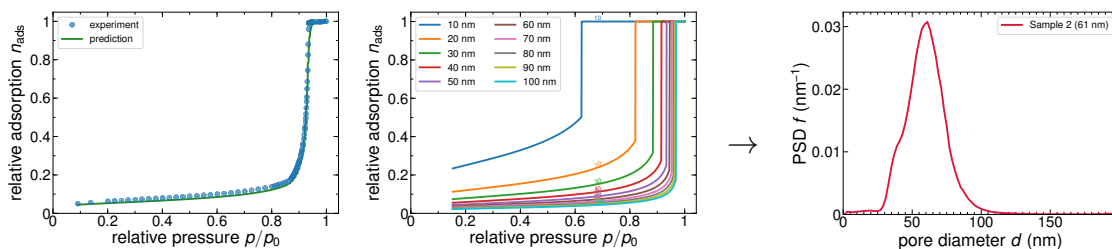
Figure 1.5 Schematic of predicting a pore-size distribution (right) for a given experimental isotherm (left) and theoretical kernel (middle). The idea of calculation of a kernel using Derjaguin-Broekhoff-de Boer (DBdB) Theory and numerical solution of adsorption integral equation is provided in Chapter 2.

challenging because they have pores of roughly tens of nanometers, and the surface is

subject to be modified in certain experiments. The large pore size makes it impossible

to build kernels based on molecular simulations due to a large number of atoms

required to simulate adsorption in the pore. The surface modification aspect leaves us the problems for methods like Density Functional Theory (DFT) [2, 20, 21, 3], which require complex parametrization for every surface. To tackle these issues, we used a macroscopic Derjaguin-Broekhoff-de Boer (DBdB) Theory [19] lacking these drawbacks.

Other materials, for example, three-dimensional ordered mesoporous (3DOm) carbons [16, 5], have complex geometry with features like interconnected windows. However, if one would try to characterize this kind of materials using a conventional independent spherical model, the estimates even for the main peak of the pore-size distribution will not match the expectation. Therefore, the influence of interconnections must be reflected in the model. Thus, the next open problem is to generate kernels for materials in which the interconnection between the pores are essential. However, this geometry is complicated for macroscopic approaches as well as DFT since it becomes a three-dimensional problem with no cylindrical or spherical symmetry. Based on that, in Chapter 3, the Grand Canonical Monte Carlo (GCMC) method was utilized. The idea in this chapter is to extend the system to the one with periodic boundary conditions by allowing the molecules to pass through the interconnections to a neighbor simulation cell. Having the simulation run, the new kernels gave notably different results for pore-size distribution in comparison to the spherical model, which showed the importance of taking into account the presence of windows for characterization of 3DOm carbons and similar materials with spherical mesopores.

Although the analysis of gas adsorption isotherms is a powerful tool widely used for characterization, there are other criteria used for determining the pore-size distribution. These criteria can be experimental properties of fluid in pores, which are different in confinement and depend on the pore size. As a first example, an alternative method to the adsorption isotherms is thermoporometry, an approach based on the deviation of the freezing temperature of a liquid in a pore [22]. Therefore, there is

a need to identify other properties of fluids, which are related to the pore size and can readily be measured experimentally. As another example, Chapter 4 explores the compressibility of nitrogen in the pores. More specifically, we analyzed the ultrasonic measurements made by Warner and Beamish [1] by calculating elastic properties from the existing data and then used molecular simulations to provide a quantitative model for the experiment.

Chapter 5 addresses the question of the efficiency of Monte Carlo methods for molecular simulation of adsorption. Thus, GCMC simulations executed serially in one thread are limited to very small pores. One could see this in Chapter 4, where the simulation results were limited to a pore size of about 10 and we could not simulate certain trends for larger pores sizes. To support larger systems and improve sampling, in Chapter 5, we consider a promising kinetic Monte Carlo method for the simulation of Vapor-liquid Equilibrium (VLE) and adsorption with comparison to GCMC, as well the parallel version of it optimized for GPU.

1.5   Structure of the Dissertation

This Ph.D. thesis aims to address a broad scope of applied theoretical problems related to the use of gas adsorption for characterization of porous materials, motivated by recent development in materials synthesis (Chapters 2 and 3), experimental techniques for characterization of porous materials (Chapter 4), and molecular simulations methods (Chapter 5). Addressing the open questions formulated in Section 1.4, this work will employ existing theoretical methods for characterization of new materials, propose new theoretical approaches to process experimental data, as well as to extend and verify recent molecular-level theories and simulation techniques. More specifically, Chapter 2 demonstrates an example of a development of a theoretical framework for pore-size distribution calculation tailored for a specific type of porous materials, namely silica colloidal crystals. Chapter 3 addresses a problem in adsorption modeling and

the difference in pore-size distributions of interconnected pores beyond the standard ink-bottle pore model. Chapter 4 is devoted to a study of nitrogen adsorption and how we can get additional useful data for pore size estimation from ultrasound data measured complementary to the traditional adsorption measurement techniques. These three chapters are already published in peer-reviewed journals. Chapter 5, which is about the kinetic Monte Carlo algorithm, has not been published and contains benchmark results with the classical MC scheme (the Metropolis et al. algorithm), an outline for improvement with the parallel version of the algorithm and further delivery of the results.

PORE-SIZE DISTRIBUTION OF SILICA COLLOIDAL CRYSTALS FROM NITROGEN ADSORPTION ISOTHERMS [1]

Abstract

Silica colloidal crystals are face-centered cubic structures comprised of silica spheres with the diameters ranging between tens and hundreds of nanometers. The voids between the spheres form pores, which can be probed by nitrogen adsorption porosimetry. Here we [2] prepared two mesoporous samples and a macroporous reference sample, then measured nitrogen adsorption and desorption isotherms for further characterization. We proposed a straightforward procedure for calculation of pore-size distribution of silica colloidal crystals from nitrogen adsorption isotherms. The procedure is based on the adsorption integral equation solution with a kernel of theoretical isotherms, consistent with the procedure used for many other porous materials. The solution is carried out using the non-negative least squares (NNLS) method with Tikhonov regularization. The kernel of isotherms is build based on the macroscopic Derjaguin-Broekhoff-de Boer (DBdB) Theory of capillary condensation considering the voids as a network of spheres. The outcome provides a good agreement with the single mode estimator, which is consistent with the geometrical estimates for the voids sizes. Furthermore, we modified the surface of the samples with organics, and repeated the characterization procedure for the modified samples. The resulting pore-size distribution for the samples with the modified surface matched the original one quite closely. It demonstrates the method as a simple and efficient technique to estimate the pore-size distribution, and justifies the spherical shape approximation for the voids in the silica colloidal crystals.

---

[1]The chapter was published in Maximov MA, Galukhin AV, Gor GY. Pore-Size Distribution of Silica Colloidal Crystals from Nitrogen Adsorption Isotherms. *Langmuir.* 2019;35(47):14975–14982

[2]The experimental part was made by Andrey Galukhin

2.1 Introduction

Silica colloidal crystals, often referred to as opals, are face-centered closely packed cubic crystals comprised of silica spheres forming a network of octahedral and tetrahedral voids [14]. These voids (pores) have sizes that could vary in the range of tens to hundreds of nanometers [24]. Being ordered transparent materials with the lattice constants close to the visible light wavelength, opals are widely applied as photonic structures [25, 26]. However, being ordered nanoporous materials, they also find applications as membranes for separation processes [27] and sensors [4].

Synthesis of silica colloidal crystals for the applications employing their porous structure requires reliable methods for characterization of these materials with respect to the surface area and pore-size distribution (PSD). Microporous and mesoporous materials, i.e., materials with pores below 50 nm in size, are typically characterized with nitrogen adsorption [2]. Although the crystals were made using the existing isothermal heating evaporation-induced self-assembly (IHEISA) method [28], until recently, mesoporous opals samples have not been synthesized in the form of thin films with masses sufficient for nitrogen adsorption using standard gravimetric or volumetric measurements. To our knowledge, nitrogen adsorption has not been carried out on silica colloidal crystals except for our recent work [14].

Recent paper by Galukhin et al. [14] reported nitrogen adsorption isotherms for three different opal samples, having similar surface properties but different sizes of the silica spheres. The work assumed the spherical geometry of the pores, and applied the Derjaguin-Broekhoff-de Boer Theory [29, 30](DBdB), in its version for spherical pores [19]. Analysis of the characteristic points on the experimental adsorption isotherms provided the estimates for the average sizes of the pores between the spheres, which were consistent with the geometric estimates.

Here we further explore the potential of nitrogen adsorption for characterization of opals. In addition to the opal samples used in the aforementioned work, we prepared

the samples with the same sphere sizes but modified surface properties. We measured the nitrogen adsorption isotherms on these new samples and analyzed those isotherms along with the isotherms from [14] with respect to the pore-size distribution.

The IUPAC recommendation for the calculation of pore-size distribution from a nitrogen adsorption isotherm is a combination of Density Functional Theory (DFT) with integral adsorption equation [2]. Although the density functional theory works for different pore geometries [21], the libraries available with commercial software are rather limited, not to mention that the source code for these methods is not open. In particular, the DFT predictions for nitrogen adsorption on silica surface are based on one reference silica material. Therefore, the application of this model for deriving the pore-size distribution of silica materials with modified surfaces can lead to incorrect PSD. Furthermore, the kernels of DFT isotherms for spherical pore geometry are limited with ca. 40 nm [31], which is not sufficient to describe the characteristic pores of silica colloidal crystals samples, estimated to be ca. 60 nm [14].

Here we propose to use the DBdB theory [19], fast and flexible method that is easy to implement and configure. The advantages of the approach are: 1) requires only two parameters, has a simple and intuitive physical interpretation; 2) does not require long optimizations or simulations; 3) can easily be implemented using classical algorithms available in modern numerical libraries; 4) shown to be consistent with DFT for pores above 7-8 nm in diameter [32]. We combined the DBdB method for calculation the adsorption isotherms with the adsorption integral equation solution using the NNLS method with Tikhonov regularization [33], following the steps described in [34]. We derived the PSD for our opal samples and showed its consistency with the geometrical analysis. We also showed that the PSDs derived using our procedure for the original samples are consistent with the PSDs for the samples with the modified surface.

2.2 Methods

2.2.1 Experimental [3]

Materials and methods. Ammonium hydroxide solution (28-30% of NH_3, Sigma-Aldrich), tetraethylorthosilicate (TEOS, >99.9%, Aldrich), tetrabutylammonium hydroxide solution (40% in water, Sigma-Aldrich), hexamethyldisilazane (>99%, Aldrich) were purchased and used without additional purification. Absolute ethanol was obtained by consecutive distillations of 96% ethanol over CaO and CaH_2. Deionized water (18.2 MΩ) was obtained by the Arium mini instrument (Sartorius).

Scanning electron microscopy (SEM) measurements were carried out using field-emission high-resolution scanning electron microscope Merlin Carl Zeiss. The particle size in colloidal crystals was estimated by measuring 100 individual particles. The UP200Ht ultrasonic homogenizer was used for all sonications. The MF48 centrifuge (AWEL) was used for all centrifugations. The LOIP LF-7/11-G1 furnace was used for calcination and sintering. Nitrogen adsorption and desorption measurements at 77 K were carried out with the ASAP 2020 MP instrument (Micromeritics). Before measurements samples were degassed by heating at $200\,°C$ under vacuum ($8\ \mu$mHg) for 2 hours. Adsorption and desorption isotherms contained about 200 points for each colloidal crystal sample. Specific surface areas of the silica colloid crystal samples were determined by applying the Brunauer-Emmett-Teller (BET) equation in a range of relative pressure $\sim 0.05 - 0.30$. Contact angle measurements were performed with drop shape analyzer DSA100 (KRÜSS, Germany).

Preparation of silica spheres. Silica spheres with sizes of 93 ± 5 and 106 ± 5 nm were prepared by two-step controllable growth technique based on regrowth of silica seeds [35]. Detailed information on synthesis conditions is described in our previous study [14]. Silica spheres with size of 565 ± 25 nm were prepared by classical Stöber

---

[3]The experimental part was performed by Andrey Galukhin

synthesis [14, 36]. All silica particles were isolated by centrifugation and sintered at $600\,°C$ for 12 h.

Preparation and morphology examination of silica colloidal crystals. Silica colloidal crystals were prepared by the modified vertical deposition method based on the isothermal heating evaporation-induced self-assembly (IHEISA) method [28]. Obtained colloidal crystals were carefully removed from the glass slide and sintered at $800\,°C$ for 12 hours, the desired temperature was achieved at a heating rate of $300\,°C$ per hour.

The functionalization of silica colloidal crystals was achieved via consecutive treatment of silica surface with tetrabutylammonium hydroxide solution in water (pH = 9.5) at $60\,°C$ for 12 h, and a hexamethyldisilazane (HMDS) solution in hexane (1.0 M) at $60\,°C$ for 12 h.

2.2.2   Derjaguin-Broekhoff-de Boer Theory

The Derjaguin-Broekhoff-de Boer Theory is a macroscopic approach that describes adsorption and desorption by considering the adsorbed film layer on a pore wall of cylindrical [29, 30] or spherical [19] geometry. In this chapter, we consider our system as a spherical pore with radius R and film thickness h. The model gives the following prediction for an adsorption isotherm before the point of capillary condensation and for a desorption isotherm after the evaporation point as:

$$\mu = \mu_0 + R_{\mathrm{g}} T \ln(p/p_0) = -\left(\Pi + \frac{2\gamma}{R-h}\right) V_{\mathrm{l}} \qquad (2.1)$$

where Π is disjoining pressure, γ is the adsorbate vapor-liquid surface tension, T is the absolute temperature, R_{g} is the gas constant, V_{l} is the molar volume, μ is the chemical potential, μ_0 is the chemical potential of the saturated vapor, which can put equal zero for simplicity of derivation. The disjoining pressure as a function of film thickness h (and no dependence on the capillary radius) can be calculated by the

Frenkel-Halsey-Hill [37] equation

$$\Pi = \frac{R_{\mathrm{g}}T}{V_1} \frac{k}{(h/h_0)^m} \tag{2.2}$$

where k and m are dimensionless empirical parameters, $h_0 = 1$ Å is a constant.

The mesoporous isotherm construction procedure goes in two major steps. First of all, we find k and m parameters for disjoining pressure described by Equation (2.2) from a macroporous reference material isotherm, where Equation (2.1) can be approximated as $\mu \approx -\Pi V_1$ since the radius in macropores is way larger than in mesopores. Therefore, these parameters can be estimated from the linear regression. For some already studied materials like silica, k and m can be accessed from reference data [38, 39].

The next step is to find a point of capillary condensation or evaporation for further maximal thickness estimation where Equation (2.1) holds. For the adsorption branch, the condition on capillary condensation is $\left.\frac{d\mu}{dh}\right|_{h=h_{\mathrm{c}}} = 0$. The thickness h_{c} can be found by calculating the derivative numerically or analytically and solving the optimization problem. Once it is found, the values below thickness h_{c} are evaluated using Equation (2.1), the values for the rest of the interval are set to relative adsorption equal to 1. Similarly, for desorption, the corresponding condition of evaporation is the zero change of the Gibbs free energy on complete filling $\Delta G_{p,T} = 0$. The explicit expression to find film thickness h_{e} for spherical pores is given by Equation 17 from [19]:

$$\mu = \frac{-3V_1}{R - h_{\mathrm{e}}} \left[\gamma + \frac{\int_{h_{\mathrm{e}}}^{R}(R-h)^2\Pi(h)\mathrm{d}h}{(R-h_{\mathrm{e}})^2} \right] \tag{2.3}$$

The minimal adsorbed film thickness where the theory is applicable corresponds to $h \simeq \sigma_{\mathrm{ff}}$, the Lennard-Jones (LJ) fluid-fluid interaction diameter. Finally, one can build an isotherm in terms of given range of fluid density n_{ads} and estimated surface

area S_A by finding thickness h using

$$n_{\text{ads}} = \frac{hS_A}{V_l} \tag{2.4}$$

Pore-Size Distribution

For a given experimental adsorption or desorption isotherm, the mean pore size can be estimated using single mode prediction by picking a pore size using the DBdB theory. A way to implement this is to match the maximum of the slope of the experimental adsorption or desorption isotherm with the corresponding point of capillary condensation or evaporation predicted by the DBdB theory for a trial pore size [14].

In order to extract the pore-size distribution $f(d)$ as a function of the pore size d for a given experimental adsorption or desorption isotherm $n_{\text{exp}}(p/p_0)$, one can solve the adsorption integral equation:

$$n_{\text{exp}}(p/p_0) = \int_{d_{\text{min}}}^{d_{\text{max}}} n_{\text{kernel}}(p/p_0, d) f(d) \mathrm{d}d \tag{2.5}$$

where $n_{\text{kernel}}(p/p_0, d)$ is the series of isotherms in the kernel for given relative pressure p/p_0 and diameter, d_{min} and d_{max} are the corresponding limits of the kernel. Thus, the Derjaguin-Broekhoff-de Boer Theory can be used to generate a kernel $n_{\text{kernel}}(p/p_0, d)$ using the method described in the previous subsection for both adsorption and desorption branches by using Equation (2.1). In the discrete case, the equation can be represented in a matrix form, further solved using the non-negative least squares (NNLS) algorithm with the Tikhonov (ridge) regularization penalty by Generalized Cross Validation [34, 33].

Here we briefly summarize how to solve Equation (2.5) in the discrete case. Thus, the equation can be represented in a form of the regression equation $\boldsymbol{y} = X\boldsymbol{\beta} + \boldsymbol{\epsilon}$ for dependent variables $\boldsymbol{y}$ and residual $\boldsymbol{\epsilon}$ N-vectors, regression coefficient q-vector $\boldsymbol{\beta}$, independent variables $N \times q$-matrix X as $\hat{\boldsymbol{\beta}} = \text{argmin}_{\boldsymbol{\beta}} \|\boldsymbol{y} - X\boldsymbol{\beta}\|_2^2$ subject to

$\beta_i \geq 0$ and $\sum \beta_i^2 \leq t$ constraint, where hat represents the solution vectors given by the predictor, t is the regularization parameter choice of which will be discussed later. In our case, $\boldsymbol{y}$ is the experimental isotherm, X is the kernel, $\boldsymbol{\beta}$ is the pore-size distribution, N is the number of points on the isotherm, q is the number of trial pore sizes. Technically, it is convenient to transform the problem by augmenting solution vector $\hat{\boldsymbol{y}}$ by a zero vector and kernel X by a unit matrix multiplied by square root of new regularization parameter λ into

$$\widetilde{\boldsymbol{y}} = \begin{bmatrix} \hat{\boldsymbol{y}} \\ \boldsymbol{0_{q \times 1}} \end{bmatrix} = \begin{bmatrix} X \\ \sqrt{\lambda} I_{q \times q} \end{bmatrix} \cdot \hat{\boldsymbol{\beta}} = \widetilde{X} \hat{\boldsymbol{\beta}} \tag{2.6}$$

This way, the Tikhonov NNLS problem for X, $\boldsymbol{y}$, λ is reduced into the equivalent NNLS problem for $\widetilde{X}$, $\widetilde{\boldsymbol{y}}$ and can be solved using the Lawson-Hanson algorithm [40] or its modifications available in many numerical packages. There are many ways to choose regularization parameter λ, one of the ways is the leave-one-out cross-validation, which is the minimization of the error by eliminating one point at a time and using it for validation. To make the calculations more efficient, the method can be approximated by the generalized cross-validation criteria [41] as the minimization of

$$\text{GCV}(\lambda) = \frac{1}{N} \left[\frac{\sum_{i=1}^{N} (y_i - \hat{y}_i)}{1 - \text{tr} H / N} \right]^2 \tag{2.7}$$

where $H = X(X^T X + \lambda I_{q \times q})^{-1} X^T$ is the projection matrix so that $\hat{\boldsymbol{y}} = H\boldsymbol{y}$. Once regularization parameter λ at which $\text{GCV}(\lambda)$ is at minimum is found, one can get PSD as $\hat{\boldsymbol{\beta}}$, the solution isotherm as $\hat{\boldsymbol{y}}$ from Equation (2.6).

2.3   Results

Experimental

Among two existing approaches, namely sedimentation and vertical deposition [42, 43], used for the production of colloidal crystals, we chose the latter one in a form
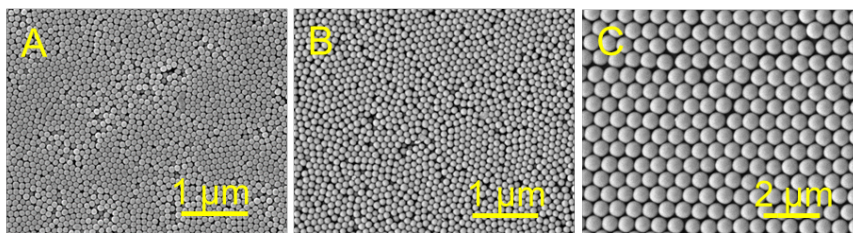
Figure 2.1 SEM images of (111) plane of silica colloidal crystals made of 93 ± 5 (A), 106 ± 5 (B), and 565 ± 25 (C) nm silica spheres.

of isothermal heating evaporation-induced self-assembly (IHEISA) [28] to prepare colloidal crystal samples. Compared to the classical vertical deposition method, IHEISA allows to obtain well-ordered colloidal crystals in a time-saving manner without any limitations imposed by the size of silica spheres. Figure A.4 shows the morphology of the synthesized colloidal crystals obtained by SEM. The absence of cracks as well as the presence of some microscopic defects can be detected on the (111) plane of the samples made of 93 ± 5 and 106 ± 5 nm silica spheres, whereas reference sample is virtually free of defects.

Surface modification of obtained colloidal crystals was used to change the strength of adsorbate-adsorbent interaction. Since optimal chemical modification of the silica surface requires its complete rehydroxylation [44], we used two-step modification protocol (Figure 2.2). It is expected that such protocol of modification does not affect the pore-size distribution of porous silica [45]. On the first step, the surface of sintered colloidal crystal was treated by an aqueous solution of tetrabutylammonium hydroxide which catalyzes the cleavage of siloxane bonds and the formation of silanol groups. The rehydroxylation results in surface concentration of silanol groups of ca. 4-5 groups per 1 nm of silica surface [14, 46]. The subsequent treatment of the rehydroxylized silica surface by HMDS results in transformation of silanols into trimethylsilyl groups. Due to the bulky nature of the $(CH_3)_3Si$ group only $\sim 40\%$ of silanols might be converted by HMDS [47]. Nevertheless, despite of incomplete conversion of silanol groups, the properties of silica surface are changed dramatically.
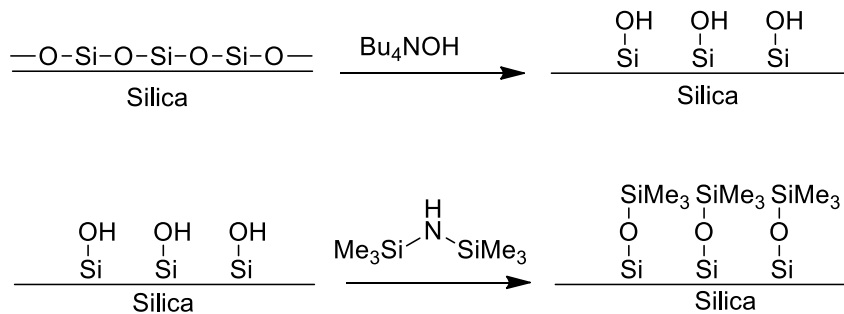
Figure 2.2 Surface modification of silica colloidal crystals.

As one can see from Figure 2.3, the water drop contact angle is changed from 24°
for the non-modified colloidal crystal (hydrophilic surface) to 133° after modification
(hydrophobic surface).
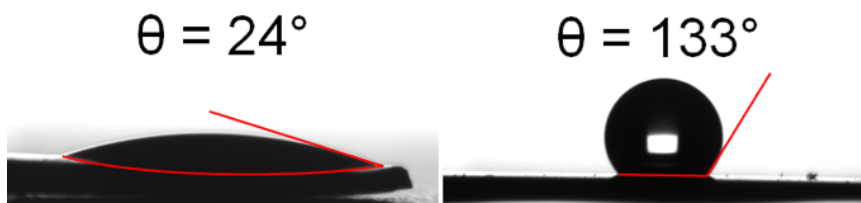
Figure 2.3 Water drop contact angle measurements of silica colloidal crystals before
and after modification (the water drop volume is 20 μL).

The resulting experimental adsorption and desorption isotherms before and after
modification are presented in Figure 2.4. The plots in absolute units are provided in
Appendix A. Here and later we will use the M suffix to the sample name to designate
that the surface was modified, e.g., original Sample R will be referred to as Sample
RM after its modification.

Analysis

The first step in the experimental data analysis was to calculate BET surface area
S_A and to find Frenkel-Halsey-Hill fitting parameters k and m for the disjoining
pressure from the reference macroporous adsorption isotherms, which are presented
in Table 2.1; the corresponding FHH fit is presented in Figure 2.5. The reference
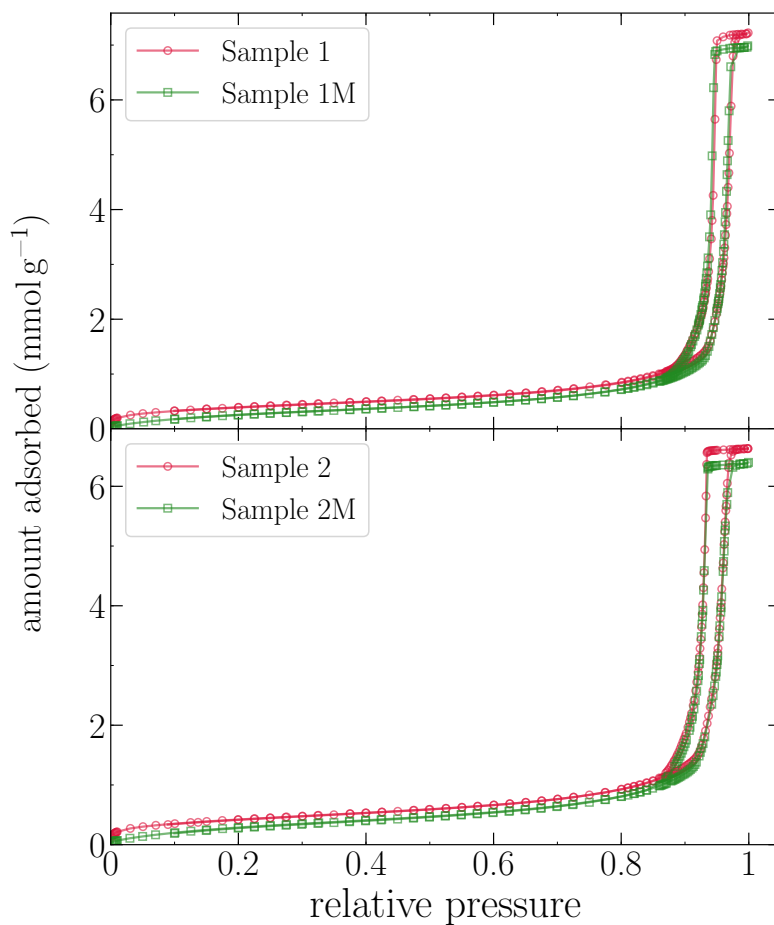
Figure 2.4 Experimental nitrogen adsorption isotherms at $T = 77$ K for Samples 1 and 2 before (circles) and after (squares) modification.

values required for calculation were retrieved from the CoolProp [48] thermophysical properties database for nitrogen at $T = 77$ K and $P = 1$ atm. Molar volume of the liquid phase V_l was 34.7 mL mol^{-1} [49], surface tension γ was 8.96 mN m^{-1} [50]. The surface area necessary for the film thickness calculation was estimated using the BET (Brunauer-Emmett-Teller) Theory [51]. For this approach, the effective cross-sectional area for nitrogen at 77 K was chosen as 0.162 nm^2 [2], the relative pressure range was from 0.05 to 0.31, similarly to the range in [14] and close to the recommended range

of $\sim 0.05 - 0.30$ by IUPAC [2]. The BET plots and FHH fit for all samples available in Appendix A.

Table 2.1 Parameters of the Samples

Sample	d_{sph}, nm	k	m	S_A,$\text{m}^2\,\text{g}^{-1}$	C	$\Delta H_{\text{ads}}, \frac{\text{J}}{\text{K\,mol}}$	d, nm
Sample R	565 ± 25	47.17	2.53	5.9 ± 0.1	192.9	8.96	-
Sample 1	106 ± 5	-	-	31.2 ± 0.2	104.8	8.57	77
Sample 2	93 ± 5	-	-	33.8 ± 0.2	102.6	8.56	61
Sample RM	565 ± 25	38.1	2.3	4.7 ± 0.1	17.8	7.44	-
Sample 1M	106 ± 5	-	-	24.8 ± 0.2	15.9	7.36	75
Sample 2M	93 ± 5	-	-	27.7 ± 0.3	16.0	7.37	61

Note: Diameters of the silica spheres d_{sph}, FHH fitting parameters k and m, BET surface area S_A and C constants, predicted pore sizes d from the adsorption isotherms for reference and mesoporous samples and its corresponding modifications.

Nitrogen adsorption data also evidence dramatic changes in surface properties: the values of the C constants of modified samples drop by 7-10 times compared to non-modified samples (Table 2.1). The C constant in BET equation characterizes the strength of adsorbate-adsorbent interaction (Equation (2.8)) [51]. The value goes up with the increase of the difference between the enthalpy of the adsorbate desorption (ΔH_{des}) from a monolayer and the enthalpy of vaporization (ΔH_{vap}) of the liquid adsorbate.

$$C = \exp\left[(\Delta H_{\text{ads}} - \Delta H_{\text{vap}})/RT\right] \tag{2.8}$$

Based on the known value of ΔH_{vap} for liquid nitrogen ($5.6\,\text{kJ\,mol}^{-1}$ at 77 K [49]) one can calculate values ΔH_{ads} for non-modified and modified colloidal crystals, which turn out to be $8.70(20)\,\text{kJ\,mol}^{-1}$ (non-modified samples) and $7.39(7)\,\text{kJ\,mol}^{-1}$

(modified samples) on average. The values of BET constants and ΔH_{ads} for all samples are given in Table 2.1.

The second step was to make a single mode prediction, at least one the simplest and easiest ways available for the DBdB method as it only requires to simply scan for the pore size until the matching isotherm is found. Further, we generated a kernel for both adsorption and desorption branches for a wide range of pore sizes from 1 to 200 nm in diameter with a 2 nm step. A part of the desorption isotherm kernel for Sample 1M is visualized in Figure 2.6. The left limit for the relative pressure was chosen as the point that corresponds to the monolayer film thickness, i.e., when it equals to the LJ fluid-fluid interaction diameter of 0.36154 nm [52].

Once the kernels were ready, the third step was to solve the integral Equation (2.5) applying the Tikhonov regularization. The outcome with pore-size distributions for both samples with original and modified surfaces is presented in Figure 2.7. The PSD curves peaks provide a good agreement with the pore size estimate for both the original surface in [14] and the modified surface. The corresponding isotherms to these distributions, i.e., solutions of the equation, with experimental data are presented in Figure 2.8. The comparison of the solutions using the integral equation and single mode predictions is presented in Figure A.3 in Appendix A.

2.4   Discussion

From the isotherm analysis, in Figure 2.4 one can see that for the modified surface, the isotherms have less amount adsorbed before the capillary condensation and after capillary evaporation. It signifies weaker adsorption to the modified surface in comparison to the original one. The point of capillary condensation and evaporation is almost the same for the isotherm corresponding to Sample 1 but not for Sample 2. For Sample 2, after the modification we see a slight shift of the points to the right.
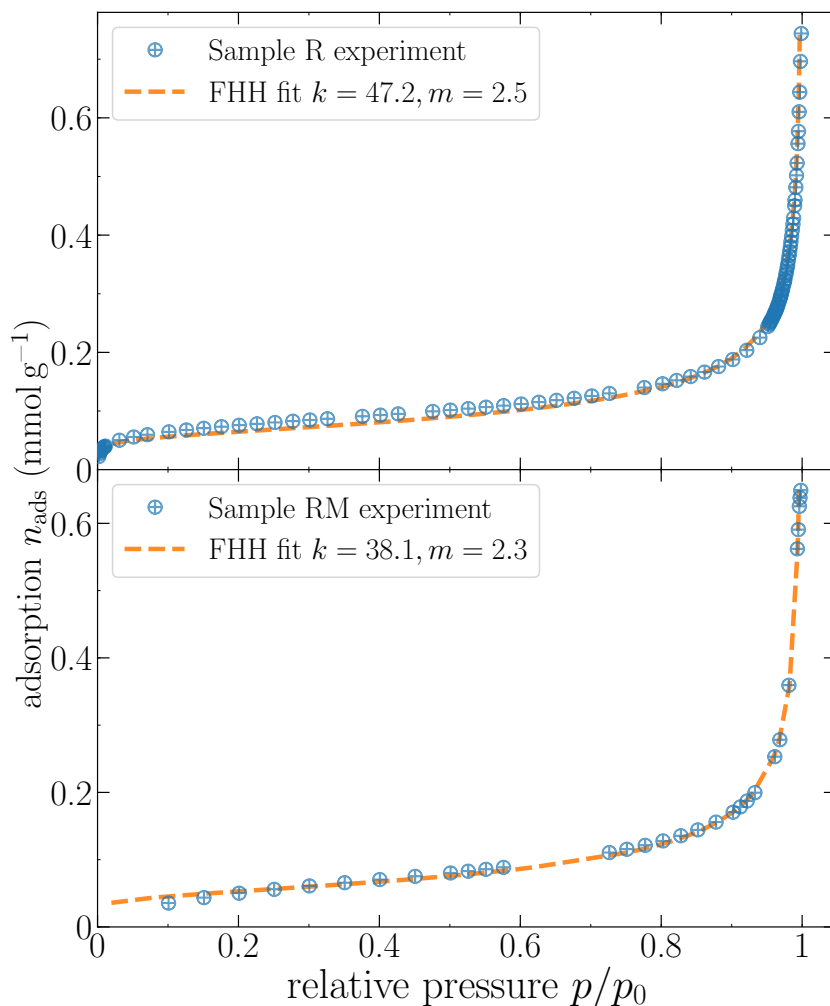
Figure 2.5 Reference macroporous isotherms with the corresponding Frenkel-Halsey-Hill fits.

The pore-size distributions presented in Figure 2.7 show good agreement of the peaks before and after the modification, which is expected since the surface modification should not appreciably affect the sizes of the mesopores. Also, it is worth noting a good agreement with the single mode solution. However, the different width of PSD extracted using adsorption and desorption kernels is an additional aspect to discuss. At least it is simple to explain the behavior mathematically: we have different isotherm slopes, and therefore, since the slope for desorption is steeper, to satisfy the equation, the solution would accumulate other pore size weights from the kernel with
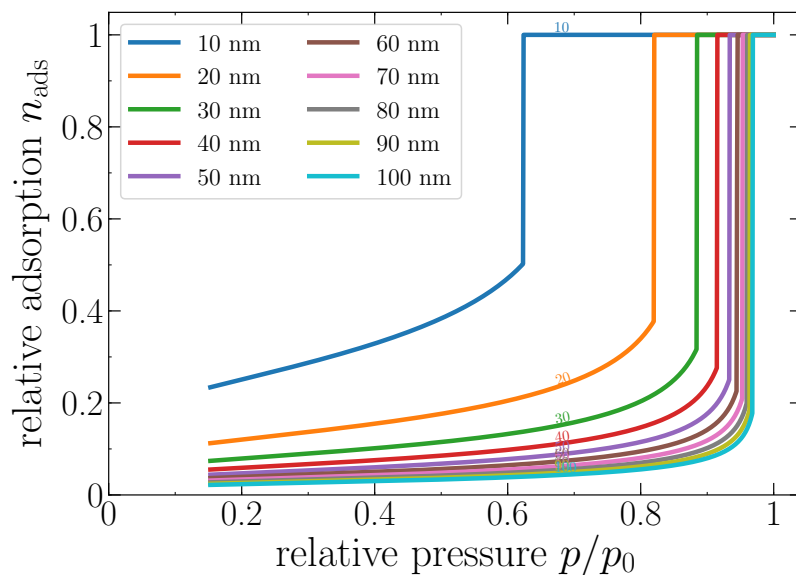
Figure 2.6 A fragment of the desorption isotherms kernel for modified surface plotted from $p/p_0 = 0.167$ corresponding to the adsorbed monolayer, where this macroscopic theory is applicable.

vertical points at the points of capillary condensation and evaporation. Often, the steep desorption branch of the isotherm is related to cavitation or pore blocking [53]. Deeper insight into the physics of desorption branch can be provided from scanning isotherms [54].

The obtained PSDs justify the single mode results from our previous work [14]. The analysis of the PSD shows that no additional mesoporosity is there (in Figure 2.7 at small values of the pore size). The kernel based on macroscopic DBdB theory does not allow one to assess microporosity, however a recent study by Farrando et al. demonstrated that nitrogen adsorption does not probe microporosity of the Stöber spheres anyway [15]. Therefore, it is likely that our macroscopic model does not lose much information. If further characterization of silica colloidal crystals with respect to micropores is needed, it should be performed using carbon dioxide adsorption at room temperature [15].
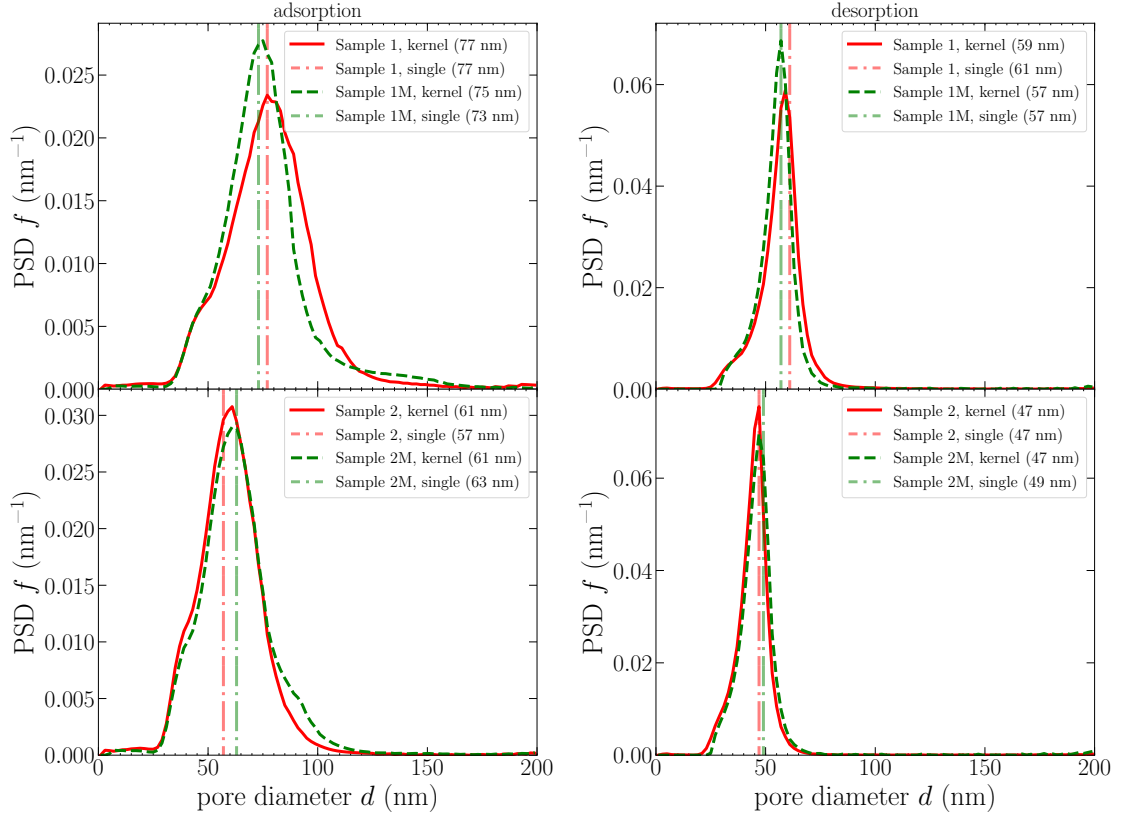
Figure 2.7 Pore-size distribution f predicted by the adsorption and desorption branches before and after surface modification for Samples 1 and 2 along with comparison to the single mode pore size estimation.

Our procedure for characterization of silica colloidal crystals form nitrogen adsorption can be easily applied by experimentalists directly for unmodified opals surface, or for various surface modifications. In this case it only requires fitting of the three parameters (k, m, S_{A}) from the reference adsorption data. The Python script for using the method, is provided. It can be applied for other porous materials, with the spherical pores.
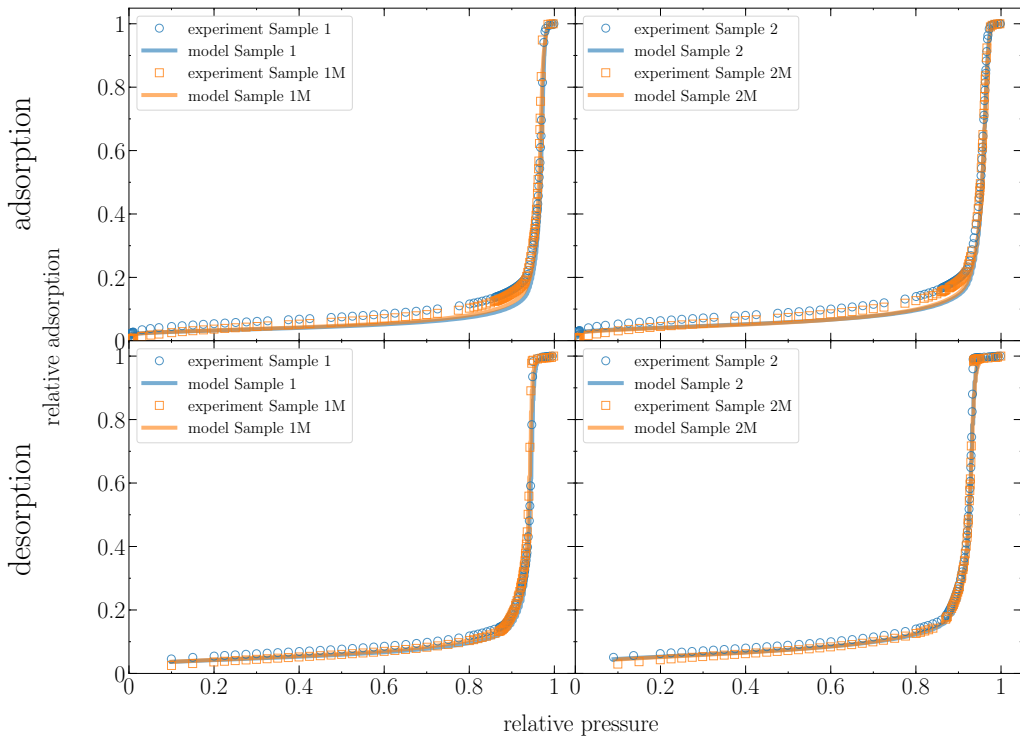
Figure 2.8 Solution of the adsorption integral equation (Equation (2.5)) versus experimental data.

2.5 Conclusion

In this chapter, we revisited applicability of the Derjaguin-Broekhoff-de Boer Theory for characterization of silica colloidal crystals using nitrogen adsorption. Specifically, we demonstrated that the approach gives pore-size distributions with a good agreement for the surfaces before and after modification. Analysis of the PSD from adsorption and desorption gives different peaks, which correspond to the characteristic sizes of voids in hexagonal *fcc* packing.

The method for pore-size distribution estimation is very efficient and straightforward for this pore size range, material, and procedure of surface modification in comparison with the density functional theory. Thus, the method only requires a

simple fitting procedure of three parameters and numerical solution of an integral equation. As a result, it gives the result almost instantly and does not require laborious DFT calculations. Also, we showed the consistency of the integral equation solution with the single mode estimator from the recent article [14].

CHAPTER 3

THE EFFECT OF INTERCONNECTIONS ON GAS ADSORPTION IN MATERIALS WITH SPHERICAL MESOPORES: A MONTE CARLO SIMULATION STUDY [4]

Abstract

Gas adsorption is a standard method for measuring pore-size distributions of nanoporous materials. This method is often based on assuming the pores as separate entities of a certain simple shape: slit-like, cylindrical, or spherical. Here, we study the effect of interconnections on gas adsorption in materials with spherical pores, such as three-dimensionally ordered mesoporous (3DOm) carbons. We consider interconnected systems with two, four, and six windows of various sizes. We propose a simple method based on the integration of solid-fluid interactions to take into account these windows. We used Monte Carlo simulations to model argon adsorption at the normal boiling point and obtained adsorption isotherms for the range of systems. For a system with two windows, we obtained a remarkably smooth transition from the spherical to cylindrical isotherm. Depending on the size and number of windows, our system resembles both spherical and cylindrical pores. These windows can drastically shift the point of capillary condensation and result in pore-size distributions that are very different from the ones based on a spherical pore model. Our results can be further used for modeling fluids in a system of interconnected pores using Monte Carlo and density functional theory methods.

3.1 Introduction

Nanoporous materials, materials with pore sizes below 100 nm, have a myriad of technological applications. The pore-size distribution (PSD) and specific surface area are the key parameters for characterization of nanoporous materials. These parameters are typically calculated from gas adsorption isotherms [2]. To derive a PSD from an experimental adsorption isotherm, one needs to make many assumptions about the pores, such as the surface properties (typically carbon or silica) and pore geometry (typically slits, cylinders, or spheres). Then, a kernel of theoretical adsorption isotherms for a given solid and pore geometry is used to solve the adsorption integral equation to get the PSD [33, 56, 21]. In recent years, many of the adsorption isotherm kernels were calculated using Monte Carlo (MC) simulations [57, 58, 59], density functional theory (DFT) [60, 61, 62], and macroscopic models [63, 64, 23], some of which are supplemented with commercial software for porosimeters and some are freely available.

Templated mesoporous silica with well-defined cylindrical pores [65] provided an excellent opportunity for verification and fine-tuning of theoretical models for the isotherms [66]. Furthermore, when new families of templated materials emerged, such models were extended to those new materials. A peculiar example of the templated nanoporous materials are a family of mesoporous carbons synthesized using spherical silica nanoparticles, often referred to as 3DOm (three-dimensionally ordered mesoporous) carbons [16]. 3DOm carbons received much attention for applications in electrical double-layer capacitors (EDLCs) [67], gas hydrate synthesis [5], and three-dimensionally ordered mesoporous-imprinted (3DOm-i) zeolites [68]. The SEM micrographs and adsorption isotherms for those materials suggest a very narrow pore-size distribution and a near-perfect spherical pore shape [69, 70]. A set of DFT kernels were developed specifically for the characterization of these types of materials; the calculations of the pore-size distribution based on these kernels confirmed the curves; however, the peaks of those PSDs did not match the expectations from the

29

sizes of silica particles used for templating. For instance, the average pore diameters for materials templated from the 10 nm silica particles appeared as 14 nm based on both argon and nitrogen adsorption isotherms [69]. This mismatch suggests that some of the assumptions made for modeling adsorption in 3DOm carbons are not justified. In many different porous materials, the interconnections between the pores alter the gas adsorption process. Therefore, the pore-size distribution obtained from the adsorption data can be affected by these interconnections [71, 72, 54]. However, modern models for PSD calculations, based on DFT or MC kernels, typically neglect these effects [21, 73, 2]. The synthesis procedure of 3DOm carbons as well as the SEM micrographs of their samples suggest that the pores are interconnected by several windows. An attempt to take into account the interconnections between spherical pores in molecular modeling of gas adsorption was limited to one window connecting two adjacent pores [74]. The observed difference in isotherms was rather small and insufficient to explain the significant mismatch in the pore-size distribution [69]. Recently, another work approached this question. Desouza and Monson [75] utilized lattice gas model DFT to study gas adsorption in 3DOm carbons. They predicted isotherms which qualitatively matched the experimental data; however, unlike the off-lattice DFT or MC, this method cannot provide a fully quantitative model and, thus, cannot be employed for characterization purposes. In this chapter, we investigate the role of interconnections between adjacent pores in templated materials with spherical pore geometry: we simulate the systems with two, four, and six windows connecting the pores. We developed integrated potentials to simulate gas adsorption in such systems and illustrated with an example of argon adsorption in model carbon mesopores. Our results demonstrate that the effect of four or six windows on the adsorption isotherms is significant, even when the window sizes are relatively small. They also suggest that neglecting interconnections can lead to a mismatch in the pore-size distribution observed in earlier works. In addition, we demonstrate that interconnections affect

other thermodynamic properties of adsorbing fluids, e.g., isothermal compressibility, which can serve as a fingerprint for pore size estimation [76, 77, 78]. The integrated potentials and the simulation framework developed in our work can be used for Monte Carlo and off-lattice DFT modeling of adsorption of gases in materials with spherical pore geometry as well as in materials with corrugated cylindrical pores [79, 80].

3.2   Methods

3.2.1   Integrated Solid-fluid Potentials

When modeling adsorption of simple gases on solid surfaces, such as N_2, Ar or CH_4 on silica or carbon, both fluid-fluid and solid-fluid interactions can be represented by the simple Lennard-Jones potential. Furthermore, their interactions with the solid surfaces are non-site-specific and can be presented as integrated potentials. This approach allows the pre-calculation of the solid-fluid interaction rather than directly calculating the solid-fluid pair interaction with each move, thereby reducing the number of operations. The solid atoms are typically replaced by surface or volumetric density, and, then, the solid-fluid interactions are integrated over the surface or volume. This approach allows one to save computational time in Monte Carlo or molecular dynamics simulations and is especially useful for off-lattice density functional theory modeling, where the solid is presented as an external potential [21],

$$U_{\text{sf}}(\mathbf{r}) = n_{\text{s}} \iint\limits_{\partial\Gamma} u(s)\text{d}\mathbf{A}, \tag{3.1}$$

where

$$u(s) = 4\epsilon\left[\left(\frac{\sigma}{s}\right)^{12} - \left(\frac{\sigma}{s}\right)^6\right], \tag{3.2}$$

Here, $\mathbf{r}$ is the radius vector where the potential is calculated, s is the distance to surface $\partial\Gamma$ (represents the surface of the pore), $\text{d}\mathbf{A}$ is the area element, $\sigma = \sigma_{\text{sf}}$ is the

Lennard-Jones diameter, $\epsilon = \epsilon_{\mathrm{sf}}$ is the Lennard-Jones energy scale for the solid-fluid interaction, and n_{s} is the surface number density of the solid Lennard-Jones sites.

The first potential of this kind is the potential by Crowell and Steele [81]. This potential was later extended to create the famous 10-4-3 Steele potential for a carbon slit pore [82]. Later, integrated potentials were proposed for cylindrical [83] and spherical [84] pore models to model adsorption in siliceous materials with channel-like and cage-like pores. As for simulations of adsorption of simple gases in nanoporous carbons with different pore structures, the Steele potential has been recently generalized for different geometries, including spherical, and provided the corresponding analytical solutions [85].

While for certain materials, such as zeolites, templated silica, and templated carbons [69, 86, 67], the spherical pore geometry is more suitable, it has a substantial limitation: it represents the pore as an isolated entity not interacting with neighbors. An attempt to include an opening between the two adjacent spherical pores in the integrated potential and molecular simulation based on such potential did not show an appreciable difference in adsorption isotherms, except when the opening is very large. The integrated potentials proposed here take into account two, four, and six interconnections between the system of spherical pores. In the case of a spherical pore without windows, the analytical form of Equation (3.1) would be the Baksh-Yang potential [84],

$$U_{\mathrm{sf}}(r, R) = 2\pi n_{\mathrm{s}} \epsilon \sigma^2$$

$$\times \left\{ \frac{2}{5} \sum_{i=0}^{9} \left[\frac{\sigma^{10}}{R^i (R-r)^{10-i}} + \frac{\sigma^{10}}{R^i (R+r)^{10-i}} \right] \right.$$
$$\left. - \sum_{i=0}^{3} \left[\frac{\sigma^4}{R^i (R-r)^{4-i}} + \frac{\sigma^4}{R^i (R+r)^{4-i}} \right] \right\}, \tag{3.3}$$

where R is the pore radius corresponding to the external diameter d_{ext} (see Section 3.2.6) and r is the distance from the center of the pore. Potential given by Equation (3.3)
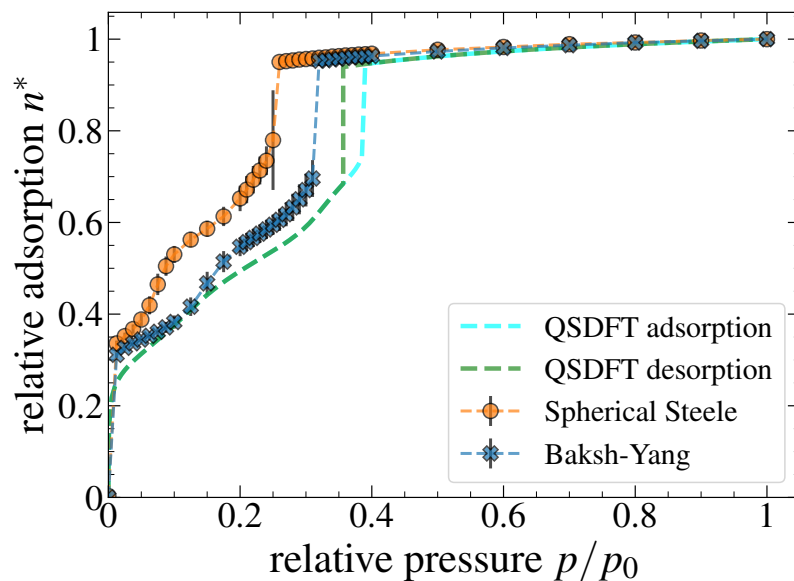
Figure 3.1 Comparison of the argon adsorption isotherms at 87.3 K for a 5 nm spherical carbon pore obtained using the "spherical Steele" [85] and Baksh-Yang potentials [84] in QSDFT data [70, 69], which is considered a standard characterization method, according to IUPAC.

is frequently used for modeling gas adsorption in silica pores via DFT and MC methods [66, 52, 76, 78].

Although we consider argon adsorption on the carbon surface, we chose to use the potential given by Equation (3.3), rather than the "spherical Steele" potentials, which includes integration over several layers of carbon atoms, proposed recently by Siderius and Gelb [85]. Figure 3.1 shows the comparison of the adsorption isotherms predicted by Monte Carlo simulation using the Baksh-Yang potential with the isotherms based on the spherical Steele potential. The latter appeared to be closer to the isotherms obtained by the quenched solid DFT (QSDFT) method [70], suggesting the choice for our simulations. This is different for materials like CMK-3 [58, 87], where the generalized Steele potential gives a closer match of isotherms.
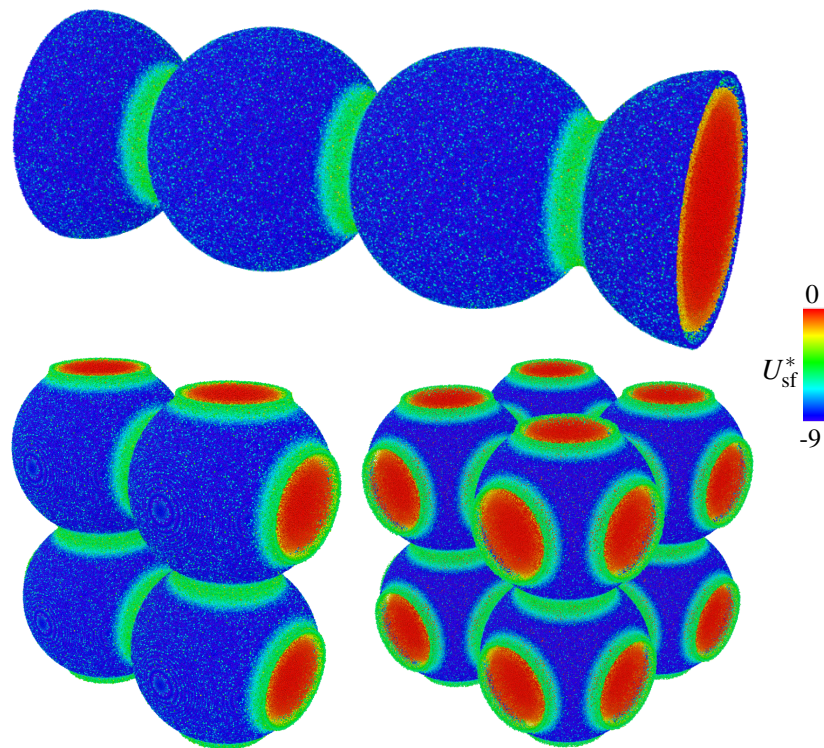
Figure 3.2 The structures of the systems of interest represented by potential maps for two, four, and six windows with an opening angle $\delta = \pi/5$.

3.2.2 Geometry with Two Windows

The simplest case of interconnected spherical pores is the chain of pores with two windows, arranged along one axis (see Figure. 3.2). At small window sizes, this model represents a pore system in materials such as 3DOm carbons [16, 5]; at larger window sizes, when it becomes comparable to the pore size, the system represents a corrugated cylindrical pore, a model frequently used for SBA-15 silica [79, 80, 88, 62, 89]. We describe the opening size in terms of polar angle δ (see Figure 3.3). For the two-window potential, the problem can be generalized in spherical coordinates as follows:

$$U_{\text{sf,2win}}(r,\theta) = \int_0^{2\pi} \int_\delta^{\pi-\delta} u\left(\theta', \varphi'\right) R^2 \sin\theta' \mathrm{d}\theta' \mathrm{d}\varphi', \tag{3.4}$$

where s can be explicitly expressed as $s^2 = R^2 + r^2 - 2Rr[\sin\theta\sin\theta'\cos(\varphi - \varphi') + \cos\theta\cos\theta']$, θ is the polar angle, and φ is the azimuthal angle. Primes, here and further, correspond to auxiliary variables. It is important to note that for the two-window case, we have cylindrical symmetry; hence, the function is not dependent on the azimuthal angle.

3.2.3 Periodic Boundary Conditions

An easy way to calculate the contribution from the neighboring images of the cell in spherical coordinates is to take into account the periodicity of the structure. This can be done by shifting the fluid atom by the cell z-axis length rather than integrating over the surface of the neighboring cells,

$$U_{\text{sf,PBC}}(r,\theta,\varphi) = \sum_{i=-N_{\text{cells}}}^{N_{\text{cells}}} U_{\text{sf}}\left(T_{z'=z+iL_z}(r,\theta,\varphi)\right), \tag{3.5}$$

where L_z is the length of the cell (see Figure 3.4), T is the translation of the (r, θ, φ) vector in spherical coordinates by L_z along the z-axis i times in cylindrical coordinates, N_{cells} is the number of cells in each direction, and U_{sf} is the target potential we want to extend. Using this method, we are able to take into account both fluid-fluid and
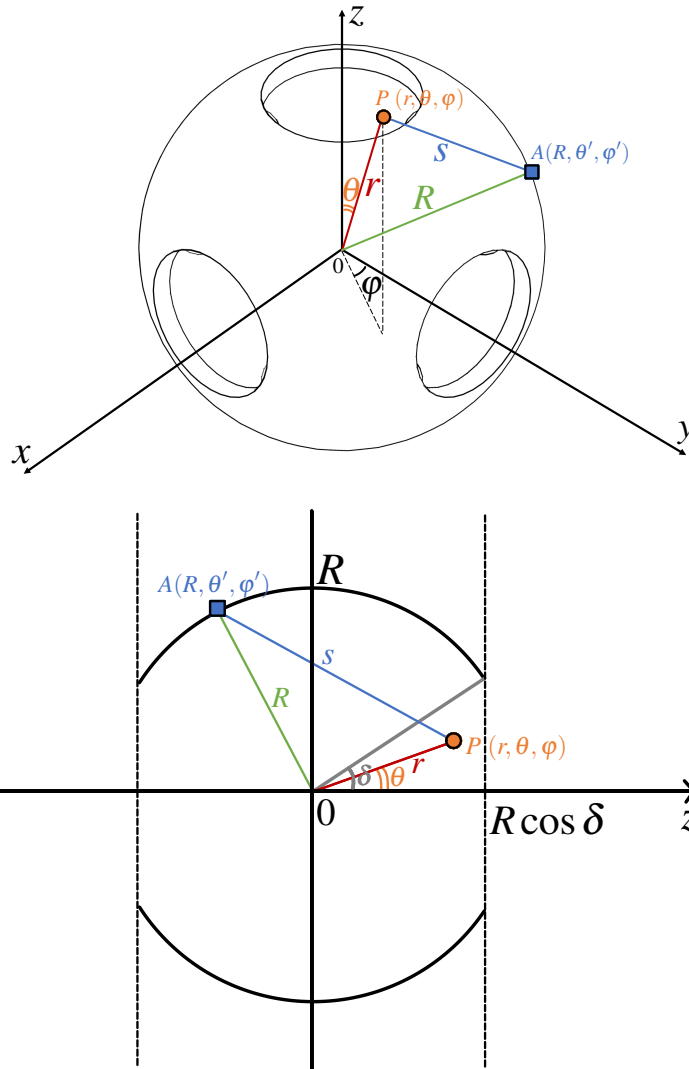
Figure 3.3 Geometric notation for the calculation of the potential at point $P\,(r, \theta, \phi)$ integrating over the surface with variables θ', ϕ'. Point $A\,(R, \theta', \phi')$ is a point on the surface, θ is the polar angle, φ is the azimuthal angle, R is the radius of the sphere, and δ is the opening polar angle.
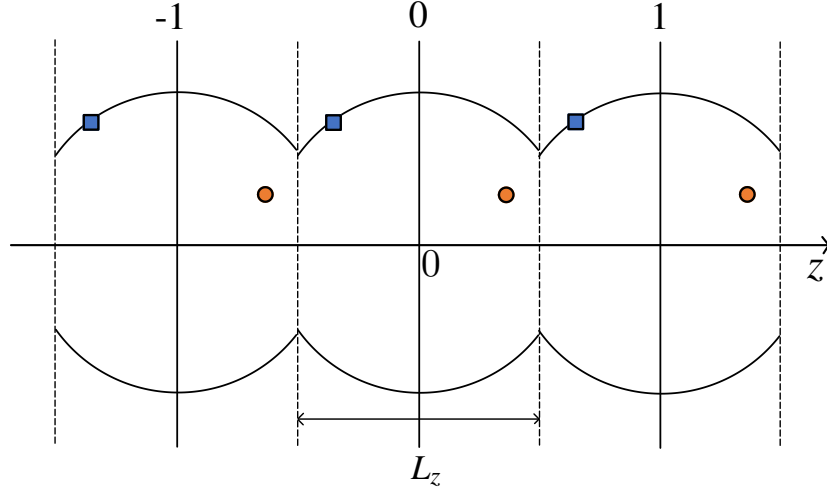
Figure 3.4 Periodic image contribution calculation. Digits above indicate the cell index, $L_z = 2R\cos\delta$ is the cell z-axis length. The orange circles are the virtual images of a fluid molecule where the potential should be calculated.

fluid-solid interactions of the neighboring cells. The effect of these interactions is elaborated in Section 3.3.2.

3.2.4   Integrated Potential with Four and Six Windows

As we increase the number of windows and try to calculate the integral over the surface directly, we lose the cylindrical symmetry. Instead of calculating the potential utilizing the cylindrical symmetry, we represent the target surface $\partial\Gamma$, which corresponds to the pore with windows, as a spherical surface complemented by caps (see Figure 3.5). Due to the additivity property of the integral, this gives a solution equivalent to Equation (3.4) in the case of two windows,

$$
\iint_{\partial\Gamma} u\mathrm{d}\mathbf{A} = \int_0^{2\pi}\int_0^{\pi} uR^2\sin\theta'\mathrm{d}\theta'\mathrm{d}\varphi' -
$$
$$
- \int_0^{2\pi}\int_0^{\delta} uR^2\sin\theta'\mathrm{d}\theta'\mathrm{d}\varphi' - \int_0^{2\pi}\int_{\pi-\delta}^{\pi} uR^2\sin\theta'\mathrm{d}\theta'\mathrm{d}\varphi',
\tag{3.6}
$$

Although the expression is analytically correct, the numerical calculation can be a bit
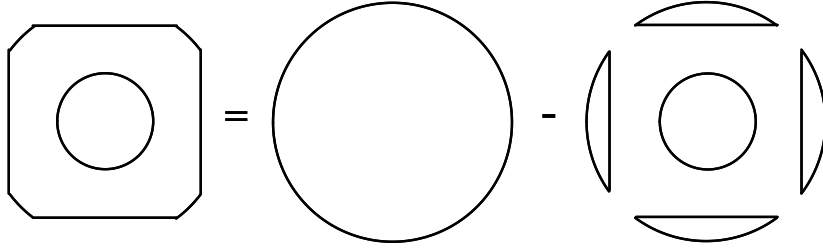
Figure 3.5 Extension of the model to calculate the potential with two to six windows in spherical coordinates. First, we calculate the integral over the sphere, and, then, we subtract the caps corresponding to each window in the pore.

challenging since the values of the constituent integrals can be large, and it requires calculating the integral with higher precision, which in turn downgrades performance. The solution here would be an adaptive scheme where one would calculate the integrals with higher precision if the first integral has a large value. In order to continue with the calculation of the integrals for other caps, which correspond to other pore windows, in spherical coordinates, one can transform the coordinate system by rotation and subtract these two integrals from Equation (3.6) for each window as it is depicted in Figure 3.5.

3.2.5   Mesh, Interpolation, and Coordinates

Due to cylindrical symmetry, we decided to use cylindrical coordinates for the two-window system. For this purpose, a mesh with 1000×1000 layers was generated for the corresponding axial coordinate z and radial distance ρ. To calculate the potential, we used bilinear interpolation by z and the closest band by a radial distance ρ.

For the system with four and six windows, we needed to use an alternative coordinate system. For this purpose, we created a mesh in the Cartesian coordinate system with 200-350 layers for each axis. We, then, used trilinear interpolation to calculate the potential. Discussion on the choice of the number of layers is presented in Appendix B.

3.2.6 Internal vs External Pore Diameter

The external diameter of a pore is defined as the maximal center-to-center distance between (solid) atoms within one cell [77]. On the other hand, the internal diameter is defined as the maximal accessible distance between fluid atoms, i.e., where the solid-fluid potential is equal to zero. For spherical and cylindrical pores, d_{int} is estimated as [52, 74]

$$d_{\text{int}} \approx d_{\text{ext}} - 1.7168\sigma_{\text{sf}} + \sigma_{\text{ff}}. \tag{3.7}$$

In the case of a pore with windows, neglecting the periodic boundary conditions, by geometrical estimates, the formula can remain the same until critical opening $\delta_{\text{c}} = \arccos(d_{\text{int}}/d_{\text{ext}})$, and the internal volume can be calculated as a volume of a sphere. Past this angle, the volume should be estimated using the volume with subtracted caps with the equivalent internal opening angle as

$$\delta_{\text{int}} = \arccos\left(\frac{d_{\text{ext}}}{d_{\text{int}}}\cos\delta\right). \tag{3.8}$$

The details about volume estimations are provided in Appendix B.

3.2.7 Monte Carlo Simulation and Parameters

Simulations were carried out using the Grand Canonical Monte Carlo (GCMC) approach by the Norman-Filinov algorithm [90] at fixed chemical potential μ, volume V, and temperature T with a pre-calculated potential for the solid-fluid interactions. All simulations were performed using the Chainbuild molecular simulation code [91] with custom modifications for pore geometry. The parameters for fluid-fluid and solid-fluid interactions are listed in Table 3.1 and represent the argon-carbon system. The simulations are performed at argon normal boiling point $87.3\,\text{K}$. The relative pressure $p/p_0 = \exp(\mu^* - \mu_0^*)/T^*$ was changed by varying chemical potential from a small value $\mu^* = -17.997$, corresponding to $p/p_0 = 10^{-5}$, to saturated chemical

potential $\mu_0^* = -9.5934$ calculated using the Johnson et al. equation of state [92]. The asterisks here and after correspond to the reduced Lennard-Jones units. The partition first was chosen uniformly at the $(0, 1]$ interval with 21 points, then, uniformly on $(0, 0.1]$ with 21 points, excluding 0 and replacing it with 10^{-5}. The pore size was chosen to be 5 nm with opening angles represented in Figure 3.6. The number of Monte Carlo moves was chosen to be at least 10^{10} for the isotherms, where the bulk modulus was calculated (see Figure 3.7), and at least 10^9 for the rest.

Table 3.1 Lennard-Jones (LJ) Parameters and Relevant Physical Properties for the Argon-Argon Fluid-Fluid (ff) and Carbon-Argon Solid-Fluid (sf) Interactions

Interaction	σ, nm	ϵ/k_B, K	n_s, nm^{-2}	r_{cut}, σ_{ff}	Ref
Ar - Ar	0.34	119.6	-	5	[93]
Carbon - Ar	0.3417	56.43	38.19		[94, 85]

Note: σ is the LJ diameter, ϵ is the LJ energy scale, n_s is the surface number density of solid LJ sites, r_{cut} is the distance at which the interactions were truncated; no tail corrections are used.

3.2.8 Isothermal Fluid Modulus

As it was shown in several recent works [95, 76, 77, 78, 96], elastic modulus of a fluid in a pore depends on the pore size. Therefore, an elastic modulus can serve as indication of the pore size, consequently, in addition to calculating the adsorption isotherms, we obtained the isothermal modulus of the fluid in the pores. A detailed discussion of these effects is given in Chapter 4. One way to calculate the isothermal fluid modulus K_f^T in pore confinement is from fluctuations of the number of particles using the following formula [97, 76]:

$$K_f^T = \frac{k_B T \langle N \rangle^2}{V \langle \delta N^2 \rangle},$$
(3.9)
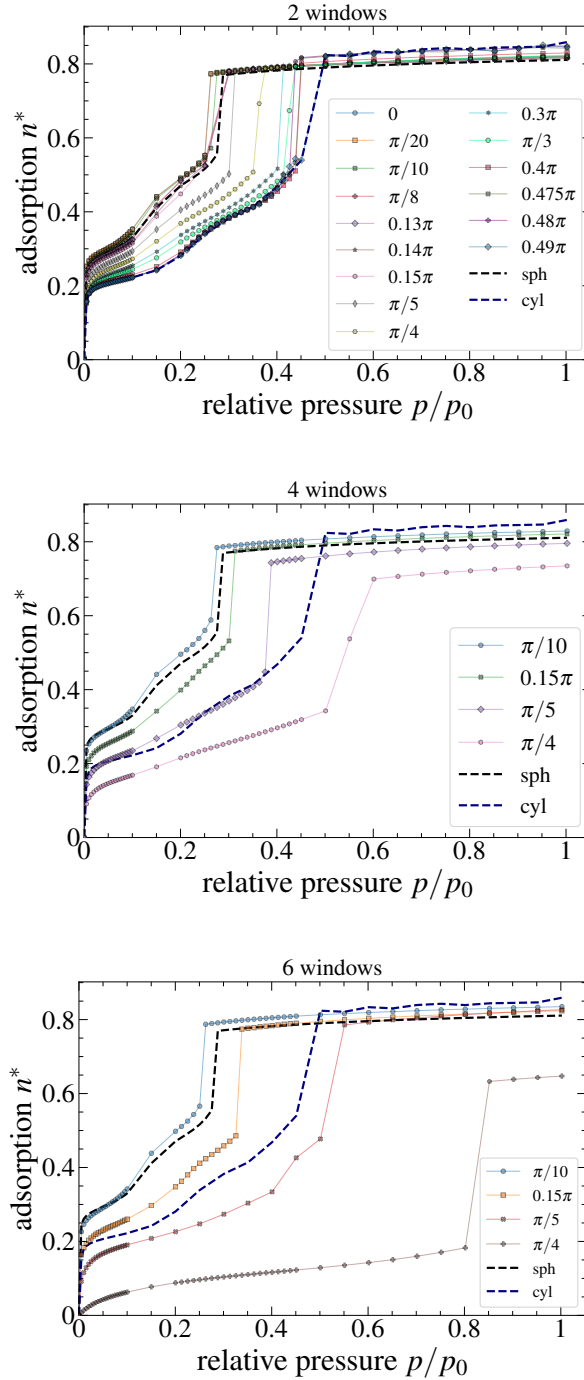
Figure 3.6 Argon adsorption isotherms at $T = 87.3\,\mathrm{K}$ for two (upmost), four (middle), and six (lowest) window carbon pores with different opening polar angles δ based on a sphere of 5 nm in diameter. Dashed isotherms represent both limiting cases for two windows, namely, spherical ($\delta = 0$; periodic boundary conditions were not applied) and cylindrical ($\delta = \pi/2$) pores.
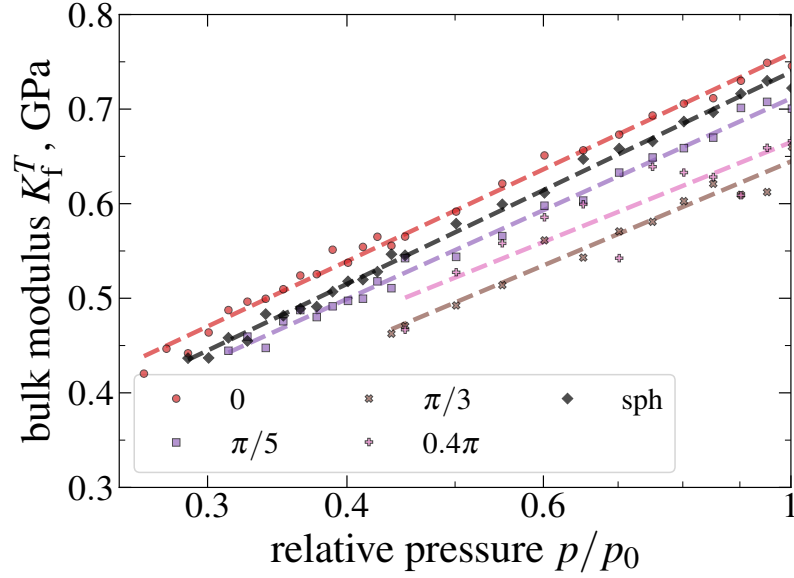
Figure 3.7 Isothermal fluid modulus K_f^T vs relative pressure in the log scale for various opening angles in a two-window system and a spherical ($\delta = 0$; periodic boundary conditions were not applied) pore calculated using Equation (3.9).

where N is the number of particles in the reservoir, k_B is the Boltzmann constant, V is the pore volume, and T is the temperature.

3.3 Results

3.3.1 Effect of the Opening Size for Interconnected Systems

The isotherms were simulated using the grand canonical Monte Carlo method at $T = 87.3\,\text{K}$ using the integrated potential for opening angles ranging from 0 to 0.49π and are presented in Figure 3.6. These results are presented along with the limiting cases of spherical and cylindrical pores.

The combined isotherms with an emphasis on the comparison of different numbers of windows are depicted in Figure 3.8. For a small opening angle, δ of 0.15π, the shift of capillary condensation in the case of four windows was 0.05 in terms of relative pressure, and an extra 0.1 for six windows.
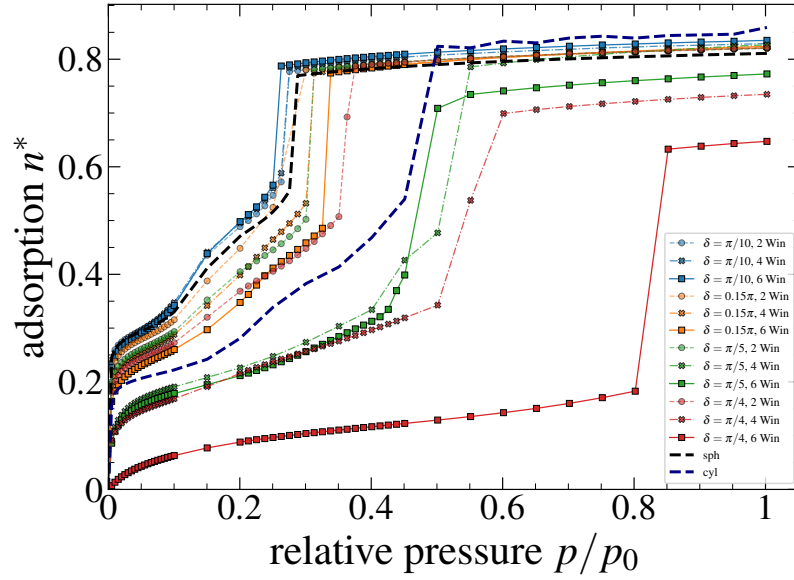
Figure 3.8 Isotherms with different numbers of windows and opening polar angles δ. The isotherms for large angles show a drastic difference as we increase the number of windows.

The comparison with the kernel of isotherms for pores with original sphere diameter $d_{\mathrm{ext}} = 5\,\mathrm{nm}$, a different number of windows, and opening angles are presented in Figure 3.9. Although the shapes of the isotherms with windows are different from the shape of the isotherms for purely spherical pores, the main mode of the PSD, which is often the main outcome of the adsorption characterization, is defined by the capillary condensation point. In this sense, the pores whose isotherms have the same capillary condensation points we consider equivalent. By comparing the point of capillary condensation, the two-window version with opening $\delta = \pi/5$ corresponds to an equivalent 5 nm spherical pore, and $\delta = \pi/4$ corresponds to a 6 nm pore. The larger pores have a combination of spherical and cylindrical behavior, but in terms of the point of capillary condensation, the pore with $\delta = 0.4\pi$ is close to an equivalent 6.5 nm spherical pore. For six windows, a closer representation of 3DOm carbons, a pore with $\delta = \pi/5$ has a shifted capillary condensation point leading to an equivalent spherical pore of 7.25 nm in diameter.
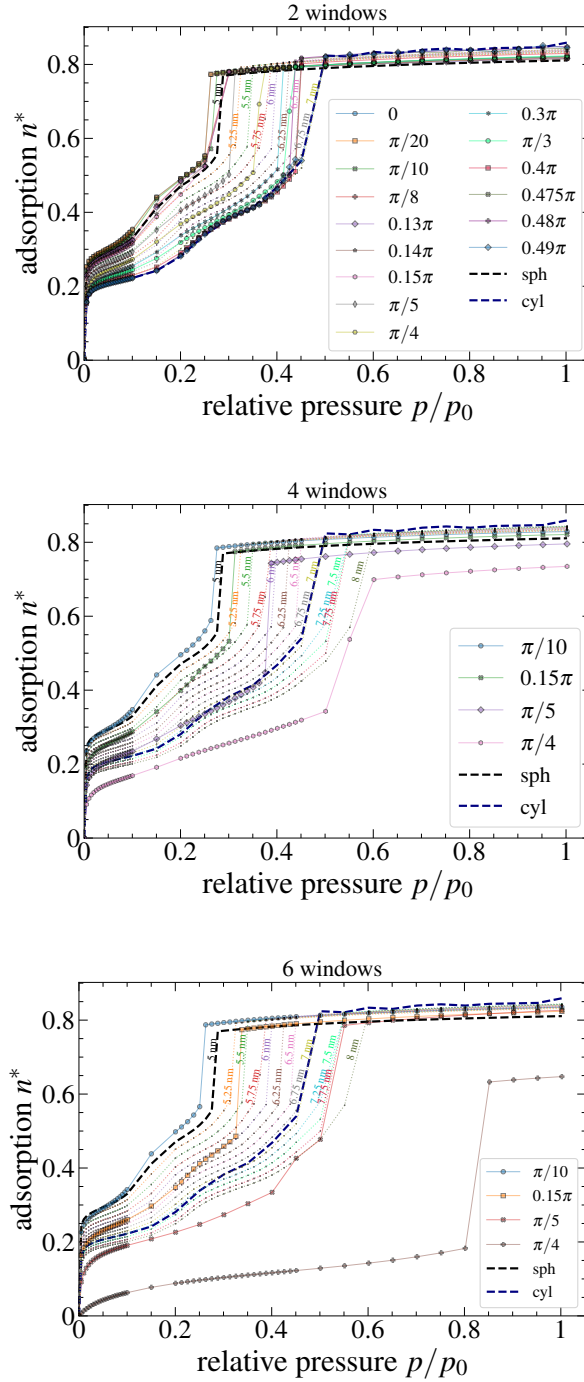
Figure 3.9 Isotherms with different numbers of windows and opening polar angles δ with comparison to the kernel of spherical isotherms from 5 to 7 nm (and to 8 nm for six windows) in diameter with 0.25 nm step.

3.3.2 Role of Periodic Boundary Conditions for the Isotherm

Typically, adsorption in a spherical pore is modeled as an isolated pore. However, for modeling of interconnections, we need to use the periodic boundary conditions, both for solid-fluid and fluid-fluid interactions (see Figure 3.10), and they clearly bring about some effect on the potential. Although technically these are two different problems, it is important to consider them when we try to compare the transition from spherical to cylindrical isotherms and use the results for verification. For this reason, first, we decided to check the potentials. Thus, the upper part of the plot of Figure 3.10 shows that at the very edge change in the potential is quite large, but it corresponds to a relatively small area. On the other hand, in the plot of Figure 3.10, we see that the effect is negligible in terms of a shift of capillary condensation and equal to about 0.025. This gives us an explanation for the slight shift of the isotherm for a pore with zero opening angle from the spherical isotherm.
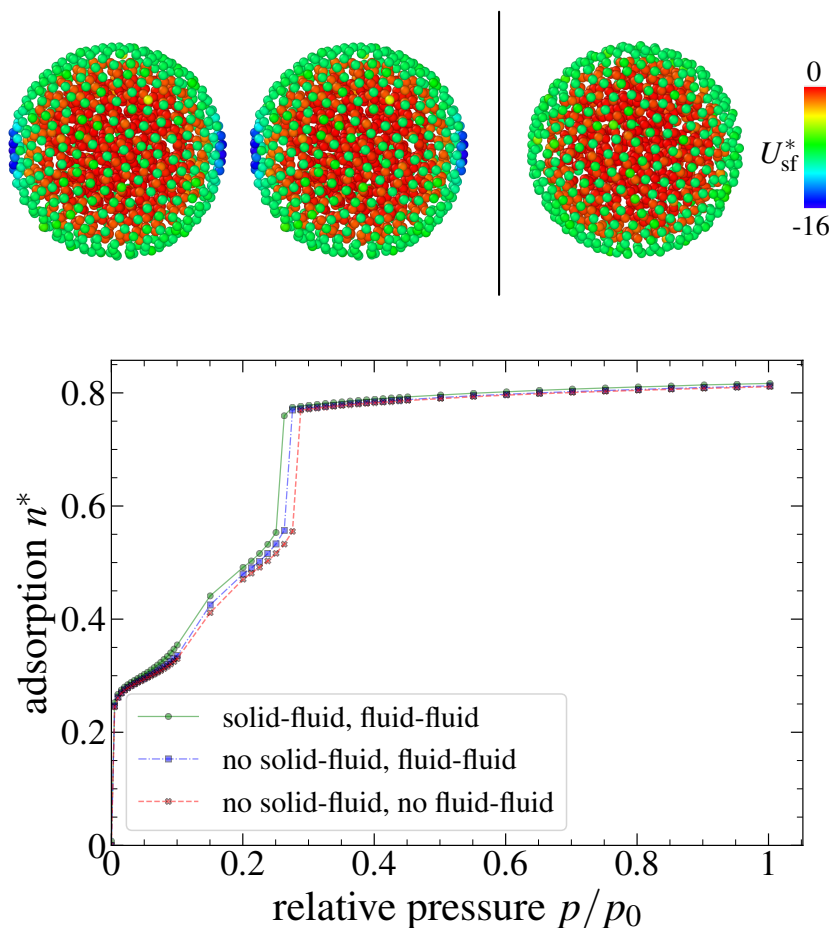
Figure 3.10 Effects of various types of periodic boundary conditions on isotherm at $\delta = 0$, in other words, a spherical pore. The upper-left image corresponds to the potential under solid-fluid and fluid-fluid conditions, the upper-right image shows the potential not under periodic boundary conditions, and the bottom plot shows the isotherms. In the simulations of interconnected pores, both solid-fluid and fluid-fluid conditions were utilized.

3.3.3 Isothermal Fluid Modulus

Earlier works suggested the isothermal bulk modulus of a confined fluid as another fingerprint of the pore size [76, 77, 78]. Since it does not require any additional simulations, and can be extracted from GCMC simulations data, we calculated this property for each of the systems. Figure 3.7 gives a plot of isothermal elastic modulus vs the relative pressure (in logarithmic scale) depending on the opening angle. The

points for each opening angle were fit using linear regression. The plot shows that larger window sizes give a lower modulus, thus, weaker confinement effects. The fluid in the pore system with the zero window size gives the modulus higher than the simple spherical pore. This is likely due to the PBC effects discussed in Section 3.3.2. Overall, this data is in line with what is seen on the isotherms. Note that when the window size increases, and the resulting system approaches cylindrical geometry, the points become more scattered. This effect is likely due to ordering effects, which are more pronounced in the cylindrical pores [77].

3.3.4 Local Density

The local density plot (Figure 3.11) was constructed as a histogram of the number of particles per volume $\Delta N/\Delta V$ over radial coordinate r by analyzing configurations. For each pair of particles, the radial coordinate was calculated and, then placed into bin i corresponding to the $[i\Delta r, (i+1)\Delta r)$ interval, where Δr is the discretization step. Then, the number of particles was divided by the volume of the shell corresponding to each bin using the formula for the cylinder. For consistency, we use one formula to calculate the ΔV for each case in Figure 3.11. The chosen pore opening angles are similar to a cylindrical pore, hence we chose the formula for the cylinder.
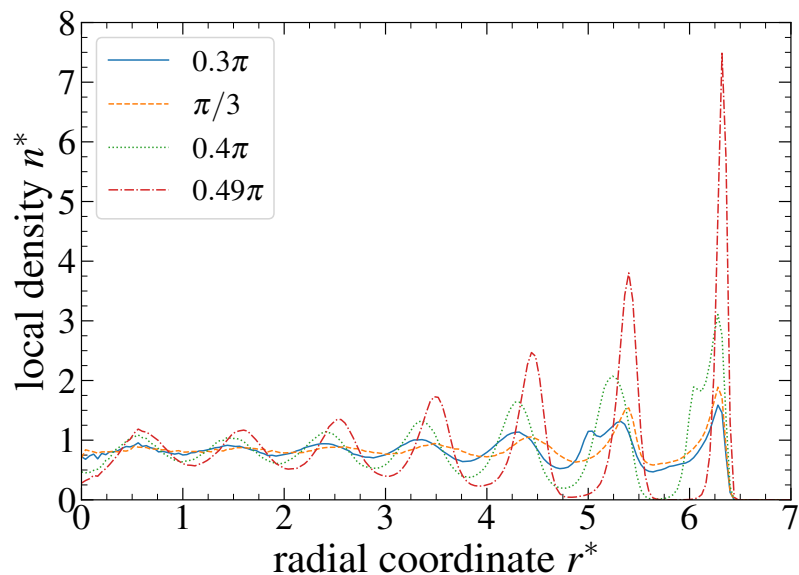
Figure 3.11 The local density function for various opening angles δ of a two-window system calculated using the formula for a cylinder. The estimated peaks represent adsorbed layers of fluid in the pore.

3.3.5 Pore-Size Distribution

Finally, we illustrate how the application of an isotherm kernel corresponding to the pore model with windows differs compared to the application of a simple spherical kernel. For this purpose, we generated two test isotherms: isotherm 1 – an isotherm for a 4.5 nm pore taken from the six-window kernel ("New Kernel") with $\delta = \pi/5$ openings, and isotherm 2 – constructed as a linear combination of the isotherms for 4.0, 4.5, and 5.0 nm from the same kernel with the weights of 0.25, 0.5, and 0.25, respectively. We calculated the PSDs for these isotherms by solving the adsorption integral equation using non-negative least squares (NNLS) regression with Tikhonov regularization [23, 34] on the two isotherm kernels: the one used for constructing these isotherms and a spherical kernel without openings ("Sph. Kernel"). Figure 3.12 shows the kernels, the test isotherms, and the results of the PSD calculations. While the first kernel gave the expected "true" PSDs for both isotherm 1 and isotherm 2, the

spherical kernel predicted much broader distributions, with the peaks shifted to 6 nm. This difference in the PSD predictions qualitatively (and almost quantitatively) agrees with the overprediction of the pore sizes in 3DOm carbons from the application of the simple spherical pore model [70, 69].

3.4   Discussion

Figure 3.2 shows that a system with two connecting windows is an intermediate case between the spherical and cylindrical pore models. Indeed, in the case of two windows, we found a gradual and smooth transition of isotherms between the limiting cases: the spherical and cylindrical cases. Geometrical estimates for the critical angle δ_c can be verified by the fact that for small windows with opening polar angle $\delta < \delta_c$, the isotherms are very close to the spherical pore isotherm. After this angle, the isotherms are shifted toward the cylinder. An interesting observation is an intermediate case at $\delta = \pi/4$, which represents a corrugated cylinder. As shown in the upper panel of Figure 3.6, the isotherm for this pore behaves like a cylinder before the point of capillary condensation in terms of the density value; and has almost the same capillary condensation point. In contrast, after the condensation point, its behavior is similar to a sphere, namely, the final density after the point of capillary condensation is closer to the value corresponding to a sphere, only slightly shifted toward the cylindrical isotherm. The molecular snapshot is rendered in Figure 3.13.

We further investigated the effects of confinement on the fluids quantifying their local density. The obtained histogram in Figure 3.11 gave us layers, the peaks do not match the radial coordinate as occurred in one of our previous studies [77]. Although we admit that the plot shows rather qualitative observation due to the ambiguous definition of volume slices ΔV, the location of the peaks should not be affected. In the case of cylindrical-like pores, it is caused by the non-uniform radius of the cylinder-like shape, so the isotherms represent some sort of averaged behavior.
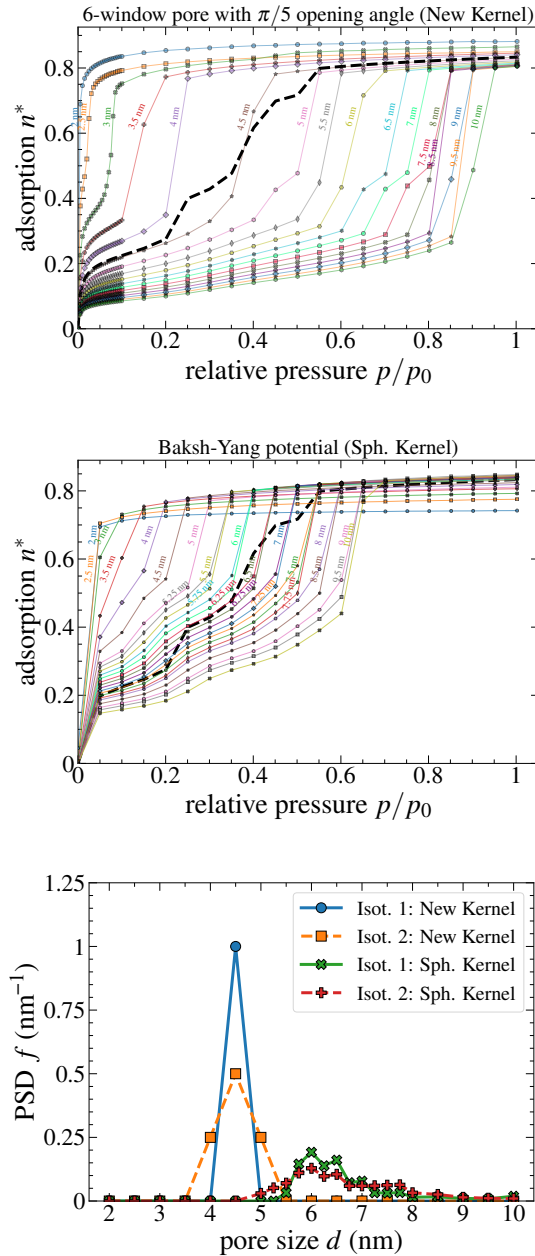
Figure 3.12 Top: A kernel of adsorption isotherms for six windows, opening angle $\delta = \pi/5$, and the sizes are shown in the labels ("New Kernel"). Test isotherm 1 is labeled as 4.5 nm; test isotherm 2, which is constructed as a linear combination of 4, 4.5, and 5 nm isotherms with 0.25, 0.5, 0.25 weights, is marked with a thick dashed line. Middle: A kernel of adsorption isotherms for spherical pores using the Baksh-Yang potential ("Sph. Kernel"). Bottom: Pore-size distribution for the test isotherms 1 and 2 obtained using the two kernels.
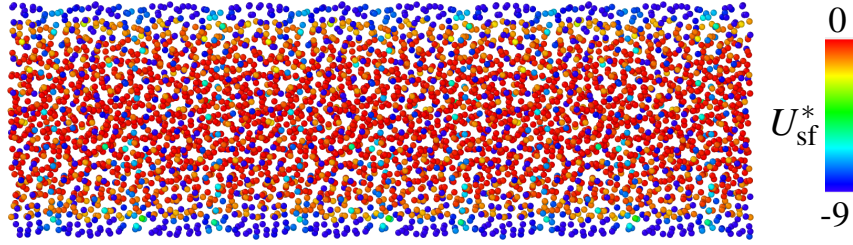
Figure 3.13 A pore with two windows with an opening angle $\delta = 0.4\pi$, which has features of both a cylinder and a sphere. The color represents the solid-fluid potential value having the lowest values near the boundary.

In the aspect of isothermal elastic modulus and compressibility, Figure 3.7 shows the linear behavior with a constant slope, which confirms the expected behavior of the Tait-Murnaghan equation [98, 99]. The larger windows correspond to lower modulus, i.e., weaker confinement effects, which is consistent with the isotherms. The only exception in terms of the trend here is the isotherm corresponding to 0.4π opening, which is between the $\pi/5$ and $\pi/3$ curves. We suggest that due to high fluctuation from the linear regression, it requires more moves to be equilibrated properly.

For greater numbers of windows, the critical opening angle property also holds true, i.e., when the isotherm for pore with an opening angle δ smaller than $\delta_c = \arccos(d_{\text{int}}/d_{\text{ext}})$ described in Section 3.2.6, we see little difference from the spherical isotherm. We also noticed a drastic effect due to the number of windows in Figure 3.8. If the number of windows is increased, the point of capillary condensation is shifted to the right. On the other hand, as the opening angle increases, the effect becomes stronger. Thus, for the opening angle $\delta = \pi/4$, the point of capillary condensation is shifted from 4 windows $p/p_0 = 0.5$ to 6 windows $p/p_0 = 0.8$. The full dependence of the capillary condensation point on the opening angle for different windows is presented in Figure 3.14. The justification for such a result is that due to the increase in the opening angle and the number of windows, the pore has a smaller solid surface the fluid can adsorb to.
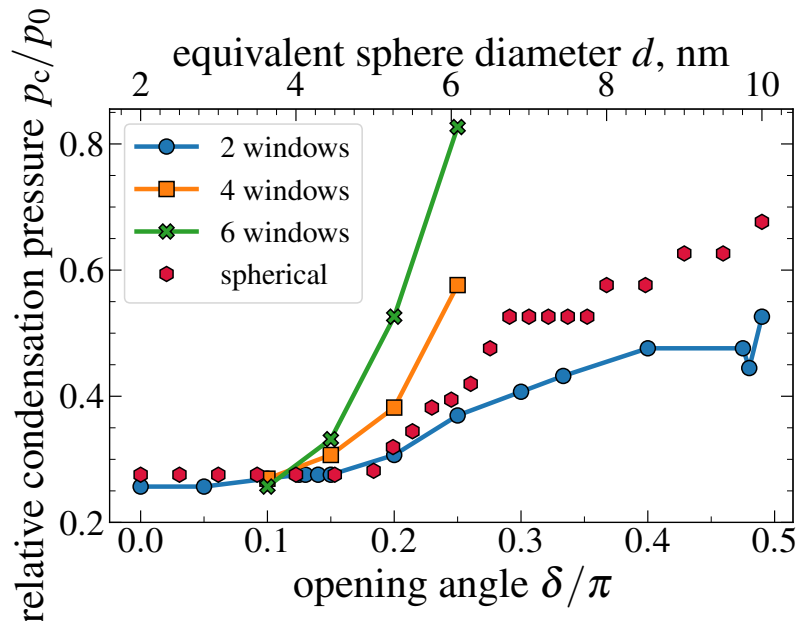
Figure 3.14 Dependence of the capillary condensation point for a single spherical pore on the pore diameter (hexagons) and for a 5 nm pore with windows on the opening angle (solid lines). The capillary condensation pressure was calculated as the argument of maximum of the derivative of density with respect to pressure.

The constructed pore-size distributions tell us that the effect is crucial for the correct estimation of the pore size and the width of the distribution, albeit we used model isotherms for the verification. In addition, the shift of the capillary condensation point we found is consistent with other papers that compared the experimental isotherms of 3DOm carbons for nitrogen adsorption [69]. In this paper, for a 3DOm carbon system with 10 nm pores, they obtained an equivalent diameter of 14 nm, which is similar to our simulation results, which mapped to 4.5-6 nm. Although we admit that the effect should be non-linear and for a different fluid, we see a clear qualitative agreement.

Our focus here was on the effect of interconnections on the capillary condensation point, the shape of the adsorption isotherm, and the PSD resulting from such isotherm. Typically, adsorption isotherms on mesoporous materials (including 3DOm carbons) have hysteresis loops [100, 73], and the adsorption branch can be used as an additional

source for PSD analysis [21]. Although we did not consider desorption isotherms here, the pore models and integrated solid-fluid potentials developed in this study can be used for these calculations as well as a possible extension of this work.

It is worth noting that even though the calculation of the integrated solid-fluid potentials presented in this chapter is done numerically, it can still save computational time for simulations in large mesopores using MC and can be utilized in DFT calculations, relying on integrated potentials. In recent years, a more rigorous approach to the calculation of the integrated potentials for molecular modeling of adsorption was proposed [101]. The idea of this method is to use a temperature-dependent effective potential based on the free energy calculations, rather than on the configurational energy. This approach was recently generalized for the 2D geometry [102] and could be applied for the two-window case of our system. However, the four-window and six-window cases, which are three-dimensional, could not be described within the 2D approach. Furthermore, due to the high surface density, the case of adsorption on 3DOm carbons should be satisfactorily described within the conservative integrated potential approach.

3.5   Conclusion

In this chapter, we proposed a model for a porous material with spherical pores connected by windows and studied the role of interconnections on the gas adsorption isotherms. We proposed a simple way to calculate the integrated potential for four and six windows that utilize only surface integrals in the spherical coordinate system. For materials with two windows, we obtained the expected smooth transition from spherical to cylindrical isotherms and studied the dependence of the opening polar angle on the shift of the capillary point. Then, we extended our problem to four and six windows, a geometry consistent with that of a real 3DOm carbon system, and found a drastic difference. We showed that the application of a kernel of spherical

isotherms for PSD calculation on isotherms for materials with six-windows noticeably overpredicts the "true" pore size. The mismatch that we demonstrated agrees with the mismatch seen in PSD of 3DOm carbon materials almost quantitatively. In addition, we identified and derived analytically the critical angle when isotherms start diverging from the spherical pore. We also carefully studied and verified the periodic effects, which we came across during implementation. Our results can be further used for modeling the adsorption of gases in the system of interconnected pores using Monte Carlo molecular simulations or off-lattice density functional theory.

MOLECULAR SIMULATIONS SHED LIGHT ON POTENTIAL USES OF ULTRASOUND IN NITROGEN ADSORPTION EXPERIMENTS [5]

Abstract

Nitrogen adsorption is one of the main characterization techniques for nanoporous materials. The experimental adsorption isotherm provides information about the surface area and pore-size distribution (PSD) for a sample. In this chapter we show that additional insight into PSD can be gained when the speed of sound propagation through a sample is measured during nitrogen adsorption experiment. We analyzed published experimental data on ultrasound propagation through a nanoporous Vycor glass sample during nitrogen adsorption experiment. Next, from the experimental isotherms from the paper, we calculated the change of the longitudinal and shear moduli of the sample as a function of relative vapor pressure. From this, we show that the shear modulus of the sample does not change upon filling the pores, evidencing that adsorbed nitrogen at 77 K has zero shear modulus [6], similarly to a bulk liquid. The longitudinal modulus [7] of the sample behaves differently: it changes abruptly at the capillary condensation and keeps gradually increasing thereafter. We performed Monte Carlo molecular simulations to predict the compressibility of adsorbed nitrogen and then calculated the longitudinal modulus of the nitrogen-saturated Vycor using the Gassmann equation. Our theoretical predictions nicely matched the longitudinal modulus derived from the experimental data. Additionally, we performed molecular simulations to model nitrogen adsorbed in silica pores of sizes ranging from 2 to 8 nm, which is close to the modeled Vycor glass sample with characteristic pore size ca.

---

[6]*Shear modulus* is defined as the ratio of shear stress to shear strain [103]

[7]*Longitudinal modulus*, also known as *P-wave modulus*, is defined as the ratio of axial stress to axial strain [103]

6-8 nm. We found that the isothermal elastic modulus of adsorbed nitrogen depends linearly on the inverse pore size. This dependence, along with the proposed recipe for probing the modulus of adsorbed nitrogen, sets up the grounds for extracting additional information about the porous samples, when the nitrogen adsorption is combined with ultrasonic experiments.

4.1   Introduction

Nitrogen adsorption is one of the main characterization techniques for nanoporous materials; an experimental adsorption isotherm provides information about the BET surface area and pore-size distribution (PSD) of a sample. Typically, adsorption isotherms are measured by volumetric or gravimetric methods; however, there could be various alternatives. In particular, Warner and Beamish proposed to use ultrasound for this purpose [1]. Their idea was based on experimental measurements of the speed of sound propagation through a porous sample during nitrogen adsorption at a constant temperature. The speed of sound in a medium depends on the medium density. Therefore, the variation of the speed of sound during the adsorption experiment can be related to the variation of the average density of the sample, i.e. the adsorption isotherm. Warner and Beamish showed that the adsorption isotherm derived from ultrasonic measurements is fully consistent with the volumetric one and is applicable for calculation of the specific surface area.

Instead of using the ultrasonic measurements as an alternative, we propose interpreting these data as complementary information to adsorption isotherm data. Knowing the adsorption isotherm from independent (e.g., volumetric) measurements allows one to predict the change of the elastic moduli (shear and longitudinal) of the porous sample as a function of nitrogen vapor pressure. On the basis of the experimental data, we show that the shear modulus of the sample is not changing, suggesting that, similarly to bulk liquid nitrogen, the shear modulus of the adsorbed

nitrogen is zero. The longitudinal modulus of the sample, however, behaves differently: while not changing appreciably at low vapor pressures, it rises abruptly at the capillary condensation point. This behavior is consistent with the ultrasonic measurements performed for other adsorbates: n-hexane [104, 105] and argon [106, 107, 108, 109].

In addition to analysis of the experimental data, we performed molecular simulations of nitrogen adsorption in silica pores of various sizes. Specifically, we performed Monte Carlo simulations in the grand canonical ensemble, which gives the isothermal compressibility of the adsorbed fluid from the fluctuations of the number of molecules in the pore [76]. The results of our simulations combined with the Gassmann equation [110] demonstrated a good agreement with the experimental data from [1]. Moreover, the simulations reveal a simple relation between the pore size and the compressibility of adsorbed nitrogen. This relation further supports that the ultrasonic experiments can be utilized for the characterization of porous materials, providing information complementary to adsorption isotherms [95, 76, 77].

4.2   Methods

Measuring the velocity of ultrasonic wave propagation is a routine way to get the elastic moduli of bulk materials. Ultrasonic methods can be applied to composites as well, and porous materials in particular [111, 112]. The key equation is the following:

$$v = (X/\rho)^{1/2} \tag{4.1}$$

where v is the velocity of the longitudinal or transverse wave propagation in the sample and ρ is the mass density of the sample. For transverse waves $X = G$ is the shear modulus of the sample and for longitudinal waves $X = M$ is the longitudinal modulus of the sample.

4.2.1 Calculation of the Porous Sample Modulus from Ultrasonic Data

Although we do not present new experimental data, but rather are focusing on the theoretical analysis of the data from [1], it is worth briefly summarizing how these data were obtained. The experiment was performed using a Vycor glass 7930 porous sample of 1-cm long and 0.3-0.5 cm across with porosity [8] $\phi = 0.286 \pm 0.001$ [113]. Vycor glass 7930 is a disordered mesoporous material with long, channel-like pores having the characteristic size of ca. 6-8 nm in diameter.

The simplified diagram of the original experiment is shown in Figure 4.1. First, the sound transit time t_0 through the dry sample was measured, corresponding to the dry shear G_0 and longitudinal M_0 moduli of the porous sample. Thereafter the vapor pressure was varied, and the corresponding relative transition time change was measured in this way:

$$\frac{\Delta t}{t_0} = \left(\frac{v}{v_0}\right)^{-1} - 1 = -\frac{\frac{\Delta v}{v_0}}{1 + \frac{\Delta v}{v_0}} \tag{4.2}$$

where v_0 and v are the speed of sound propagation for the dry and saturated samples, respectively; $\Delta v = v - v_0$; $\frac{\Delta v}{v_0} = -\frac{\theta}{1+\omega t_0}$, θ is the phase angle; ω is the sound angular frequency.

Reference [1] reported v/v_0 as a function of the relative vapor pressure of nitrogen p/p_0 (p_0 is the saturated vapor pressure). The relative change of the longitudinal modulus can be calculated from the measured relative change of the transit time and relative change of the mass of the sample [105]. Indeed, Equation (4.1) gives the longitudinal sound speed $v = \sqrt{M/\rho}$, then using the relation between the sample length L and time t as $t = L/v$, one can obtain the expression for density as a function of time t and longitudinal modulus M as $\rho(t, M) = \frac{Mt^2}{L^2}$. By expanding this function in the Taylor series and rewriting in terms of the relative change $\Delta\rho/\rho_0$, we derive an expression in terms of $\Delta M/M_0$ and $\Delta t/t_0$. Then, the replacement of $\Delta\rho/\rho_0$ to the

---

[8] *Porosity* is defined as the ratio of the volume of open pores to the total volume of the solid [10]
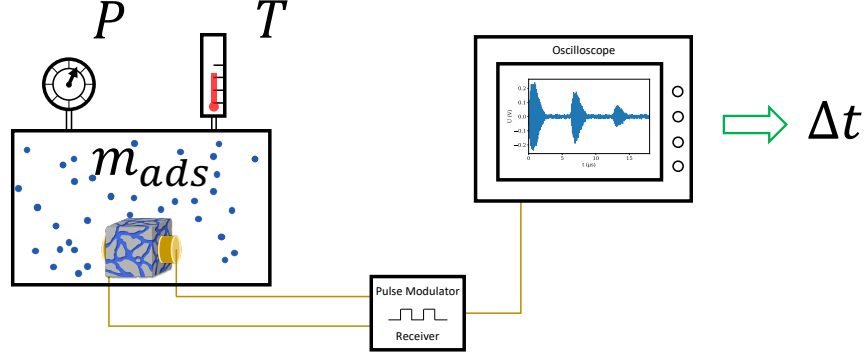
Figure 4.1 Diagram (drawn by Chris Dobrzanski in [114]) of the experiment carried out by Warner and Beamish [113]. Here the ultrasound transition time at certain at a range of pressures and constant temperature 77 K was measured and converted to an adsorption isotherm.

relative change of the sample mass $\Delta m/m_0$ gives us

$$\frac{\Delta M}{M_0} = \frac{\frac{\Delta m}{m_0} - \left[2\frac{\Delta t}{t_0} + \left(\frac{\Delta t}{t_0}\right)^2\right]}{1 + 2\frac{\Delta t}{t_0} + \left(\frac{\Delta t}{t_0}\right)^2}, \tag{4.3}$$

where m_0 and ρ_0 are the mass and density of the dry sample respectively. This equation was proposed by Page et al. (Equation 4 in [105]). In the case of transverse waves, a similar equation is valid for the shear modulus

$$\frac{\Delta G}{G_0} = \frac{\frac{\Delta m}{m_0} - \left[2\frac{\Delta t}{t_0} + \left(\frac{\Delta t}{t_0}\right)^2\right]}{1 + 2\frac{\Delta t}{t_0} + \left(\frac{\Delta t}{t_0}\right)^2} \tag{4.4}$$

where $\Delta t/t_0$ is now related to the transverse waves propagation. Equations (4.3) and (4.4) can be used to extract the moduli of the sample as a function of p/p_0.

4.2.2 Predictions of the Fluid-Saturated Sample Modulus Based on the Gassmann Theory

The ultrasonic measurements on a saturated porous sample provide the moduli M and G of the composite, which can in turn be related to the moduli of the constituents. When the pores are filled with fluid, which has zero shear modulus, the shear modulus

of the saturated sample G is equal to the modulus of the dry material G_0:

$$G = G_0. \tag{4.5}$$

When a porous sample is isotropic, the frequency of the sound wave is low, and the pores are filled with a fluid (so Equation (4.5) holds), the bulk modulus K of the saturated porous sample is related to the moduli of the constituents by the Gassmann equation [110, 115, 116]:

$$K = K_0 + \frac{\left(1 - \frac{K_0}{K_s}\right)^2}{\frac{\phi}{K_f} + \frac{1-\phi}{K_s} - \frac{K_0}{K_s^2}}, \tag{4.6}$$

where K_0 is the dry bulk modulus, K_s is the solid (pore walls) modulus, ϕ is the porosity of the sample and K_f is the fluid modulus. Note that ultrasonic measurements take place at adiabatic conditions so that the fluid modulus is taken at constant entropy. Discussion of the adiabatic vs isothermal modulus is given below. The low frequency limit for the experiment can be estimated as $f_{\max} = \frac{\eta}{\pi \rho_f \delta_{\max}^2} \simeq 1$ GHz [115], where $\delta_{\max} \approx 7 - 8$ nm is the viscous skin depth considered as the maximum pore diameter for the Vycor sample, $\rho_f = 807$ kg m^{-3} is the fluid density [49], $\eta = 163$ µPa s is the dynamic viscosity for nitrogen at temperature $T = 77$ K and pressure $P = 0.1$ MPa [117]. Therefore, the frequencies of 11 and 9.4 MHz, used in [1] for transverse and longitudinal waves, can be considered low.

Because the experimentally measured quantity is the longitudinal modulus of the composite, it is convenient to rewrite Equation (4.6) as

$$M = M_0 + \frac{(K_s - K_0)^2 K_f}{\phi K_s^2 + [(1 - \phi)K_s - K_0] K_f}. \tag{4.7}$$

If the properties of the solid and fluid constituents are known, Equation (4.7) predicts the longitudinal modulus M of the fluid-saturated sample, which is directly measured in ultrasonic experiments. While the Gassmann theory was originally proposed for

systems with macroscopic pores, recently it was shown to be applicable for nanoporous glass filled with adsorbed argon and n-hexane [118]. Parameters of the solid can be accessed experimentally and do not appreciably change during fluid adsorption [118]. For the data from [1] discussed here, the longitudinal and shear moduli of the dry Vycor sample were measured using ultrasonic experiments: $K_0 = 9.56$ GPa, and $G_0 = 7.47$ GPa [113]. The solid wall properties can be estimated based on these values and porosity $\phi = 0.286$ from the effective medium theory by Kuster and Toksöz [119], which gives $K_s = 18.5$ GPa (see the Supporting Information for [118] for details).

Finally, to use the Gassmann equation, the modulus of the adsorbed fluid has to be known, which, unlike the modulus of the solid, is noticeably affected by the confinement [95] and cannot be directly probed experimentally. Following our previous work [76, 99, 77], we calculate the modulus of confined fluid from Monte Carlo molecular simulations.

4.2.3 Calculation of the Fluid Modulus from Molecular Simulations

Thermodynamic properties of fluids in mesopores noticeably differ from the bulk fluids' properties [120]. Many of these properties can be readily calculated from molecular simulations [121]. Monte Carlo simulations in the grand canonical ensemble (GCMC) provide a direct way to calculate the isothermal compressibility β_f^T, or the reciprocal property – isothermal modulus K_f^T, of a fluid through the fluctuation of the number of molecules $\langle \delta N^2 \rangle$ [97]:

$$K_f^T = \left(\beta_f^T \right)^{-1} = \frac{k_B T \langle N \rangle^2}{V \langle \delta N^2 \rangle}, \tag{4.8}$$

where N is the number of molecules in the system, k_B is the Boltzmann constant, V is the system volume, and T is the absolute temperature. While being derived for a bulk system, Equation (4.8) is applicable for fluids confined in mesopores also, as long as the fluctuations obey a Gaussian distribution [76].

Alternatively, the isothermal modulus can also be calculated from the fluid number density $n = N/V$ as a function of pressure at the constant temperature:

$$K_f^T \equiv -V \left(\frac{\partial P}{\partial V} \right)_T = -\frac{1}{n} \left(\frac{\partial P}{\partial (\frac{1}{n})} \right)_T, \qquad (4.9)$$

where P is the pressure of the fluid. Equation (4.9) can be directly used for calculation of the isothermal modulus of a bulk fluid from an equation of state. Moreover, it can also be applied for the fluid confined in the pore if the fluid is assumed uniform, so that the Gibbs-Duhem equation applies to it. In this case, the modulus can be rewritten as [95, 77]

$$K_f^T = n^2 \frac{k_B T}{p/p_0} \left(\frac{\partial (p/p_0)}{\partial n} \right)_{V,T}, \qquad (4.10)$$

where p/p_0 is the relative pressure of the vapor. Note that Equation (4.10) calculates the modulus directly from the adsorption isotherm, which can be obtained from Monte Carlo simulations. Therefore, Equation (4.10) can be applied to the same data as Equation (4.8). Because this method uses macroscopic relations of classical thermodynamics, as opposed to the statistical mechanics expression Equation (4.8), we will call it the "macroscopic method" below.

Knowing the heat capacity ratio $\gamma = \frac{C_P}{C_V}$, it is possible to derive the adiabatic fluid modulus K_f from Maxwell's relations [122]:

$$K_f = \gamma K_f^T \qquad (4.11)$$

Following the previous works, where the isothermal modulus of confined argon K_f^T was compared to ultrasonic experimental data, we assume that γ for a confined fluid equals to γ of the bulk fluid at the same temperature [95, 118].

4.2.4 Details of Monte Carlo Simulations

We modeled thermodynamic properties of nitrogen adsorbed in spherical silica pores using the GCMC method, based on the conventional Norman-Filinov algorithm [90]. Both fluid-fluid and solid-fluid interactions were represented by Lennard-Jones (LJ) potentials, with parameters following [52]. The parameters are summarized in Table 4.1. When modeling adsorption in Vycor glass, the pores are typically represented by cylinders [123]. However, calculation of compressibility of fluids adsorbed in cylindrical pores at low temperatures may encounter artifacts related to the layering of the fluids along the walls [77]. Because the moduli of argon confined in spherical and cylindrical pores of the same size do not differ much [124, 77], in the current work we consider the spherical pores exclusively. The solid-fluid interaction potential for the spherical pore was calculated as follows [84]:

$$U_{\text{sf}}(r, R) = 2\pi n_{\text{s}}\epsilon_{\text{sf}}\sigma_{\text{sf}}^2$$

$$\times \left\{ \frac{2}{5} \sum_{i=0}^{9} \left[\frac{\sigma_{\text{sf}}^{10}}{R^i (R-r)^{10-i}} + \frac{\sigma_{\text{sf}}^{10}}{R^i (R+r)^{10-i}} \right] \right.$$

$$\left. - \sum_{i=0}^{3} \left[\frac{\sigma_{\text{sf}}^4}{R^i (R-r)^{4-i}} + \frac{\sigma_{\text{sf}}^4}{R^i (R+r)^{4-i}} \right] \right\}, \tag{4.12}$$

where n_{s} is the surface number density of solid LJ sites, r is the distance from the center of the pore, and R is the radius of the pore, corresponding to the "external" diameter d_{ext} (the distance between the centers of the furthest solid atoms). The "internal" diameter, corresponding to the volume V used for density and modulus calculations, is related to the external diameter d_{ext} as [74]:

$$d_{\text{int}} \approx d_{\text{ext}} - 1.7168\sigma_{\text{sf}} + \sigma_{\text{ff}}, \tag{4.13}$$

where σ_{sf} and ϵ_{sf} are Lennard-Jones parameters for solid-fluid interactions.

The simulations were run at $T = 77$ K to match the experimental conditions of [1]. The simulations carried out for the pores with external diameters of $2 - 10$ nm

Table 4.1 Lennard-Jones (LJ) Parameters and Relevant Physical Properties for the N$_2$-N$_2$ Fluid-Fluid (ff) and SiO$_2$-N$_2$ Solid-Fluid (sf) Interactions

interaction	σ (nm)	ϵ/k_{B} (K)	n_{s} (nm^{-2})	r_{cut} (σ_{ff})
N$_2$-N$_2$	0.36154	101.5	-	5.0
SiO$_2$-N$_2$	0.317	147.3	15.3	-

Note: σ is the LJ diameter, ϵ is the LJ energy scale, n_{s} is the surface number density of solid LJ sites, r_{cut} is the distance at which the interactions were truncated; no tail corrections were used. All parameters are taken following [52].

with 1 nm step interval. For each pore size, 2.5×10^9 equilibration trial moves and 5×10^9 production trial moves were performed. The chemical potential at saturation point μ_0^* was derived from the Johnson et al. equation of state [92] and equal to -9.596 (hereinafter the asterisk stands for the reduced LJ units). The reduced chemical potential was varied from -18.33 to μ_0^* with a fixed step per pressure. For 7 and 8 nm pores, 11 extra points were calculated for p/p_0 from 0.7 to 1.0.

4.3   Results

4.3.1   Fluid Modulus from Molecular Simulations

Figure 4.2 shows the adsorption isotherms of nitrogen at $T = 77$ K calculated using GCMC for a series of pore sizes. For each of the isotherms, we identified the points above the capillary condensation and used them to calculate the isothermal modulus of the fluid using Equation (4.8) and 4.10. The resulting moduli are shown in Figure 4.3 as a function of relative pressure p/p_0. Figure 4.3 demonstrates a good agreement between the moduli calculated from the fluctuation of the number of particles and from the slope of the isotherm.

It is instructive to present the calculated moduli as a function of the Laplace (capillary) pressure in the pores, calculated as

$$P_{\mathrm{L}} = \frac{R_{\mathrm{g}}T}{V_{\mathrm{l}}} \log\left(\frac{p}{p_0}\right). \tag{4.14}$$

Here R_g is the gas constant, and $V_l = 34.7\,\mathrm{mL\,mol^{-1}}$ is the molar volume of the liquid phase. Figure 4.4 shows the isothermal fluid modulus as a function of Laplace pressure and demonstrates the linear dependence for each of the pore sizes. The corresponding coefficients for the linear regression for these data, as well as for the reference data for bulk liquid nitrogen, can be found in Table 4.2. To calculate the adiabatic elastic modulus from the reference data, we used the relation with the speed of sound v and the density of the sample ρ, $K_f = \rho v^2$, which is then divided by γ to get the isothermal modulus.

The values of v and ρ at $T = 77$ K and P between 0.1 and 0.2 MPa were brought from the reference data [49] and accessed using the CoolProp thermophysical property database [48]. The heat capacity ratio γ is equal to [49] 1.878. The fluid modulus-pressure dependence $K_f^T(P)$ was obtained using the relation between pressure and density $P^*(n^*)$ in the Johnson equation provided by Equation 7 from [92]. The saturation pressure corresponds to the liquid phase at the point of saturated liquid $\mu_{\mathrm{ex}}^* = -4.181$ and $n^* = 0.811$.

Each of the last points in the curves shown in Figure 4.4 gives the fluid modulus at saturation $(p/p_0 = 1)$. These points are plotted separately as a function of the pore size in Figure 4.5. The regression shows the linear trend on the inverse pore diameter with the intersection with the bulk value at $d_{\mathrm{ext}} \approx 10$ nm.

4.3.2 Analysis of the Ultrasonic Data

Once the properties of confined nitrogen are known, we can combine them with the properties of the solid using the Gassmann equation and compare to the moduli derived from the ultrasonic measurements using Equations (4.3) and (4.4). Although our molecular simulations do not predict the shear modulus of the confined fluid, we expect it to remain zero taking it as an assumption based on that it is zero for any bulk fluid [125, 118]. Figure 4.6 shows the relative change of the shear modulus of
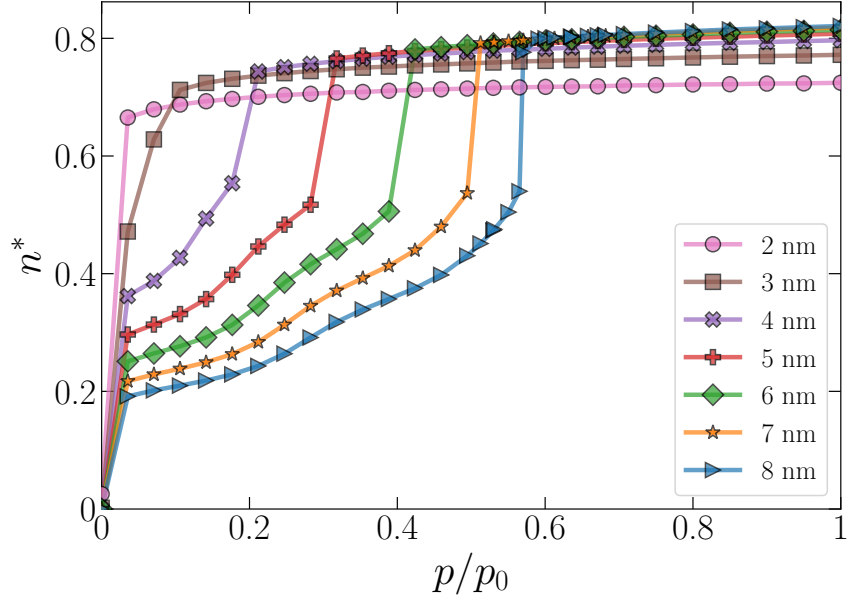
Figure 4.2 Nitrogen adsorption isotherms at $T = 77$ K for spherical silica pores of different sizes calculated using GCMC.

the sample, calculated using Equation (4.4), where $\Delta m/m_0$ is taken from volumetric adsorption isotherm and $\Delta t/t_0$ from the transverse wave propagation. Although it deviates from zero, comparison with the change observed for the longitudinal modulus is drastic.

Figure 4.7 shows the calculations of the longitudinal modulus of the sample as a function of nitrogen vapor pressure in three different ways. The red solid line shows the calculations using Equation (4.3) based on ultrasonic data exclusively: $\Delta m/m_0$ is taken based on the transverse wave propagation (assuming the shear modulus constant) and $\Delta t/t_0$ from the longitudinal waves. The black dotted line is also obtained using Equation (4.3), but is based on both ultrasonic and volumetric data: $\Delta m/m_0$ is taken from volumetric adsorption isotherm and $\Delta t/t_0$ from the longitudinal waves. Lastly, the theoretical values (green dashed line) were calculated using the fluid modulus predicted by GCMC (Equation (4.8)) and substituted into the Gassmann
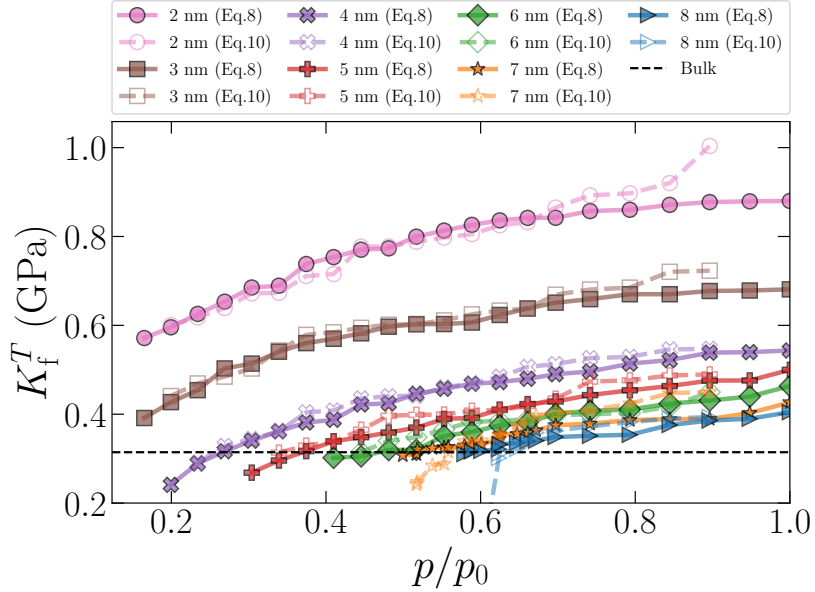
Figure 4.3 Isothermal modulus of nitrogen adsorbed in spherical silica pores of different diameters as a function of relative gas pressure. The dashed lines show the calculations based on the macroscopic thermodynamics (Equation (4.10)), and the solid lines show the calculations based on the statistical mechanics (Equation (4.8)) approach.

equation (Equation (4.6)). Figure 4.7 shows a good agreement between the theoretical predictions and the experimental data.

4.4 Discussion

The first thing worth discussing is the change of shear and longitudinal moduli of the porous sample, calculated based on the experimental data from [1] without even involving any modeling. Bulk fluids have zero shear, however, the shear modulus of a fluid in nanoconfinement can be nonzero [126]. Yet our analysis of the ultrasonic data on liquid nitrogen confined in Vycor nanopores suggests that there is no difference comparing to the bulk fluid behavior. Figure 4.6 shows that the relative change of the shear modulus does not exceed 1%. Moreover, this plot shows a near-constant shift with respect to zero, and it does not reveal any specific trend. The origin of this shift could be due to a small systematic error in the volumetric adsorption measurements; Warner
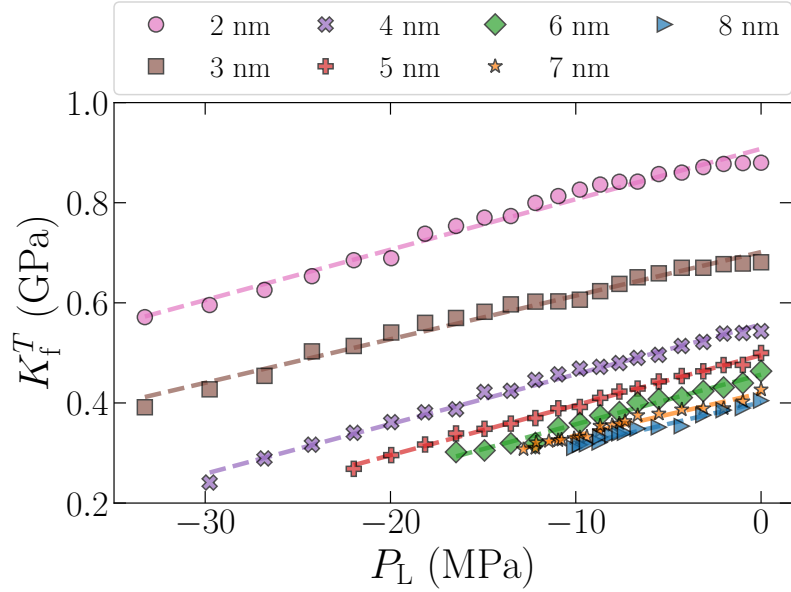
Figure 4.4 Isothermal fluid modulus K_f^T of nitrogen in spherical pores of different sizes calculated using Equation (4.8) as a function of the Laplace pressure. The dashed lines are their linear regression; see Table 4.2 for the linear regression coefficients.

and Beamish mentioned the relatively low accuracy of their volumetric adsorption isotherm [1]. This result is consistent with the recent observations by Schappert and Pelster, who reported a negligible change of the shear modulus of Vycor glass during adsorption of argon [106, 108, 127] and oxygen [128] near their normal boiling points. Zero shear of confined fluid is crucial for the data analysis, since then the experimental data on shear wave propagation can be used as a measure of change of sample mass. Moreover, zero shear is the necessary condition for using the Gassmann equation [110]. Finally, the change of the shear modulus of a fluid-saturated sample with temperature has been often used as an indication of the onset of the solid-liquid phase transition [129, 130, 131, 132, 133, 134].

We calculated the longitudinal modulus of the sample from the experimental data in two different ways: first – based on ultrasonic data exclusively (longitudinal and transverse waves) and, second, based on ultrasonic data for the longitudinal waves and volumetric adsorption data. The results of these calculations are shown

Table 4.2 Dependence of Isothermal Fluid Modulus K_f^T on P_L for Different Pore Sizes d_{ext}

d, nm	α	K_i^T, GPa	method
bulk	7.30	0.314 (0.315)	reference data [49, 48]
bulk	8.08	0.298 (0.294)	Johnson et al. EOS [92]
2	10.64 ± 0.61	0.853 ± 0.009	GCMC
3	9.71 ± 0.73	0.654 ± 0.011	GCMC
4	10.66 ± 0.46	0.499 ± 0.005	GCMC
5	10.45 ± 0.49	0.434 ± 0.004	GCMC
6	9.88 ± 1.20	0.392 ± 0.007	GCMC
7	11.12 ± 2.15	0.371 ± 0.008	GCMC
8	12.07 ± 1.32	0.352 ± 0.003	GCMC

Note: Parameter α is the slope, K_i^T is the intercept of the corresponding linear regression with the related 95% confidence intervals calculated as double standard errors. For bulk, the value in parentheses is K_f^T at 1 atm.

in Figure 4.7 by solid red line and dotted black line respectively. The calculations based on ultrasonic data exclusively show no change of the longitudinal modulus of the sample, prior to the vicinity of the capillary condensation point. For the same range of pressures, the calculations based on volumetric adsorption isotherm show the increase of the sample modulus by $\sim 0.5\%$, similar to the apparent increase observed for the shear modulus in Figure 4.6, which most likely originates from a systematic error in the volumetric adsorption measurements. Note that the curves corresponding to volumetric and ultrasonic measurements diverge by a nearly constant shift of less than 0.01 in the whole range of pressures. However, in contrast to the "volumetric" line, the "ultrasonic" curve in the pressure range below the capillary condensation is about zero as expected. This is in line with the main message of the original work by
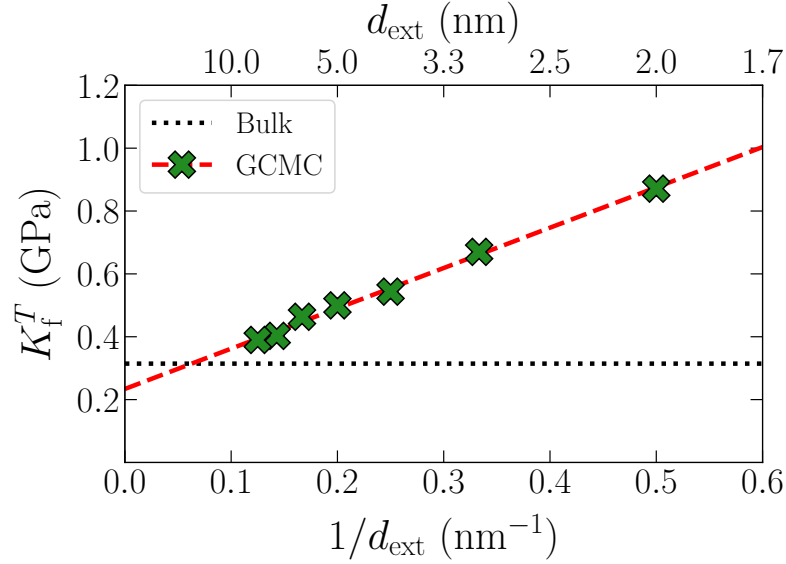
Figure 4.5 The green cross marks are the elastic modulus at saturation ($p/p_0 = 1$) for nitrogen at 77 K in pores of various sizes, calculated from GCMC simulations. The red dashed line is their linear regression, the black dotted line $K_f^T = 0.314$ GPa is the elastic modulus calculated from the reference data for the bulk liquid nitrogen [49].

Warner and Beamish: the ultrasonic measurements employed for the calculation of the sample mass provide higher precision than a conventional volumetric isotherm [1].

The experimental curves show that after the capillary condensation the longitudinal modulus changes abruptly and then continues to gradually increase, which is fully consistent with our theoretical interpretation. Moreover, we show a quantitative agreement between the experimental results and the theoretical predictions obtained using the Gassmann equation and GCMC simulations (green dashed line in Figure 4.7). The difference in the capillary condensation point is due to the spherical pore model used in Monte Carlo simulations, which is known to predict the capillary condensation at the lower relative pressure than in the cylindrical pores [19, 66]. The only feature of the experimental curves which is not reproduced here theoretically, is the small decrease of the longitudinal modulus of the sample below the M_0 value (the negative region in Figure 4.7). The decrease of the modulus below the dry value
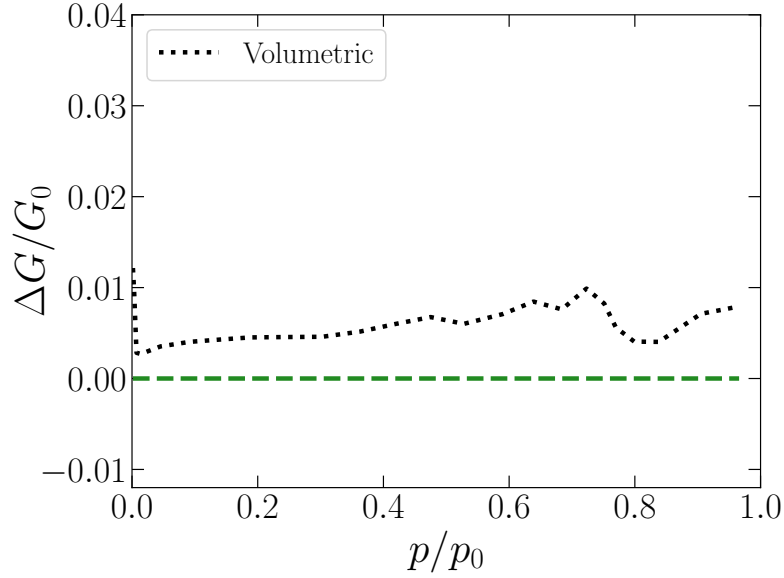
Figure 4.6 Relative change of the shear modulus of a sample during nitrogen adsorption derived from experimental data using Equation (4.4). The green dashed line, corresponding to zero change, presents the expected value for fluid.

is not physical within the Gassmann equation. This apparent decrease is likely to come from assuming the sample always uniform on the wavelength length scale. This assumption could be violated, at the onset of the capillary condensation, when some pores remained empty, while others get filled. Note that a similar dip is seen on the shear modulus data in Figure 4.6. Moreover, this feature was observed for the moduli of Vycor glass saturated with n-hexane [105] and argon [108].

Good agreement of the theoretical results with the measured longitudinal modulus supports the chosen model, namely, the applicability of the Gassmann equation to nanoporous Vycor glass, applicability of the Kuster-Toksöz effective medium theory for calculation of the solid modulus K_{s} of Vycor, and calculation of compressibility of adsorbed nitrogen based on the GCMC simulations. Therefore, it is worth discussing the rest of the theoretical results, even though not all of them can be compared to experimental data.
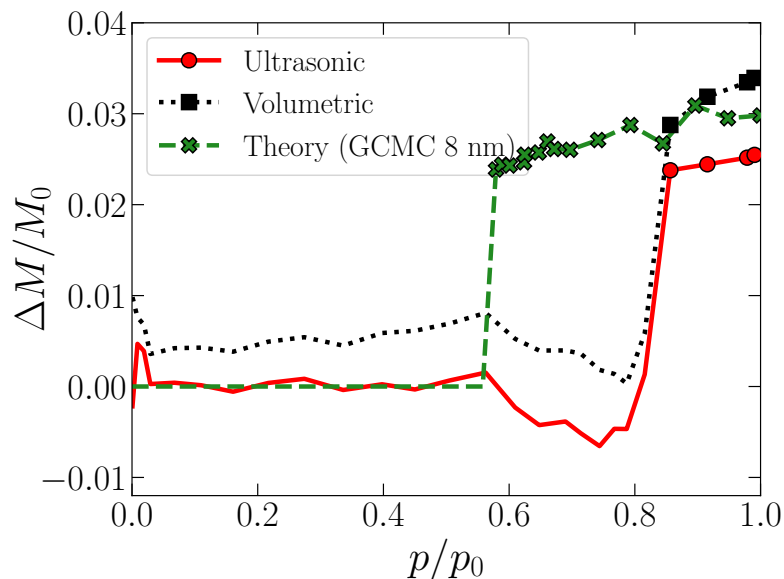
Figure 4.7 Relative change of the longitudinal modulus of a sample during nitrogen adsorption. The red solid line gives the modulus calculated based on the ultrasonic data for longitudinal and shear waves using Equation (4.3). The black dotted line gives the modulus calculated from the combination of ultrasonic data (for longitudinal waves) and volumetric data for the mass change. The green dashed line gives the theoretical predictions. Both experimental curves are calculated based on the data from [1].

From the consideration of our molecular simulation results, we can first conclude that the Lennard-Jones model for nitrogen molecules with the same parameters as established in adsorption literature [135, 52] describes well the compressibility of bulk liquid nitrogen, with the 7% deviation between the theoretical and experimental values (see first two rows in Table 4.2). The calculated compressibility (or isothermal modulus) or nitrogen adsorbed in model silica pores noticeably differ from the bulk. This difference has two distinct trends that can be seen in Figure 4.3: dependence on the relative vapor pressure (for each given pore size) and on the pore size (at any constant vapor pressure).

The physical meaning of the first trend is clear when the data are shown in logarithmic scale on vapor pressure, or even better as a function of Laplace pressure in

the pores (see Figure 4.4). The simulation results demonstrate a linear dependence of isothermal fluid modulus on Laplace pressure in the interval between -30 and 0 MPa. The linear dependence of the isothermal modulus of *bulk* fluid on pressure is known for decades [136], and is often termed the Tait-Murnaghan equation. The results in Figure 4.4 show that adsorbed nitrogen also satisfies this equation. Table 4.2 shows that the slope α in the Tait-Murnaghan equation is nearly the same for the simulations in various pore sizes. Moreover, the slope α calculated for confined nitrogen does not deviate much from the value of α for the bulk liquid argon. Finally, the slope is close to the values calculated recently for argon adsorbed in model silica nanopores [99]. This is in line with the discussion of this slope being the same for most of the bulk liquids [98]. The range of Laplace pressures for these data is quite moderate, being within 10% of the isothermal fluid modulus, which explains the validity of the linear approximation for the pressure dependence of the modulus. If higher (by absolute value) Laplace pressures could be realized, it would be likely to observe the deviation from the linear behavior. Finally, we should note that we use an intuitive concept of "Laplace pressure" to be consistent with a classical picture of capillary condensation/evaporation, which involves meniscus. Strictly speaking, the liquid in the spherical pore in our simulation does not have a meniscus, and the Laplace pressure should be interpreted as a pressure difference due to the difference in chemical potential, determined by the Gibbs-Duhem equation.

The other trend, seen in Figure 4.5, is worth a separate discussion, as it clearly shows another linear dependence: GCMC simulations predict that the isothermal modulus of adsorbed nitrogen changes linearly with the inverse pore size. The slope of this dependence is quite steep, so that the modulus of nitrogen adsorbed in 2 nm pore exceeds the modulus of the bulk liquid nitrogen almost by a factor of 3. This linear dependence resembles another well-known linear dependence of a thermodynamic property on inverse pore size – the temperature of freezing of liquid in a pore, given by

73

the Gibbs-Thomson [137] equation. Note that we do not expect that the linear trend will continue up to macropores, but rather expect it to start flattening around the bulk value of modulus at the pore sizes > 10 nm. Unfortunately, GCMC simulations in such large pores become prohibitively slow and do not allow one to get a good-quality distribution for calculating the isothermal modulus.

The importance of the predicted linear trend for the modulus of nitrogen adsorbed in the pores stems from the fact that this modulus can be probed experimentally. The combination of Equations (4.3) and (4.7) allows one to extract the average value of the modulus of nitrogen within the pores from the experimental values of the transition times of the ultrasonic waves. Knowing the linear dependence of the modulus in the pores on the pore size, the extracted value could serve as a basis for calculation of the pore-size distribution (PSD) of the sample, similarly to the values of capillary condensation pressures used for calculating the PSD based on nitrogen adsorption isotherm [2] or depression of the freezing point of confined liquid, used as a basis of thermoporometry [138]. While the modulus at $p = p_0$ can be used only as an estimate for the average pore size, the "modulus isotherm", i.e., the modulus as a function of p/p_0, can be employed to calculate the PSD. This can be done similarly to a solution of an adsorption integral equation using an adsorption isotherm [139, 140] or strain isotherm [141, 142]. This task would require calculation of a kernel of modulus isotherms and testing it on a representative set of experimental data collected for well-described samples. The experimental data published to date are insufficient for performing this task.

Notwithstanding a good agreement between our theoretical results and experimental data, the model can be made more rigorous. The gap between theoretical and ultrasonic curves was about 15%, which is not negligible. Even the modulus calculated for the bulk liquid nitrogen based on the EOS for LJ fluid [92] showed 7% deviation from the experimental value. In contrast, the modulus predicted by the

same EOS for argon at 87.3 K is 0.479 GPa, which deviates from the argon reference data [143] by only 3%. Therefore, this discrepancy is a consequence of the single-site LJ representation of nitrogen molecules. We expect that a more advanced model for nitrogen molecule, taking into account the diatomic structure, could provide a better agreement with experimental data. A TraPPE three-site model could be considered as a potential candidate [144]. However, if nitrogen is represented this way, the pore structure has to be consistent, requiring detailed atomistic representation of the silica surface. Such changes of the model are possible; however they would require additional lengthy simulations, which are beyond the scope of the current work. Finally, further improvement of the theoretical model can be achieved by a more precise calculation of the solid modulus K_s used in the Gassmann equation

4.5   Conclusion

In this chapter we revisited the idea of measuring the speed of sound propagation during nitrogen adsorption experiments. However, unlike Warner and Beamish, who suggested to use the ultrasonics as an alternative method for measuring the adsorption isotherm [1], here we propose to extract complementary information from these measurements. From the experimental data in [1], we calculated the longitudinal and shear moduli of the porous sample as a function of nitrogen vapor pressure. We showed that the shear modulus of the sample does not appreciably change when the pores get filled with nitrogen and thus concluded the adsorbed nitrogen has zero shear modulus as if it is a bulk liquid. The longitudinal modulus of the sample behaves differently: while not changing at low relative vapor pressure, it rises abruptly at the capillary condensation point and continues to gradually increase thereafter. We proposed a theoretical model that explains this behavior and matches the experimental curve. Our model is based on the Gassmann equation, in which the compressibility of adsorbed nitrogen is calculated based on GCMC simulations. Good agreement

between the model and experimental data justifies the predictions of our molecular simulation model beyond the system in the considered experiment. Thus, we simulated nitrogen adsorbed in mesopores of various sizes and calculated its isothermal elastic modulus. One of the key results of our simulations is the linear dependence of the isothermal modulus of adsorbed nitrogen on the inverse pore size. This dependence provides an unambiguous relation between the pore size and the modulus, which can be probed experimentally using ultrasound. Therefore, our results set up the grounds for extracting additional information about the porous samples, when the nitrogen adsorption is combined with ultrasonic experiments.

CHAPTER 5

KINETIC MONTE CARLO: MAKING MOLECULAR SIMULATIONS OF ADSORPTION MORE EFFICIENT

5.1 Introduction

Phase equilibrium, and vapor-liquid equilibrium (VLE) in particular, plays an important role in separation and purification processes in chemical, material, and pharmaceutical industries, understanding living organisms in biology, and even in climate modeling [145]. Thus, for a proper design of such processes, one has to provide theoretical models that give quantitative predictions of thermodynamic data. It is especially true for the distillation process, which can consume plenty of energy, so such knowledge of how to separate the mixtures easier could make the distillation column much more energy-efficient. Another motivation for such methods is that since there is a significant number of mixtures one can mix, the experimental data can be unavailable for a specific mixture of species [146]. Therefore, understanding how to model such processes is of utmost importance for chemical engineers.

There are three requirements for the thermodynamic equilibrium: equality of temperatures (thermal equilibrium), partial pressures of each component (mechanical equilibrium), and the Gibbs free energy (chemical equilibrium); see Figure 5.1 as an illustration. The thermodynamic data for VLE, such as vapor pressure, liquid density, and fugacity, can be predicted using different equations of state (EOS). The simplest analytical one is the cubic EOS [147], such as van der Waals, Soave-Redlich-Kwong, and Peng-Robinson equations. However, despite their relative simplicity, the cubic EOS cannot give an acceptable prediction for multicomponent mixtures behavior, especially for Water/Hydrocarbon mixtures [148]. For this reason, more advanced equations of state, based on statistical mechanics theories (e.g., Statistical Associating Fluid
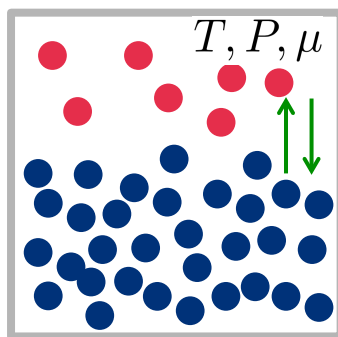
Figure 5.1 Vapor-liquid equilibria interface.

Theory (SAFT) [149] and its extension, Perturbation Theory SAFT (PC-SAFT) [150])
were developed.

Alternatively to experiments and related to them the analytical theories,
molecular simulations can provide many advantages. The first advantage of simulations
over experiments is that one can carry out in-silico experiments cheaply and safely,
without involving toxic chemical species. The second advantage is one can scale
computer simulations and adjust many values of different parameters rather than doing
a huge number of experiments or automating the experimental process. Furthermore,
one can generate so-called "pseudo-experimental" data for future research [151]. The
third advantage is that we can test our theory for an experiment that nowadays is
not technically possible. For instance, molecular simulation methods have already
proven themselves in material science and biological research as an apt discovery tool
in nanofabrication processes [151]. In addition to that, simulations can act as a great
tool to verify the hypotheses and assumptions of the theory [152].

Nowadays, due to the advances in hardware and algorithms, molecular
simulations play an important role in many areas of chemical engineering, such
as drug design, the synthesis, design, and characterization of advanced materials,
protein folding and aggregation, and many other areas [153]. Moreover, in some
areas, it has even become a routine tool for chemical engineers. However, since

the computational complexity, many scientific and engineering problems still remain unsolved.

The primary goal of molecular simulations is to predict the macroscopic thermodynamic and transport properties of a system from the given the molecular-level description as an input. Let us consider some conventional ways to carry out such a molecular simulation. Nowadays, there are two main methods, which are the Monte Carlo and molecular dynamics methods. Although they both consider evolution of a configuration, they handle the evolution of the microstates in different ways. The molecular dynamics method is based upon solving Newton's laws of motion, whereas the Monte Carlo method is based on the importance sampling for the Boltzmann distribution.

Specifically, this chapter is going to discuss the use of Monte Carlo techniques for the calculation of vapor-liquid equilibrium and their performance aspects. It starts with a discussion of conventional canonical ensemble and grand canonical ensemble Monte Carlo [90, 152]. Later, we discuss the kinetic Monte Carlo algorithm for vapor-liquid equilibria recently introduced by Ustinov and Do [154]. The main advantage of this method is that one can calculate certain properties easier and less computationally expensive. One of the examples where the algorithm has an advantage is the calculation of chemical potential in the canonical ensemble. In the classical scheme, for a given configuration, to calculate chemical potential, one needs to utilize the Widom test particle insertion (or deletion) method [155, 152] or its modifications, which can be very computationally expensive in the dense states [156]. In the kinetic Monte Carlo algorithm, on the other hand, it can be calculated at constant time, meaning that the asymptotic time complexity does not depend on the number of particles in the system. Other advantage is that the scheme works even with low-dense liquid since there is no reason to delete or remove particles.

The Kinetic Monte Carlo algorithm is aimed to simulate the stochastic evolution of some process from an initial state by known rates of occurrence of events r_i. The term kinetic Monte Carlo (kMC) was coined in 1993, although the algorithm was proposed earlier, referred to as the Dynamic Monte Carlo (DMC) method [157]. The scheme is often applied for stochastic reaction modeling, in particular for problems of vacancy diffusion, grain growth, film deposition [158], birefringence [159], and biological pattern formation [160].

5.2   Methods

5.2.1   Calculation of Energy

Let us discuss different molecular-level models. In the ideal world, one would probably prefer to model taking into account all bonds interaction, many-body interactions, chemical reactions [97], and other contributions. However, for many problems, it requires lots of computational resources and with current hardware and algorithms, the solution to this problem is not always feasible within the reasonable time limit. However, we can neglect some interactions for certain systems and still obtain an acceptable model. Depending on what the system is, one can build different molecular-level models. Let us examine the most conventional models for such interactions and their assumptions.

In general, an interatomic potential can be represented as a sum of many-body potentials

$$U \approx \sum_i U_1(r_i) + \sum_{i<j} U_2(r_{ij}) + \sum_{i<j<k} U_3(r_{ijk}) + ...,$$

where U_1 is the one-body potential, U_2 is a pairwise potential, U_3 represents the energy of triplets, etc. In this work, only the terms up to third one will be considered.

The first term, i.e., the bonded interactions, is represented as a sum of the bond, valence angle, and torsional (dihedral) angle deformation energy [161]. Bond
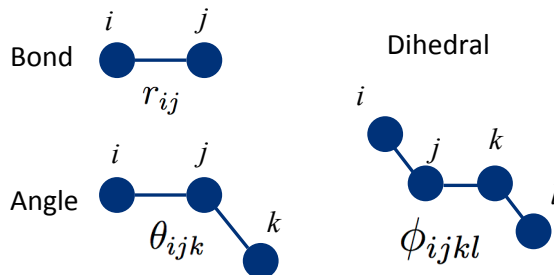
Figure 5.2 Bond, valence angle and torsion angle deformation energy calculation.

deformation energy is modeled by Hooke's law $U_{\text{bond}} = \sum k_{ij}^{\text{bond}}(r_{ij} - r_0)^2$, where r_0 is the reference bond length, r_{ij} is the distance between atoms (see Figure 5.2). Similarly, for valence angles θ the potential would be $U_{\text{angle}} = \sum k_{ijk}^{\text{angle}}(\theta_{ijk} - \theta_0)^2$. Finally, dihedral angles ϕ energy is represented by $U_{\text{dihedral}} = \sum k_{ijkl}^{\text{dihedral}}(1 + \cos(m(\phi_{ijkl} - \phi_0)))$, where m is a constant called periodicity. Taking these aforementioned terms for energy related to bond deformation, valence and dihedral angles into account is important for complex molecules, like alkanes.

For some systems, such as metals [152], it is important to take into account many-body interactions. In its simplest case, the three-body potential looks like $U \approx \sum_i U_1(r_i) + \sum_{i<j} U_2(r_{ij}) + \sum_{i<j<k} U_3(r_{ijk})$. However, it drastically increases the computational cost. Nevertheless, there are some parallel decomposition schemes that allow calculating the interaction much more efficiently [162]. For most of the other systems relevant to chemical engineering, such as alkanes, this and further terms can be neglected, and the pair potentials would be sufficient.

Let us now consider the most commonly used pairwise potential, neglecting the interaction between triplets, etc.

$$U \approx \sum_i U_1(r_i) + \sum_{i<j} U_2(r_{ij}) \tag{5.1}$$

Typically, the nonbonded interaction is represented as a sum of electrostatic, London dispersion, and Pauli repulsion terms. The electrostatic potential can be described
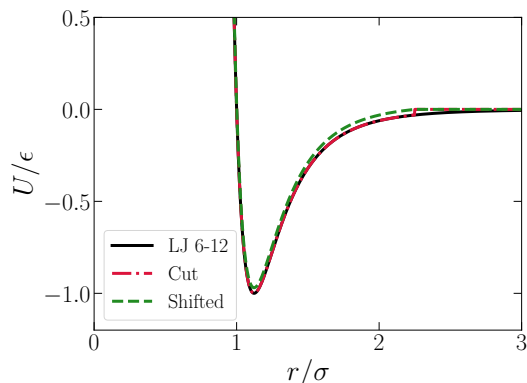
Figure 5.3 LJ potential, its cut and shifted versions.

by Coulomb's law $U_{ij} = const \cdot \frac{q_i q_j}{r}$, where q_i are the corresponding partial charges, *const* is a unit system-specific constant. Analyzing the experimental data, a simple function can fit the interaction between two nonbonded atoms by the Lennard-Jones (LJ) 12-6 potential:

$$U_{ij} = 4\epsilon \left\{ \left(\frac{\sigma}{r}\right)^{12} - \left(\frac{\sigma}{r}\right)^{6} \right\},$$

(5.2)

where r is the interaction distance, constant ϵ is the depth of the potential well, constant σ is the distance where the potential equals zero. The r^{-12} term can be interpreted as a Pauli repulsion term, the r^{-6} one represents the attraction term, London dispersion forces. The potential captures the qualitative behavior of interaction between particles and is consistent with the van der Waals equation of state. However, for illustrative purposes, here we will limit our consideration with LJ potential only.

In simulations, in order to reduce the computational cost, a fairly common approach is to truncate the potential in this way:

$$U_{ij} = \begin{cases} 4\epsilon \left\{ \left(\frac{\sigma}{r}\right)^{12} - \left(\frac{\sigma}{r}\right)^{6} \right\}, & r \leq r_c \\ 0, & r > r_c, \end{cases}$$

(5.3)
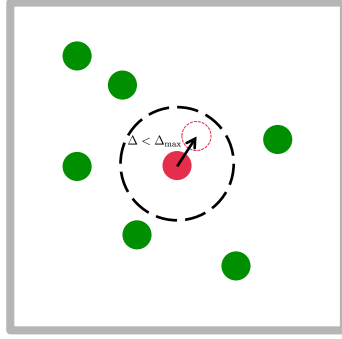
Figure 5.4 Illustration of the Metropolis et al. MC scheme. In the NVT ensemble, an arbitrary particle is chosen and then attempted to be randomly displaced at $\boldsymbol{r'} = \boldsymbol{r} + \boldsymbol{\Delta}$, $\Delta < \Delta_{\mathrm{max}}$.

where r_{c} is the cutoff radius. The potential is plotted in Figure 5.3. Below we focus on the algorithms for LJ fluids (fluids where the intermolecular interaction is described using Lennard-Jones potential) for the sake of simplicity and brevity. However, most of the algorithms described in the report either have been generalized or can be generalized for more complex molecules.

5.2.2   Basics of MC Algorithm

The original Metropolis et al. MC algorithm [163] lies upon the Boltzmann distribution and finding the most efficient energy state, i.e., the state with the lowest energy. From statistical mechanics, for the canonical (NVT) ensemble and assuming the ergodic hypothesis, one can estimate an average of a property F using the following ratio:

$$\langle F \rangle_{NVT} = \frac{\int \mathrm{d}r e^{-\beta U} F}{\int \mathrm{d}r e^{-\beta U}}, \tag{5.4}$$

where $\beta = \frac{1}{k_{\mathrm{B}}T}$ is the Boltzmann factor, k_{B} is the Boltzmann constant, T is absolute temperature.

Metropolis et al. proposed a simple and efficient scheme to calculate this ratio. Rather than taking the integral by probability density at each point, they proposed a random walk and proved its correctness. Briefly, the algorithm pseudorandomly generates a non-overlapping initial configuration of molecules and then iteratively

changes the position of particles with a certain statistical bias based on Boltzmann distribution for a large enough number of steps to equilibrate. The schematic is given in Figure 5.4 and pseudocode is provided in Algorithm 1. After running the algorithm, one can estimate an average of an arbitrary property F after M moves using a discrete version of Equation (5.4) :

$$\langle F \rangle_{NVT} \approx \frac{1}{M} \sum_{j=1}^{M} F_j. \tag{5.5}$$

Algorithm 1 The original Metropolis et al. scheme.
1: Choose an arbitrary initial configuration of molecules

2: **for** each move **do**

3:    Select a particle at random (uniformly)

4:    Calculate its energy $U(\boldsymbol{r})$ using Equation (5.3)

5:    Attempt a uniform random displacement $\boldsymbol{r}' = \boldsymbol{r} + \boldsymbol{\Delta}$, $\Delta < \Delta_{\mathrm{max}}$

6:    Calculate the corresponding energy $U(\boldsymbol{r}')$ for the new configuration

7:    Accept the new configuration with probability $\min\left(1, \mathrm{e}^{-\beta[U(\boldsymbol{r}')-U(\boldsymbol{r})]}\right)$

8: **end for**

5.2.3   Grand Canonical Monte Carlo

Many systems cannot be represented by a canonical ensemble due to the necessary exchange of the molecules. An important example would be an adsorption process described in Figure 5.5. In this section, a Monte Carlo technique that allows simulating a system in the grand canonical $(\mu V T)$ ensemble will be considered. The ensemble represents a fixed volume system in contact with a thermostat with constant temperature T and a particle exchange reservoir with fixed chemical potential μ.
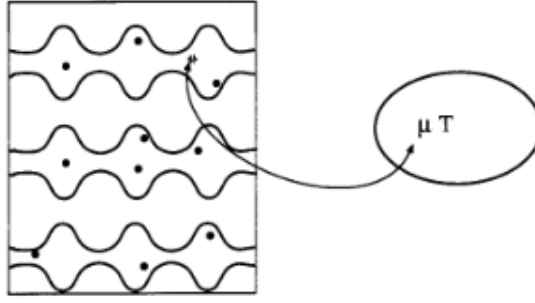
Figure 5.5 Modeling gas adsorption in a zeolite framework [152], which requires the exchange of particles with a reservoir. The thermodynamic equilibrium is reached between the gas in the reservoir and the adsorbed gas. The dots are gas molecules, the bends represent the geometry of an adsorbent sample.

An average of a property F in this case can be obtained by the following expression:

$$\langle F \rangle_{\mu VT} = \frac{\sum_{N,j} F_{N,j} e^{\beta(\mu N - U_{N,j})}}{\sum_{N,j} e^{\beta(\mu N - U_{N,j})}}. \tag{5.6}$$

The difference with the previous scheme for the canonical ensemble is that since now we have the particle exchange, it brings three types of moves instead of one (see details in Algorithm 2):

- Displacement, new configuration acceptance probability is $P_{\mathrm{acc}}^{\mathrm{disp}} = \min(1, e^{-\beta[U(\boldsymbol{r}') - U(\boldsymbol{r})]})$, no change.

- Removal, acceptance probability $P_{\mathrm{acc}}^{\mathrm{rem}} = \min(1, \frac{\Lambda^3 N}{V} e^{-\beta[U(N) - U(N-1) + \mu]})$, where $U(N) - U(N-1)$ is the energy change after the particle removal, $\Lambda = \frac{h}{\sqrt{2\pi k_{\mathrm{B}} T}}$ is the de Broglie wavelength.

- Insertion, acceptance probability $P_{\mathrm{acc}}^{\mathrm{ins}} = \min(1, \frac{V}{\Lambda^3 (N+1)} e^{-\beta[U(N+1) - U(N) - \mu]})$, where $U(N+1) - U(N)$ is the energy change after the particle insertion.

Algorithm 2 The Grand Canonical Monte Carlo scheme with the highlighted difference with the NVT ensemble.

1: Choose an arbitrary initial configuration of molecules

2: **for** each move **do**

3:       Select a particle at random (uniformly)

4:       Calculate its energy $U(\boldsymbol{r})$ using Equation (5.3)

5:       Displace the particle $\boldsymbol{r'} = \boldsymbol{r} + \boldsymbol{\Delta}$, $\Delta < \Delta_{\max}$ with probability $\min\left(1, \mathrm{e}^{-\beta[U(\boldsymbol{r'})-U(\boldsymbol{r})]}\right)$

6:       **Remove a particle with probability** $\min\left(1, \frac{\Lambda^3 N}{V}\mathrm{e}^{-\beta[U(N)-U(N-1)+\mu]}\right)$

7:       **Insert a particle with probability** $\min\left(1, \frac{V}{\Lambda^3(N+1)}\mathrm{e}^{-\beta[U(N+1)-U(N)-\mu]}\right)$

8: **end for**

5.2.4 Kinetic Monte Carlo Algorithm

Recently Ustinov and Do proposed to employ the kMC algorithm to simulate VLE of a simple LJ fluid in canonical [154] and grand canonical [164] ensembles, then extended it further to two-site LJ model and quadrupole-quadrupole interactions [165]. The idea behind the algorithm is similar to the conventional algorithm described in the previous section. Let us consider the canonical ensemble with an initial configuration of N particles, volume V and temperature T. During the iterative procedure, we choose a particle among others with statistical weight (event rates in terms of the original kMC scheme) r_i as $\mathrm{e}^{\beta U_i}$, displace it at a uniformly random location within the periodic boundary conditions no matter whether it overlaps any other molecules. The iterative procedure of kMC works in such way:

- Choose an event according to its weight in the energy distribution. This can be done by drawing a random uniform number p, followed by finding the index i of the next event this way: $R_{i-1} \leq pR_{N-1} < R_i$, where R_i is a partial (prefix) sum $R_i = \sum_{j=1}^{i} r_i$

- Update the residence time Δt of this event as $\Delta t = \frac{1}{\sum_{i=1}^{N}} \ln 1/p_i$

Having done the iteration procedure for enough steps M to equilibrate, for given density $\rho = \frac{N}{V}$, one can calculate the average chemical potential using the following expression [154]:

$$\mu = k_{\mathrm{B}}T \ln \left(\Lambda^3/V \right) + k_{\mathrm{B}}T \ln \left(\frac{1}{t} \sum_{i=0}^{M-1} \ln 1/p_i \right), \tag{5.7}$$

where M is the total number of steps, t total residence time, p_i are the drawn pseudorandom numbers. The final kMC scheme for a single thread with the calculation of chemical potential is presented in Algorithm 3.

Algorithm 3 The kMC scheme for the vapor-liquid equilibrium calculation. There are also improvements of the algorithm that mitigate the issue with the numerical overflow in R_i [166] caused by frequent overlaps through calculation of $X_i = \ln R_i$ instead of R_i.

1: Choose an arbitrary initial configuration

2: **for** each move **do**

3:    $p \leftarrow \mathrm{uniform}(0,1)$ // Draw pseudorandom number $\in [0,1)$

4:    $R_i \leftarrow \sum_{j=0}^{i} \mathrm{e}^{\beta U_j}$ // Get partial sums of energy

5:    Find i: $R_{i-1} \leq pR_{N-1} < R_i$ // Find the upper bound

6:    Displace i^{th} particle within cell:

7:    $x_i \leftarrow \mathrm{uniform}(0, L_x)$

8:    $y_i \leftarrow \mathrm{uniform}(0, L_y)$

9:    $z_i \leftarrow \mathrm{uniform}(0, L_z)$

10:    $\Delta t \leftarrow \frac{1}{R_{N-1}} \log(1/p)$ // time change

11:    $t \leftarrow t + \Delta t$ // total time

12:    $E \leftarrow E + R_{N-1}\Delta t$ // average energy multiplied by time

13:    $\mu \leftarrow \mu + \log(1/p)$ // average chemical potential multiplied

14:   // by time

15: **end for**
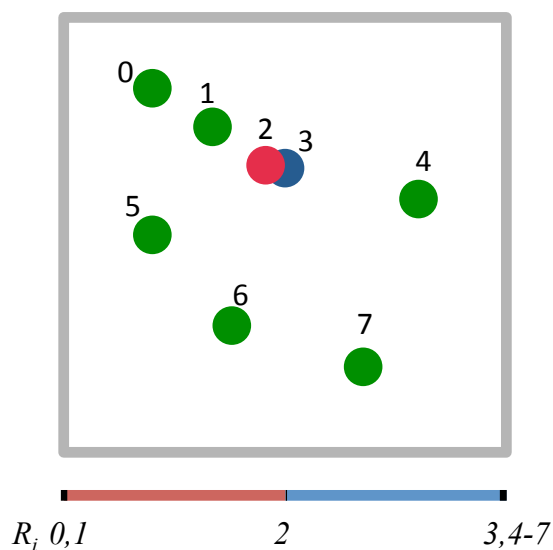
Figure 5.6 The overlap case of two molecules 2 and 3 and their corresponding partial sum of probabilities R_i to be chosen for displacement. As one can see, the probabilities for molecules 2 and 3 are about $\frac{1}{2}$, for the rest it is almost zero.

One of the key differences with the Metropolis et al. algorithm is related to the molecule overlap is treated. Thus, it is worth discussing the overlapping in detail (see Figure 5.6). It can be explained that this overlapping configuration has a short residence time Δt and its contribution to property average will be negligible. Another aspect is that the probability of the fact they would be chosen is very high since the interaction energy is close to infinity. Therefore, the rates r_i, in this case, will be high and the probability that they will be chosen will dominate on the choice of other particles. For example, if one has two overlapping particles, one would have the probability of choosing these two particles the next time approximately equal to $\frac{1}{2}$.

5.2.5 Parallelization Scheme for Graphics Processing Units

One of the improvements can be made here is to parallelize the scheme on one or many graphics processing units (GPUs). This would make viable to simulate large systems as in Chapter 4 it was prohibitively slow to model adsorption for pores larger than 8 nm on a single central processing unit (CPU) core. GPUs are beneficial for

large systems that have number of particles of about $10000 - 50000$, which require simple operations to be performed. It is possible to parallel the algorithm for multiple CPU cores, but it is not going to be as beneficial as an optimization on a single GPU as a GPU has a few thousand cores (as of 2021), although with lower performance. It results in a bigger latency for a single operation but faster wall time overall.

There are already molecular simulation packages with GPU implementations for conventional Monte Carlo schemes [167]. In this section, we are going to apply similar parallelization approaches for the Metropolis algorithm described in the paper. In the kMC algorithm, the overall idea of the parallel implementation remains similar to the serial version, except the energy calculation and Rosenbluth sampling are implemented for execution in multiple threads.

As for the energy calculation, the main idea for parallelization is the same as in the NVT ensemble [167] using the conventional Metropolis et al. algorithm. First, the system is divided into many neighbor lists [152]. They represent a division of the overall box into smaller cells and assigning cell identifiers to each particle in the box. Then, when we need to calculate the energy, not only do we apply the cutoff potential, but also avoid the enumeration over the particles that are far away from each other. This reduces the time complexity significantly as checking neighbor interactions per particle linearly depends on the number of particles. It is worth mentioning that this approach is also applicable for a single thread, although it increases software architecture complexity with little performance benefit. Then, the energy distribution is calculated in parallel, counting only the particles in neighbor cells.

With Rosenbluth sampling, the situation is more complex. As it was mentioned before, to map the uniform pseudorandom number to the one from the energy distribution, one needs to calculate the prefix sums $R_i = \sum_{j=0}^{i} e^{\beta U_j}$. These sums can be calculated efficiently by the algorithm originally proposed by Hillis and Steele [168].

This approach calculates the prefix sums of N elements on $k \leq N$ processors in $O(\frac{N \log N}{k})$ time. Its pseudocode is presented in Algorithm 4.

Algorithm 4 Parallel Rosenbluth sampling scheme

1: **for** $j := 1$ to $\log_2 N$ **do**

2:      **for** each i **parallel do**

3:          **if** $(i+1) \mod 2^j = 0$ **then**

4:              $R_i = R_{i-2^{j-1}} + R_i$ // contribution from other parts

5:          **end if**

6:      **end for**

7: **end for**

8: $p \leftarrow \text{uniform}(0,1)$ // Draw pseudorandom number $\in [0,1)$

9: Find i: $R_{i-1} \leq pR_{N-1} < R_i$ // sample from energy distribution

---

5.3 Results

The first step was to verify the algorithm by reproducing the VLE curve from [154] and [166] (see Figure 5.7). As one can see, the VLE curve has an excellent agreement with the original paper for the same system with argon at $T = 87.3$ K. In addition to the comparison with the original paper, it was also decided to compare the results with a theoretical equation of state for LJ fluid by Johnson et al. [92], with which a quantitative agreement was reached.

The next part was to compare the convergence of chemical potential μ and total fluid-fluid energy U_{ff} by the number of Monte Carlo steps of the same system in NVT ensemble at 10^9 steps. For this reason, two sets of simulations were set up for certain densities covering gas, liquid, and metastable areas to better understand the conditions at which either algorithm performs better. For the classical NVT MC scheme, the Widom test particle insertion method was used to calculate the chemical potential. Instead of looking at the instantaneous value of the chemical potential, we
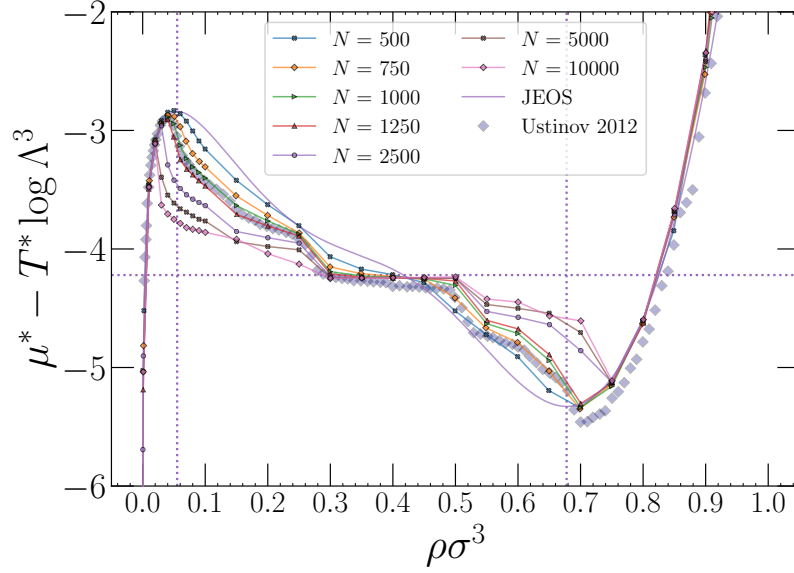
Figure 5.7 Reproduced kMC simulation results for LJ argon at $T = 87.3$ K with interaction parameters described in [154] using our own implementation of the algorithm. The lines with markers correspond to kMC simulations from our code, the N values correspond to the cubic box size matching $\sigma^3 N/V = 1$, Ustinov 2012 is the curve from [154], the purple solid line is the equilibrium curve obtained using Johnson et al. EOS [92], the horizontal dashed line correspond to the equilibrium calculated using the Maxwell rule from the Johnson et al. EOS VLE curve, vertical dashed lines correspond to the spinodal points. The asterisks here correspond to the reduced Lennard-Jones units.
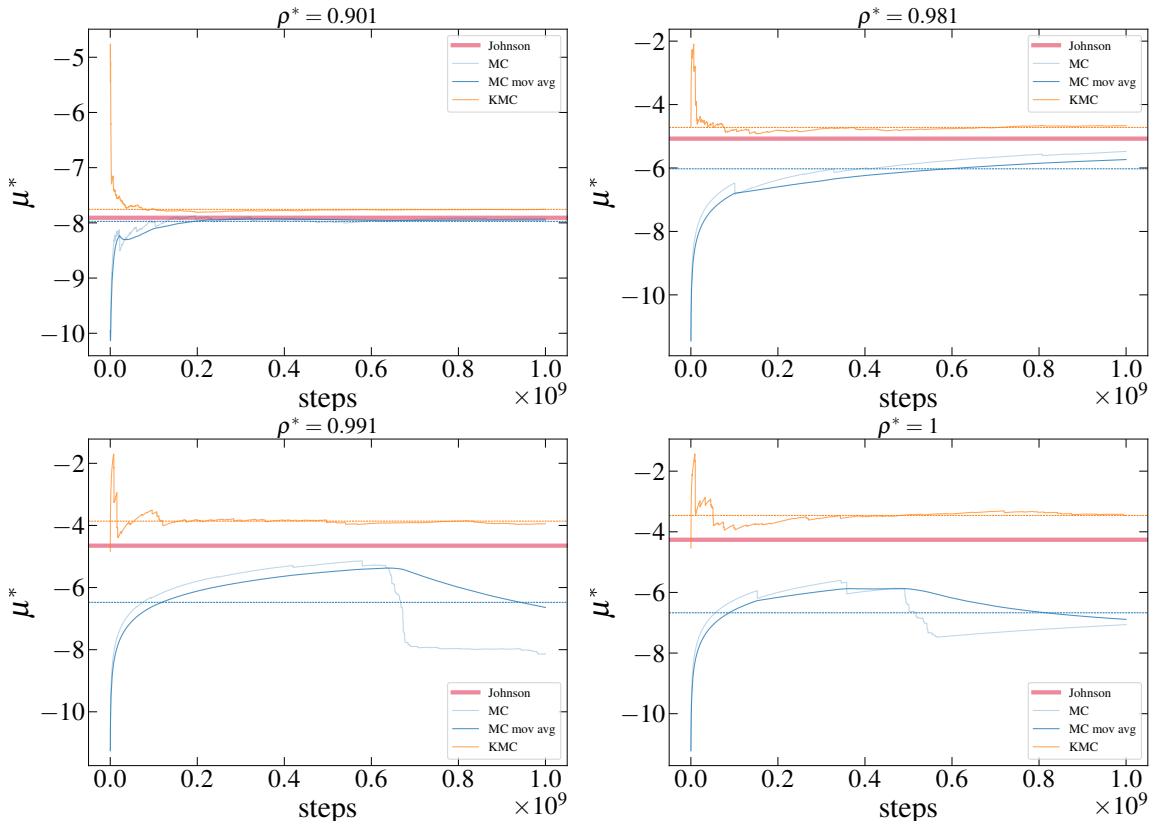
Figure 5.8 Convergence of chemical potential using the classical NVT MC scheme ("MC" for the current immediate value, "MC mov avg" for 30% moving average) and kinetic Monte Carlo scheme with the reference to the value calculated using Johnson equation of state. Four plots correspond to different values of the reduced density of the fluid specified on the title of each. The asterisks here correspond to the reduced Lennard-Jones units.

applied a moving average with a dynamic window taking 30% of the whole interval. In the kMC scheme, chemical potential was calculated using Equation (5.7). The results are presented in Figure 5.7. The total energy in the kMC scheme was weight-averaged by time.

5.4 Discussion

The main observation from the benchmark on chemical potential μ calculation was that kinetic Monte Carlo is more stable and precise in dense regions. Thus, Figure 5.8
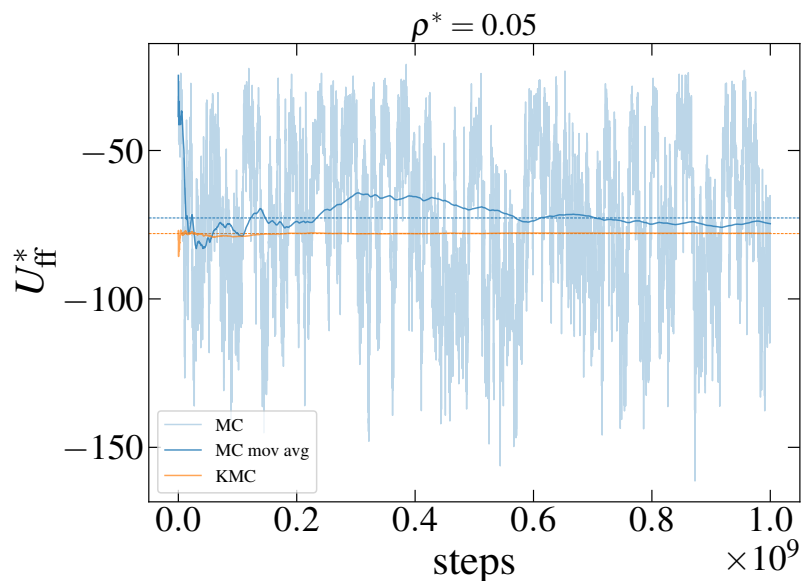
Figure 5.9 Total fluid-fluid energy U_{ff} convergence in a rarefied region at $\rho = 0.05$ using conventional NVT ("MC" for the current immediate value, "MC mov avg" for 30% moving average) and kinetic Monte Carlo schemes.

predicts the value that is closer to Johnson et al. equation of state. In addition to that, the chemical potential value converges at $2 \cdot 10^8$ steps at most, whereas for the classical MC scheme and the Widom test particle insertion method, even dynamic moving average did not completely rectify the situation. In rarefied regions, the convergence was similar for both algorithms, and the chemical potential calculation performed equally well. On the other hand, in rarefied regions, the total energy U_{ff} was calculated using the kinetic Monte Carlo scheme with less deviation than the classical scheme.

However, during testing properties other than chemical potential, a significant drawback of the kinetic Monte Carlo scheme was found. In the classical Monte Carlo scheme, one can calculate the mean value of the property and it can be averaged with a certain interval, e.g., with every 10^5 steps. In the kinetic Monte Carlo scheme, to calculate a property, it should be weighted by time, and excluding the configurations from the averaging is not an option. Thus, rather than computing the properties infrequently using their concise definition with negligible performance loss, one should

either devise a scheme on how to cheaply calculate the property from the current state (the case with the total energy) or sacrifice performance on that.

One of the remaining open problems regarding kMC is to simulate real molecules, such as hydrocarbons and alkanes in particular. The most complex molecule modeled using the scheme so far is N_2 using LJ sites by Transferable Potentials for Phase Equilibria (TraPPE) [169] molecular force field model [170], which today it is a standard for VLE calculations. For this purpose, we propose using the similar approach they did, but for *n*-alkanes and other complex molecules relevant to chemical engineering applications, taking into account bending and dihedral (torsion) potentials described in Section 5.2.1. Our view is that it is a simple united atom model, providing a reasonable balance between the precision and computational cost.

Using kMC, one also comes across a similar problem one has with the Gibbs ensemble scheme. If we start simulating long-chain modules (e.g., decane C_{10}), the configuration sampling would become grossly inefficient. Therefore, a possible solution to the issue is to try to generalize the configurational-bias Monte Carlo [171] to the kMC scheme.

5.5   Conclusion

In this chapter, we implemented the kinetic Monte Carlo algorithm and evaluated its performance. We first compared the VLE curve with the Johnson et al. equation of state with a quantitative agreement. After it, we found out that the algorithm is beneficial over the Widom test particle insertion method in dense regions for the calculation of chemical potential. Although we were limited only by benchmarks of chemical potential and total energy, the close look at the algorithm also showed that thermodynamic properties require explicit calculation at each cycle, which can either bring about complex implementation or performance degradation.

Also, we provided a parallelization scheme for graphics processing units, which would allow us to model large systems. Although the full version with the neighbor list calculation has not been implemented yet, we showed that the parallel version of the algorithm in the time complexity asymptote would have a logarithm multiplier of the number of particles in the neighbor list.

CHAPTER 6

CONCLUSIONS AND OUTLOOK

This dissertation has tackled problems of characterization of porous materials with regard to their pore sizes. It considered various techniques for characterization based on the adsorption data for real materials from microscopic methods to molecular simulations and benchmarked and introduced improvements to existing methods.

In Chapter 1, we made the introduction to the topic, stated the open problems in the characterization of porous materials. Specifically, we highlighted the importance of the techniques for the emerging materials and the absence of a unified generic method for their characterization, as well as gave examples of materials that are challenging to characterize.

In Chapter 2, we were the first who characterized silica colloid crystals (commonly known as opals), using nitrogen adsorption. Also, we revisited and motivated the applicability of Derjaguin-Broekhoff-de Boer and Frenkel-Halsey-Hill theories and obtained the pore-size distribution of it. The resulting pore-size distribution showed the significance of solving the adsorption integral equation rather than a single isotherm search. In addition to that, the distribution revealed information about the pore geometry. The method was also validated by surface modification of the samples.

In Chapter 3, we modeled materials in which the interconnections between the pores are essential. A method to model and calculate the potentials for these interconnections was proposed. The resulting kernels and the calculated pore-size distribution showed a significant deviation of the peak in comparison to a simple spherical model that does not take into account these interconnected windows. Plus, we carefully studied the influence of various periodic boundary conditions as well as the number and size of the windows.

In Chapter 4, thermodynamic properties that affect the pore size other than density were studied. We considered the elastic properties of nitrogen in the channel-like pores inside the Vycor glass. We analyzed the experimental data of the ultrasonic experiment, extracted the longitudinal and shear moduli, and then modeled the pores using the grand canonical Monte Carlo method. The resulting curves showed a near-quantitative agreement with the experiment. Then, the relation of the isothermal elastic bulk modulus to the pore size was shown.

In Chapter 5, we introduced the Kinetic Monte Carlo algorithm for vapor-liquid equilibria calculation. We made benchmarks on the calculation of chemical potential and total energy and showed the cases when the method is especially useful. Then, we highlighted the potential problems with the calculation of various thermodynamic properties and gave examples of the molecules with which the current implementation of the algorithm will struggle. Also, we proposed a scheme for graphical processing unit parallelization, which would allow simulating of large systems.

APPENDIX A

SUPPORTING INFORMATION FOR PORE-SIZE DISTRIBUTION OF SILICA COLLOIDAL CRYSTALS FROM NITROGEN ADSORPTION ISOTHERMS

This appendix contains BET plots, solution isotherms, and SEM images at different scales for Chapter 2. The source code, related documentation, and kernel are available in a Github repository at https://github.com/2xmax/dbdb.
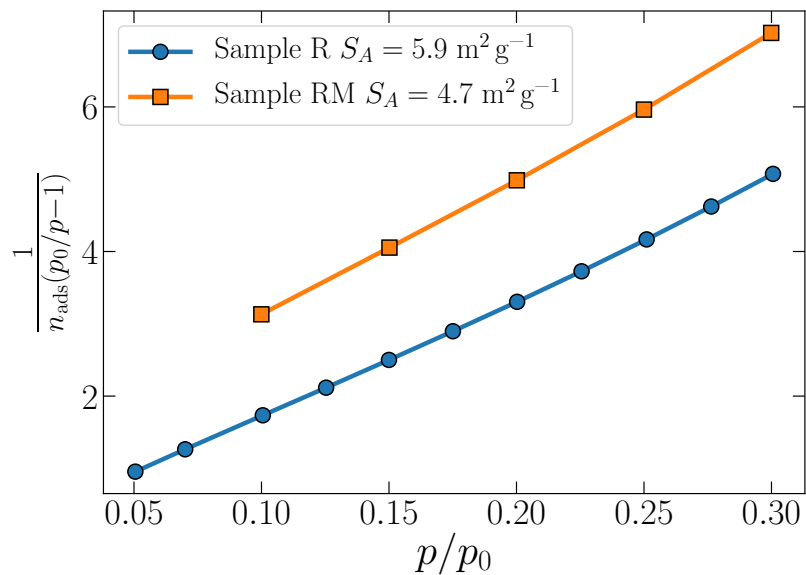
Figure A.1 BET plots for the reference samples.
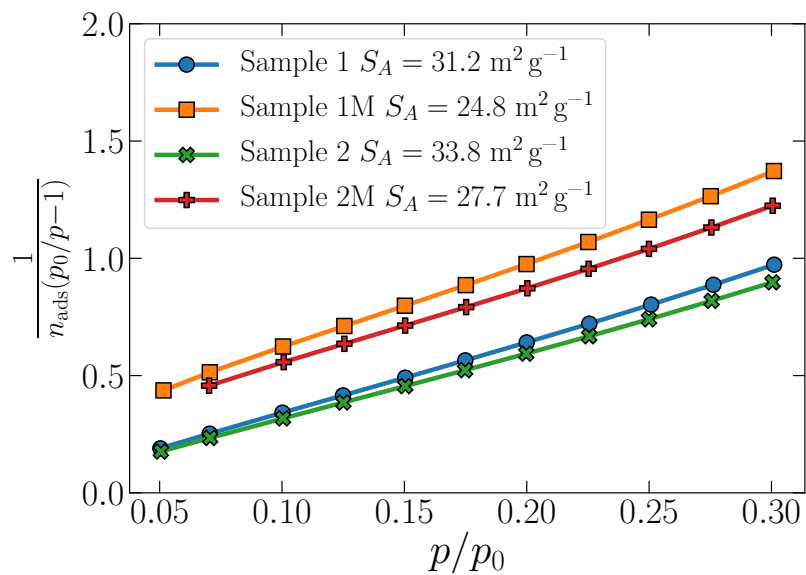
Figure A.2 BET plots for the mesoporous samples.
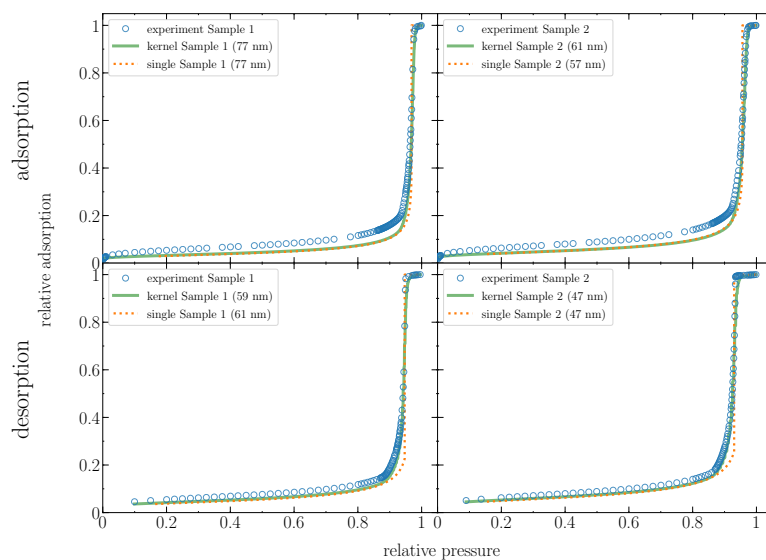
Figure A.3 Solutions for unmodified sample made by the adsorption integral equation and the single mode predictors.
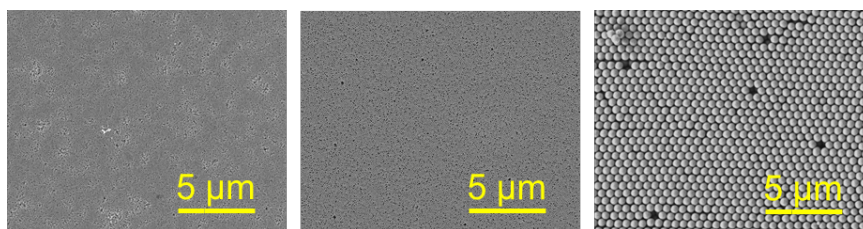
Figure A.4 SEM images for Sample 1, 2 and R.

**SUPPORTING INFORMATION FOR THE EFFECT OF
INTERCONNECTIONS ON GAS ADSORPTION IN MATERIALS
WITH SPHERICAL MESOPORES: A MONTE CARLO SIMULATION
STUDY**

Internal volume calculation

Figure B.1 presents a schematic describing the internal volume calculation for interconnected pores with one window. R and R' are the external and internal radii, δ and δ' are the external and internal opening angles. The location of the pore centers depends on both R and δ. We first derive internal opening angle δ', which is then used for the derivation of the formula for calculation of the internal volume, simply reducing it to a problem of calculation of the volume of the sphere without spherical caps. In this subproblem, there are two cases:
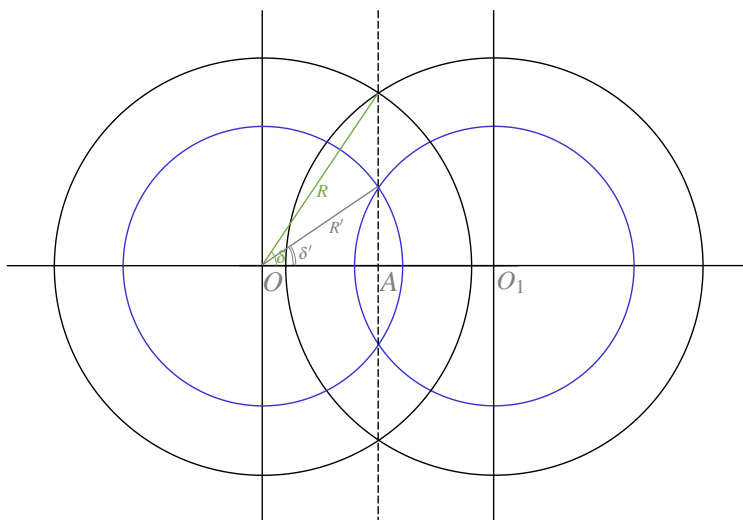
Figure B.1 Geometric notation for internal volume calculation considering one window in the middle. The internal volume is the volume of the union of the spheres of radius R' per periodic cell. The case $R\cos\delta \leq R'$ is drawn here, i.e., when the internal spheres intersect.

1. if $R \cos \delta \leq R'$ (when the internal spheres intersect)

$$OA = R \cos \delta = R' \cos \delta'$$
$$\delta' = \arccos\left(\tfrac{R}{R'} \cos \delta\right)$$

Verification of edge cases:

- $\delta = \frac{\pi}{2} \implies R \cos \delta = 0 \implies \delta' = \frac{\pi}{2}$
- $R \cos \delta = R' \implies \delta' = \arccos(1) = 0$

2. Otherwise, in the case of non-intersecting internal spheres, $\delta' = 0$. The final expression for the internal opening angle is

$$\delta_{\text{int}} = \delta' = \begin{cases} \arccos\left(\tfrac{R}{R'} \cos \delta\right) & \text{if } R \cos \delta \leqslant R' \\ 0 & \text{otherwise} \end{cases} \tag{B.1}$$

To illustrate the property, it is also convenient to introduce critical opening angle $\delta_c = \text{arcccos}\left(\frac{R'}{R}\right)$ to distinguish between these two cases in terms of the opening angle. The plot of the dependence of the internal opening angle versus the external one is shown in Figure B.2. Then, using Equation (B.1), it is easy to calculate the pore internal volume for the given number of windows N_{windows}:

$$h_{\text{cap}} = R'(1 - \cos \delta')$$
$$V_{\text{cap}} = \tfrac{\pi h_{\text{cap}}^2}{3}(3R' - h_{\text{cap}}) \tag{B.2}$$
$$V_{\text{int}} = \tfrac{4}{3}\pi R'^3 - N_{\text{windows}} V_{\text{cap}}$$
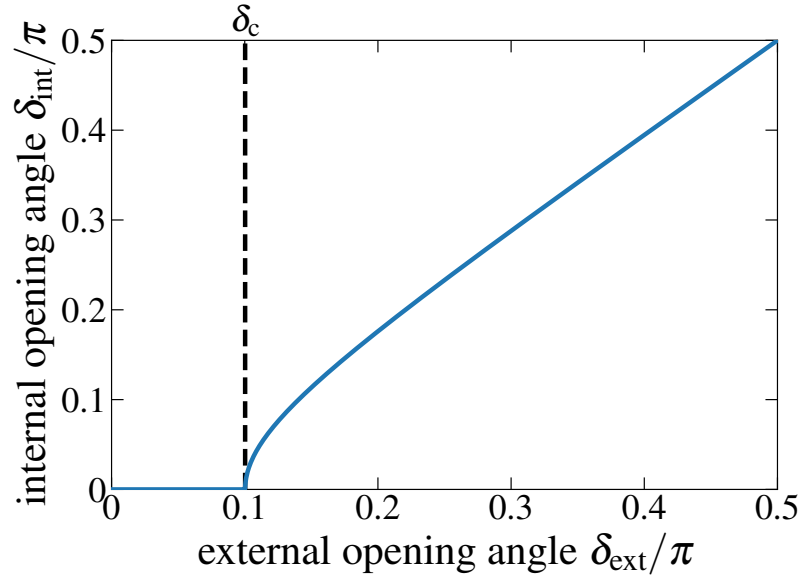
Figure B.2 Internal opening angle starts increasing after the critical opening angle is $\delta_c = \arccos(d_{int}/d_{ext})$.

Choice of number of layers

Another technical aspect is the choice of the proper number of mesh layers as for the cartesian 3D mesh (required for more than two windows) it can be computationally expensive. We performed simulations for meshes with different numbers of layers, and identified a threshold number of layers, after which further increase of layers does not alter the point of capillary condensation as well as the absolute value of density. The result of these runs is presented in Figure B.3.
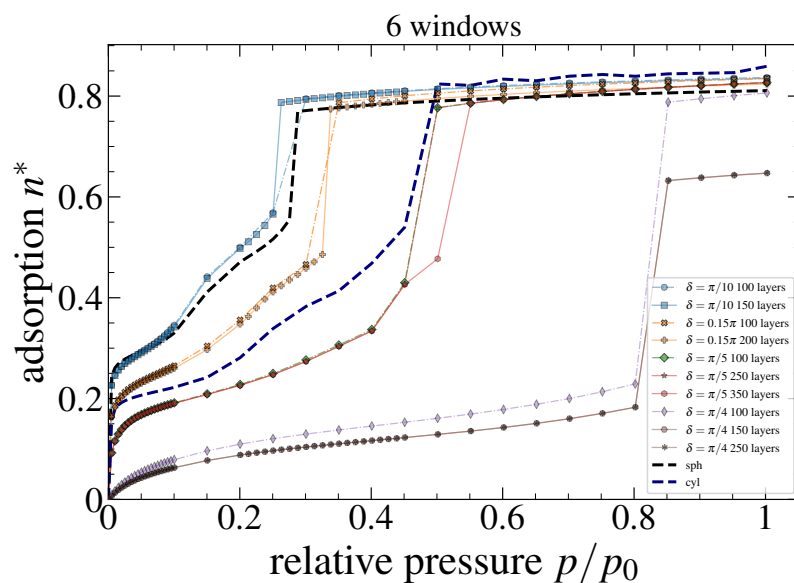
Figure B.3 Verification of a choice of the number of layers for the Cartesian mesh as a substantial increase in the number of layers does not deviate the isotherms much. While the isotherms based on the potentials with 100 layers are noticeably different from the isotherms with a larger number of layers, the isotherms with a larger number of about 200 layers do not differ much.

REFERENCES

[1] Warner KL, Beamish JR. Ultrasonic measurement of the surface area of porous materials. *Journal of Applied Physics.* 1988;63(9):4372–4376.

[2] Thommes M, Kaneko K, Neimark AV, Olivier JP, Rodriguez-Reinoso F, Rouquerol J, Sing KSW. Physisorption of gases, with special reference to the evaluation of surface area and pore size distribution (IUPAC Technical Report). *Pure and Applied Chemistry.* 2015;87(9-10):1051–1069.

[3] Rouquerol J, Rouquerol F, Llewellyn P, Maurin G, Sing KS. *Adsorption by powders and porous solids: principles, methodology and applications.* San Diego, CA, USA: Academic Press. 2013.

[4] Gallego-Gómez F, Morales M, Blanco A, López C. Bare Silica Opals for Real-Time Humidity Sensing. *Advanced Materials Technologies.* 2019;4(2):1800493.

[5] Borchardt L, Nickel W, Casco M, Senkovska I, Bon V, Wallacher D, Grimm N, Krause S, Silvestre-Albero J. Illuminating solid gas storage in confined spaces–methane hydrate formation in porous model carbons. *Physical Chemistry Chemical Physics.* 2016;18(30):20607–20614.

[6] Borchardt L, Oschatz M, Kaskel S. Tailoring porosity in carbon materials for supercapacitor applications. *Materials Horizons.* 2014;1(2):157–168.

[7] Wang G, Yang Y, Lee JH, Abramova V, Fei H, Ruan G, Thomas EL, Tour JM. Nanoporous silicon oxide memory. *Nano Letters.* 2014;14(8):4694–4699.

[8] Ji Y, Yang Y, Lee SK, Ruan G, Kim TW, Fei H, Lee SH, Kim DY, Yoon J, Tour JM. Flexible nanoporous WO3–x nonvolatile memory device. *ACS Nano.* 2016; 10(8):7598–7603.

[9] Lowell S, Shields JE, Thomas MA, Thommes M. *Characterization of porous solids and powders: surface area, pore size and density,* vol. 16. New York, NY, USA: Springer Science & Business Media. 2012.

[10] Gregg SJ, Sing KSW. *Adsorption, Surface Area, and Porosity.* Suffolk, UK: Academic Press, 2nd ed. 1982.

[11] Kruk M, Jaroniec M, Kim TW, Ryoo R. Synthesis and characterization of hexagonally ordered carbon nanopipes. *Chemistry of Materials.* 2003;15(14):2815–2823.

[12] Bentz DP, Garboczi EJ, Quenard DA. Modelling drying shrinkage in reconstructed porous materials: application to porous Vycor glass. *Modelling and Simulation in Materials Science and Engineering.* 1998;6(3):211.

[13] Sing KS. Reporting physisorption data for gas/solid systems with special reference to the determination of surface area and porosity (Recommendations 1984). *Pure and Applied Chemistry.* 1985;57(4):603–619.

[14] Galukhin A, Bolmatenkov D, Emelianova A, Zharov I, Gor GY. Porous Structure of Silica Colloidal Crystals. *Langmuir.* 2019;35(6):2230–2235.

[15] Farrando-Pérez J, López C, Silvestre-Albero J, Gallego-Gómez F. Direct Measurement of Microporosity and Molecular Accessibility in Stöber Spheres by Adsorption Isotherms. *Journal of Physical Chemistry C.* 2018;122(38):22008–22017.

[16] Fan W, Snyder MA, Kumar S, Lee PS, Yoo WC, McCormick AV, Penn RL, Stein A, Tsapatsis M. Hierarchical nanofabrication of microporous crystals with ordered mesoporosity. *Nature Materials.* 2008;7(12):984.

[17] Gelb LD, Gubbins K. Characterization of porous glasses: Simulation models, adsorption isotherms, and the Brunauer- Emmett- Teller analysis method. *Langmuir.* 1998;14(8):2097–2111.

[18] JuneáShin H, et al. Modification of SBA-15 pore connectivity by high-temperature calcination investigated by carbon inverse replication. *Chemical Communications.* 2001;(4):349–350.

[19] Broekhoff JCP, De Boer JH. Studies on pore systems in catalysts: XI. Pore distribution calculations from the adsorption branch of a nitrogen adsorption isotherm in the case of "ink-bottle" type pores. *Journal of Catalysis.* 1968;10(2):153–165.

[20] Roque-Malherbe RM. *Adsorption and diffusion in nanoporous materials.* Boca Raton, FL, USA: CRC press. 2018.

[21] Landers J, Gor GY, Neimark AV. Density Functional Theory Methods for Characterization of Porous Materials. *Colloids and Surfaces, A: Physicochemical and Engineering Aspects.* 2013;437:3–32.

[22] Gor GY, Dobrzanski CD, Emelianova A. Thermodynamic fingerprints of nanoporous materials on the fluids confined in their pores. *Soft Matter And Biomaterials On The Nanoscale: The Wspc Reference On Functional Nanomaterials-Part I (In 4 Volumes).* 2020;20:227.

[23] Maximov MA, Galukhin AV, Gor GY. Pore-Size Distribution of Silica Colloidal Crystals from Nitrogen Adsorption Isotherms. *Langmuir.* 2019; 35(47):14975–14982.

[24] Bohaty AK, Smith JJ, Zharov I. Free-standing silica colloidal nanoporous membranes. *Langmuir.* 2009;25(5):3096–3101.

[25] Galisteo-López JF, Ibisate M, Sapienza R, Froufe-Pérez LS, Blanco Á, López C. Self-assembled photonic structures. *Advanced Materials.* 2011;23(1):30–69.

[26] Zhao Y, Xie Z, Gu H, Zhu C, Gu Z. Bio-inspired variable structural color materials. *Chemical Society Reviews*. 2012;41(8):3297–3317.

[27] Park SH, Xia Y. Macroporous membranes with highly ordered and three-dimensionally interconnected spherical pores. *Advanced Materials*. 1998;10(13):1045–1048.

[28] Wong S, Kitaev V, Ozin GA. Colloidal crystal films: Advances in universality and perfection. *Journal of the American Chemical Society*. 2003; 125(50):15589–15598.

[29] Derjaguin B. A theory of capillary condensation in the pores of sorbents and of other capillary phenomena taking into account the disjoining action of polymolecular liquid films. *Progress in Surface Science*. 1992;40(1-4):46–61.

[30] Derjaguin B. A theory of capillary condensation in the pores of sorbents and of other capillary phenomena taking into account the disjoining action of polymolecular liquid films. *Progress in Surface Science*. 1940;12:181–200.

[31] Quantachrome NOVAtouch® brochure. `https://www.quantachrome.com/pdf_brochures/novatouch_rev1.pdf`. Retrieved on 5/29/2019.

[32] Neimark AV, Ravikovitch PI, Vishnyakov A. Bridging scales from molecular simulations to classical thermodynamics: density functional theory of capillary condensation in nanopores. *Journal of Physics: Condensed Matter*. 2003;15(3):347.

[33] Szombathely M, Bräuer P, Jaroniec M. The solution of adsorption integral equations by means of the regularization method. *Journal of Computational Chemistry*. 1992;13(1):17–32.

[34] Ravikovitch PI. Characterization of nanoporous materials by gas adsorption and density-functional theory. Ph.D. thesis, Yale Univeristy. 1998.

[35] Giesche H. Synthesis of monodispersed silica powders II. Controlled growth reaction and continuous production process. *Journal of the European Ceramic Society*. 1994;14(3):205–214.

[36] Stöber W, Fink A, Bohn E. Controlled growth of monodisperse silica spheres in the micron size range. *Journal of Colloid and Interface Science*. 1968;26(1):62–69.

[37] Frenkel J. *Kinetic theory of liquids*. New York, NY, USA: Dover Publications. 1955.

[38] Gor GY, Neimark AV. Adsorption-induced deformation of mesoporous solids: Macroscopic approach and density functional theory. *Langmuir*. 2011; 27(11):6926–6931.

[39] Neimark AV, Ravikovitch PI. Capillary condensation in MMS and pore structure characterization. *Microporous and Mesoporous Materials*. 2001;44:697–707.

[40] Lawson CL, Hanson RJ. *Solving least squares problems*, vol. 15. Philadelphia, PA, USA: SIAM. 1995.

[41] Golub GH, Heath M, Wahba G. Generalized cross-validation as a method for choosing a good ridge parameter. *Technometrics*. 1979;21(2):215–223.

[42] Dimitrov AS, Nagayama K. Continuous convective assembling of fine particles into two-dimensional arrays on solid surfaces. *Langmuir*. 1996;12(5):1303–1311.

[43] Jiang P, Bertone J, Hwang K, Colvin V. Single-crystal colloidal multilayers of controlled thickness. *Chemistry of Materials*. 1999;11(8):2132–2140.

[44] Köhler J, Kirkland J. Improved silica-based column packings for high-performance liquid chromatography. *Journal of Chromatography A*. 1987;385:125–150.

[45] Van Le T, Ross EE, Velarde TR, Legg MA, Wirth MJ. Sintered silica colloidal crystals with fully hydroxylated surfaces. *Langmuir*. 2007;23(16):8554–8559.

[46] Jal PK, Patel S, Mishra BK. Chemical modification of silica surface by immobilization of functional groups for extractive concentration of metal ions. *Talanta*. 2004; 62(5):1005–1028.

[47] Gun'Ko V, Vedamuthu M, Henderson G, Blitz J. Mechanism and kinetics of hexamethyldisilazane reaction with a fumed silica surface. *Journal of Colloid and Interface Science*. 2000;228(1):157–170.

[48] Bell IH, Wronski J, Quoilin S, Lemort V. Pure and Pseudo-pure Fluid Thermophysical Property Evaluation and the Open-Source Thermophysical Property Library CoolProp. *Industrial & Engineering Chemistry Research*. 2014;53(6):2498–2508.

[49] Span R, Lemmon EW, Jacobsen RT, Wagner W, Yokozeki A. A reference equation of state for the thermodynamic properties of nitrogen for temperatures from 63.151 to 1000 K and pressures to 2200 MPa. *Journal of Physical and Chemical Reference Data*. 2000;29(6):1361–1433.

[50] Mulero A, Cachadiña I, Parra M. Recommended correlations for the surface tension of common fluids. *Journal of Physical and Chemical Reference Data*. 2012; 41(4):043105.

[51] Brunauer S, Emmett PH, Teller E. Adsorption of gases in multimolecular layers. *Journal of the American Chemical Society*. 1938;60(2):309–319.

[52] Rasmussen CJ, Vishnyakov A, Thommes M, Smarsly BM, Kleitz F, Neimark AV. Cavitation in metastable liquid nitrogen confined to nanoscale pores. *Langmuir*. 2010;26(12):10147–10157.

[53] Thommes M. Physical adsorption characterization of nanoporous materials. *Chemie Ingenieur Technik*. 2010;82(7):1059–1073.

[54] Cimino R, Cychosz KA, Thommes M, Neimark AV. Experimental and theoretical studies of scanning adsorption–desorption isotherms. *Colloids and Surfaces, A: Physicochemical and Engineering Aspects*. 2013;437:76–89.

[55] Maximov MA, Molina M, Gor GY. The effect of interconnections on gas adsorption in materials with spherical mesopores: A Monte Carlo simulation study. *The Journal of Chemical Physics*. 2021;154(11):114706.

[56] Tikhonov AN, Arsenin VY. *Solutions of Ill-Posed Problems*. New York, NY, USA: Winston. 1977.

[57] Braida WJ, Pignatello JJ, Lu Y, Ravikovitch PI, Neimark AV, Xing B. Sorption hysteresis of benzene in charcoal particles. *Environmental Science and Technology*. 2003;37(2):409–417.

[58] Yelpo V, Cornette V, Toso JP, López RH. Characterization of Nanostructured Carbon CMK-3 by means of Monte Carlo Simulations. *Carbon*. 2017;121:106–113.

[59] Dantas S, Struckhoff KC, Thommes M, Neimark AV. Pore Size Characterization of Micro-Mesoporous Carbons Using CO_2 Adsorption. *Carbon*. 2021;173:842–848.

[60] Lastoskie C, Gubbins KE, Quirke N. Pore size distribution analysis of microporous carbons: a density functional theory approach. *Journal of Physical Chemistry*. 1993;97(18):4786–4796.

[61] Ravikovitch PI, Neimark AV. Characterization of micro-and mesoporosity in SBA-15 materials from adsorption data by the NLDFT method. *Journal of Physical Chemistry B*. 2001;105(29):6817–6823.

[62] Jagiello J, Jaroniec M. 2D-NLDFT adsorption models for porous oxides with corrugated cylindrical pores. *Journal of Colloid and Interface Science*. 2018;532:588–597.

[63] Jagiełło J, Schwarz JA. Local exact and approximate solutions of the adsorption integral equation with a kernel of a Langmuir-like isotherm: Determination of adsorption energy distribution. *Journal of Colloid and Interface Science*. 1991; 146(2):415–424.

[64] Ravikovitch PI, Vishnyakov A, Neimark AV, Ribeiro Carrott MML, Russo PA, Carrott PJ. Characterization of micro-mesoporous materials from nitrogen and toluene adsorption: experiment and modeling. *Langmuir*. 2006;22(2):513–516.

[65] Zhao D, Feng J, Huo Q, Melosh N, Fredrickson GH, Chmelka BF, Stucky GD. Triblock Copolymer Syntheses of Mesoporous Silica with Periodic 50 to 300 Angstrom Pores. *Science*. 1998;279(5350):548–552.

[66] Ravikovitch PI, Neimark AV. Density functional theory of adsorption in spherical cavities and pore size characterization of templated nanoporous silicas with cubic and three-dimensional hexagonal structures. *Langmuir*. 2002; 18(5):1550–1560.

[67] Vu A, Li X, Phillips J, Han A, Smyrl WH, Buhlmann P, Stein A. Three-dimensionally ordered mesoporous (3DOm) carbon materials as electrodes for electrochemical double-layer capacitors with ionic liquid electrolytes. *Chemistry of Materials*. 2013;25(21):4137–4148.

[68] Wang Z, Dornath P, Chang CC, Chen H, Fan W. Confined synthesis of three-dimensionally ordered mesoporous-imprinted zeolites with tunable morphology and Si/Al ratio. *Microporous and Mesoporous Materials*. 2013;181:8–16.

[69] Cychosz KA, Guo X, Fan W, Cimino R, Gor GY, Tsapatsis M, Neimark AV, Thommes M. Characterization of the pore structure of three-dimensionally ordered mesoporous carbons using high resolution gas sorption. *Langmuir*. 2012; 28(34):12647–12654.

[70] Gor GY, Thommes M, Cychosz KA, Neimark AV. Quenched solid density functional theory method for characterization of mesoporous carbons by nitrogen adsorption. *Carbon*. 2012;50(4):1583–1590.

[71] Zhdanov V. Application of percolation theory to describing kinetic processes in porous solids. *Advances in Catalysis*. 1993;39:1–50.

[72] Cordero S, Kornhauser I, Domínguez A, Felipe C, Esparza JM, Rojas F, López RH, Vidales AM, Riccardo JL, Zgrablich G. Site-Bond Network Modeling of Disordered Porous Media. *Particle & Particle Systems Characterization: Measurement and Description of Particle Properties and Behavior in Powders and Other Disperse Systems*. 2004;21(2):101–116.

[73] Thommes M, Cychosz KA. Physical adsorption characterization of nanoporous materials: progress and challenges. *Adsorption*. 2014;20(2-3):233–250.

[74] Gor GY, Rasmussen CJ, Neimark AV. Capillary condensation hysteresis in overlapping spherical pores: a Monte Carlo simulation study. *Langmuir*. 2012; 28(33):12100–12107.

[75] Desouza A, Monson PA. Modeling fluids confined in three-dimensionally ordered mesoporous carbons. *Adsorption*. 2021;27:DOI: 10.1007/s10450–020–00285–6.

[76] Gor GY, Siderius DW, Rasmussen CJ, Krekelberg WP, Shen VK, Bernstein N. Relation Between Pore Size and the Compressibility of a Confined Fluid. *Journal of Chemical Physics*. 2015;143:194506.

[77] Dobrzanski CD, Maximov MA, Gor GY. Effect of pore geometry on the compressibility of a confined simple fluid. *Journal of Chemical Physics*. 2018;148(5):054503.

[78] Maximov MA, Gor GY. Molecular Simulations Shed Light on Potential Uses of Ultrasound in Nitrogen Adsorption Experiments. *Langmuir*. 2018; 34(51):15650–15657.

[79] Gommes CJ, Friedrich H, Wolters M, Jongh PEd, Jong KPd. Quantitative characterization of pore corrugation in ordered mesoporous materials using image analysis of electron tomograms. *Chemistry of Materials*. 2009; 21(7):1311–1317.

[80] Gommes CJ. Adsorption, capillary bridge formation, and cavitation in SBA-15 corrugated mesopores: a Derjaguin–Broekhoff–de Boer analysis. *Langmuir.* 2012;28(11):5101–5115.

[81] Crowell AD, Steele RB. Interaction potentials of simple nonpolar molecules with graphite. *Journal of Chemical Physics.* 1961;34(4):1347–1349.

[82] Steele WA. The physical interaction of gases with crystalline solids: I. Gas-solid energies and properties of isolated adsorbed atoms. *Surface Science.* 1973; 36(1):317–352.

[83] Tjatjopoulos GJ, Feke DL, Mann Jr JA. Molecule-micropore Interaction Potentials. *Journal of Physical Chemistry.* 1988;92(13):4006–4007.

[84] Baksh MSA, Yang RT. Model for spherical cavity radii and potential functions of sorbates in zeolites. *AIChE Journal.* 1991;37(6):923–930.

[85] Siderius DW, Gelb LD. Extension of the Steele 10-4-3 potential for adsorption calculations in cylindrical, spherical, and other pore geometries. *Journal of Chemical Physics.* 2011;135(8):084703.

[86] Simaioforidou A, Kostas V, Karakassides MA, Louloudi M. Surface chemical modification of macroporous and mesoporous carbon materials: Effect on their textural and catalytic properties. *Microporous and Mesoporous Materials.* 2019;279:334–344.

[87] Kolesnikov AL, Budkov YA, Gor GY. Density Functional Theory Model for Adsorption-Induced Deformation of Mesoporous Materials with Nonconvex Pore Geometry. *Journal of Physical Chemistry C.* 2020;124(37):20046–20054.

[88] Hofmann T, Wallacher D, Perlich J, Koyiloth Vayalil S, Huber P. Formation of periodically arranged nanobubbles in mesopores: capillary bridge formation and cavitation during sorption and solidification in an hierarchical porous SBA-15 matrix. *Langmuir.* 2016;32(12):2928–2936.

[89] Kolesnikov AL, Budkov YA, Gor GY. Adsorption-induced deformation of mesoporous materials with corrugated cylindrical pores. *Journal of Chemical Physics.* 2020; 153(19):194703.

[90] Norman GE, Filinov VS. Investigations of phase transitions by a Monte-Carlo method. *High Temperature.* 1969;7(2):216.

[91] Rasmussen CJ. Molecular simulation of simple fluids and polymers in nanoconfinement. Ph.D. thesis, Rutgers The State University of New Jersey-New Brunswick. 2012.

[92] Johnson JK, Zollweg JA, Gubbins KE. The Lennard-Jones equation of state revisited. *Molecular Physics.* 1993;78(3):591–618.

[93] Vishnyakov A, Neimark AV. Studies of Liquid- Vapor Equilibria, Criticality, and Spinodal Transitions in Nanopores by the Gauge Cell Monte Carlo Simulation Method. *Journal of Physical Chemistry B.* 2001;105(29):7009–7020.

[94] Heinbuch U, Fischer J. Liquid argon in a cylindrical carbon pore: molecular dynamics and Born-Green-Yvon results. *Chemical Physics Letters.* 1987;135(6):587–590.

[95] Gor GY. Adsorption Stress Changes the Elasticity of Liquid Argon Confined in a Nanopore. *Langmuir.* 2014;30(45):13564–13569.

[96] Corrente NJ, Dobrzanski CD, Gor GY. Compressibility of Supercritical Methane in Nanopores: A Molecular Simulation Study. *Energy & Fuels.* 2020; 34(2):1506–1513.

[97] Allen MP, Tildesley DJ. *Computer Simulation of Liquids.* New York, NY, USA: Clarendon Press. 1989.

[98] Wilhelm E. Pressure dependence of the isothermal compressibility and a modified form of the Tait equation. *Journal of Chemical Physics.* 1975;63(8):3379–3381.

[99] Gor GY, Siderius DW, Shen VK, Bernstein N. Modulus–Pressure Equation for Confined Fluids. *Journal of Chemical Physics.* 2016;145(16):164505.

[100] Monson PA. Understanding adsorption/desorption hysteresis for fluids in mesoporous materials using simple molecular models and classical density functional theory. *Microporous and Mesoporous Materials.* 2012;160:47–66.

[101] Forte E, Haslam AJ, Jackson G, Müller EA. Effective coarse-grained solid–fluid potentials and their application to model adsorption of fluids on heterogeneous surfaces. *Physical Chemistry Chemical Physics.* 2014;16(36):19165–19180.

[102] Shi K, Santiso EE, Gubbins KE. Bottom-Up Approach to the Coarse-Grained Surface Model: Effective Solid–Fluid Potentials for Adsorption on Heterogeneous Surfaces. *Langmuir.* 2019;35(17):5975–5986.

[103] Mavko G, Mukerji T, Dvorkin J. *The rock physics handbook.* Cambridge, UK: Cambridge university press. 2020.

[104] Page JH, Liu J, Abeles B, Deckman HW, Weitz DA. Pore-space correlations in capillary condensation in Vycor. *Physical Review Letters.* 1993;71(8):1216.

[105] Page JH, Liu J, Abeles B, Herbolzheimer E, Deckman HW, Weitz DA. Adsorption and desorption of a wetting fluid in Vycor studied by acoustic and optical techniques. *Physical Review E.* 1995;52(3):2763.

[106] Schappert K, Pelster R. Elastic properties and freezing of argon confined in mesoporous glass. *Physical Review B.* 2008;78(17):174108.

[107] Schappert K, Pelster R. Elastic properties of liquid and solid argon in nanopores. *Journal of Physics: Condensed Matter.* 2013;25(41):415302.

[108] Schappert K, Pelster R. Influence of the Laplace pressure on the elasticity of argon in nanopores. *Europhysics Letters*. 2014;105(5):56001.

[109] Schappert K, Pelster R. Temperature Dependence of the Longitudinal Modulus of Liquid Argon in Nanopores. *Journal of Physical Chemistry C*. 2018; 122(10):5537–5544.

[110] Gassmann F. Über die Elastizität poröser Medien. *Vierteljahrsschriften Naturforschende Gesellschaft Zürich*. 1951;96:1–23.

[111] Bourbie T, Coussy O, Zinszner B. *Acoustics of porous media*. Paris, France: Gulf Publishing Company. 1987.

[112] Horoshenkov KV. A review of acoustical methods for porous material characterisation. *International Journal of Acoustics and Vibrations*. 2017;22:92–103.

[113] Warner KL. Sound Velocity and Attenuation Measurements at Low Temperatures in Fluid Filled Porous Media. Master's thesis, University of Delaware. 1986.

[114] Dobrzanski CD, Gurevich B, Gor GY. Elastic properties of confined fluids from molecular modeling to ultrasonic experiments on porous solids. *Applied Physics Reviews*. 2021;8(2):021317.

[115] Biot MA. Theory of propagation of elastic waves in a fluid-saturated porous solid. I. Low-frequency range. *Journal of the Acoustical Society of America*. 1956; 28(2):168–178.

[116] Berryman JG. Origin of Gassmann's equations. *Geophysics*. 1999;64(5):1627–1629.

[117] Lemmon EW, Jacobsen RT. Viscosity and Thermal Conductivity Equations for Nitrogen, Oxygen, Argon, and Air. *International Journal of Thermophysics*. 2004;25(1):21–69.

[118] Gor GY, Gurevich B. Gassmann Theory Applies to Nanoporous Media. *Geophysical Research Letters*. 2018;45(1):146–155.

[119] Kuster GT, Toksöz MN. Velocity and attenuation of seismic waves in two-phase media: Part I. Theoretical formulations. *Geophysics*. 1974;39:587–606.

[120] Huber P. Soft matter in hard confinement: phase transition thermodynamics, structure, texture, diffusion and flow in nanoporous media (topical review). *Journal of Physics: Condensed Matter*. 2015;27:103102.

[121] Gubbins KE, Liu YC, Moore JD, Palmer JC. The role of molecular modeling in confined systems: impact and prospects. *Physical Chemistry Chemical Physics*. 2011;13(1):58–85.

[122] Landau LD, Lifshitz EM. *Statistical Physics, vol. 5*, vol. 30. New York, NY, USA: Pergamon. 1980.

[123] Thommes M, Smarsly B, Groenewolt M, Ravikovitch PI, Neimark AV. Adsorption hysteresis of nitrogen and argon in pore networks and characterization of novel micro-and mesoporous silicas. *Langmuir.* 2006;22(2):756–764.

[124] Gor GY. Bulk Modulus of Not-So-Bulk Fluid. *Poromechanics VI.* 2017;pp. 465–472.

[125] Thorne KS, Blandford RD. *Modern classical physics: optics, fluids, plasmas, elasticity, relativity, and statistical physics.* Princeton, NJ, USA: Princeton University Press. 2017.

[126] Granick S. Motions and relaxations of confined liquids. *Science.* 1991; 253(5026):1374–1379.

[127] Schappert K, Reiplinger N, Pelster R. Correlation between the Sorption-Induced Deformation of Nanoporous Glass and the Continuous Freezing of Adsorbed Argon. *Langmuir.* 2016;32(31):7741–7746.

[128] Schappert K, Naydenov V, Pelster R. Oxygen in Nanopores: A Study on the Elastic Behavior of Its Solid Phases. *Journal of Physical Chemistry C.* 2016; 120(45):25990–25995.

[129] Molz E, Wong APY, Chan MHW, Beamish JR. Freezing and melting of fluids in porous glasses. *Physical Review B.* 1993;48(9):5741.

[130] Borisov BF, Gartvik AV, Nikulin FV, Charnaya EV. Acoustic study of melting and freezing of mercury nanoparticles in porous glasses. *Acoustical Physics.* 2006; 52(2):138–143.

[131] Charnaya EV. Acoustic studies of phase transitions in crystals and nanocomposites. *Acoustical Physics.* 2008;54(6):802–813.

[132] Borisov BF, Gartvik AV, Gorchakov AG, Charnaya EV. Acoustic studies of melting and crystallization of nanostructured decane. *Physics of the Solid State.* 2009; 51(4):823–828.

[133] Schappert K, Pelster R. Freezing behavior of argon layers confined in mesopores. *Physical Review B.* 2011;83(18):184110.

[134] Schappert K, Pelster R. Continuous freezing of argon in completely filled mesopores. *Physical Review Letters.* 2013;110(13):135701.

[135] Ravikovitch PI, Vishnyakov A, Russo R, Neimark AV. Unified approach to pore size characterization of microporous carbonaceous materials from N_2, Ar, and CO_2 adsorption isotherms. *Langmuir.* 2000;16(5):2311–2320.

[136] Macdonald JR. Some simple isothermal equations of state. *Reviews of Modern Physics.* 1966;38(4):669.

[137] Wunderlich B. *Macromolecular Physics - Crystal Melting.* New York, NY, USA: Academic Press. 1980.

[138] Landry MR. Thermoporometry by differential scanning calorimetry: experimental considerations and applications. *Thermochimica Acta*. 2005;433(1):27–50.

[139] Seaton NA, Walton JPRB, Quirke N. A new analysis method for the determination of the pore size distribution of porous carbons from nitrogen adsorption measurements. *Carbon*. 1989;27(6):853–861.

[140] Jagiello J. Stable numerical solution of the adsorption integral equation using splines. *Langmuir*. 1994;10(8):2778–2785.

[141] Balzer C, Cimino RT, Gor GY, Neimark AV, Reichenauer G. Deformation of microporous carbons during N_2, Ar, and CO_2 adsorption: Insight from the density functional theory. *Langmuir*. 2016;32(32):8265–8274.

[142] Siderius DW, Mahynski NA, Shen VK. Relationship between pore-size distribution and flexibility of adsorbent materials: statistical mechanics and future material characterization techniques. *Adsorption*. 2017;23(4):593–602.

[143] Stewart RB, Jacobsen RT. Thermodynamic properties of argon from the triple point to 1200 K with pressures to 1000 MPa. *Journal of Physical and Chemical Reference Data*. 1989;18(2):639–798.

[144] Potoff JJ, Siepmann JI. Vapor–liquid equilibria of mixtures containing alkanes, carbon dioxide, and nitrogen. *AIChE Journal*. 2001;47(7):1676–1682.

[145] Panagiotopoulos AZ. Monte Carlo methods for phase equilibria of fluids. *Journal of Physics: Condensed Matter*. 2000;12(3):R25.

[146] Fredenslund A, Gmehling J, Rasmussen P. Chapter 1 - Introduction. *Vapor-liquid Equilibria Using UNIFAC*. 1977;pp. 1–5.

[147] Abbott MM. *Cubic Equations of State: An Interpretive Review*. Washington, DC, USA. 1979.

[148] Economou IG, Tsonopoulos C. Associating models and mixing rules in equations of state for water/hydrocarbon mixtures. *Chemical Engineering Science*. 1997; 52(4):511–525.

[149] Chapman W, Gubbins K, Jackson G, Radosz M. SAFT: Equation-of-state solution model for associating fluids. *Fluid Phase Equilibria*. 1989;52:31–38.

[150] Gross J, Sadowski G. Application of the Perturbed-Chain SAFT Equation of State to Associating Systems. *Industrial & Engineering Chemistry Research*. 2002; 41(22):5510–5515.

[151] de Pablo JJ, Escobedo FA. Molecular simulations in chemical engineering: Present and future. *AIChE Journal*. 2004;48(12):2716–2721.

[152] Frenkel D, Smit B. *Understanding Molecular Simulation*. Orlando, FL, USA: Academic Press, Inc., 2nd ed. 2001.

[153] Palmer JC, Debenedetti PG. Recent advances in molecular simulation: a chemical engineering perspective. *AIChE Journal*. 2015;61(2):370–383.

[154] Ustinov EA, Do DD. Application of kinetic Monte Carlo method to equilibrium systems: Vapour–liquid equilibria. *Journal of Colloid and Interface Science*. 2012;366(1):216–223.

[155] Widom B. Some topics in the theory of fluids. *Journal of Chemical Physics*. 1963; 39(11):2808–2812.

[156] Nguyen VT, Fan C, Do D, Nicholson D, Ustinov E, et al. Development of kinetic Monte Carlo and Bin-Monte Carlo schemes for simulation of mixtures–vapor–liquid equilibria & adsorption. *Chemical Engineering Science*. 2013;102:220–226.

[157] Jansen A. *An Introduction to Kinetic Monte Carlo Simulations of Surface Reactions*. Lecture Notes in Physics 856. Springer-Verlag Berlin Heidelberg, 1st ed. 2012.

[158] Battaile CC. The kinetic Monte Carlo method: Foundation, implementation, and application. *Computer Methods in Applied Mechanics and Engineering*. 2008; 197(41-42):3386–3398.

[159] Tavarone R, Charbonneau P, Stark H. Kinetic Monte Carlo simulations for birefringence relaxation of photo-switchable molecules on a surface. *Journal of Chemical Physics*. 2016;144(10):104703.

[160] Erban R, Chapman J, Maini P. A practical guide to stochastic simulations of reaction-diffusion processes. *ArXiv e-prints*. 2007;p. 0704.1908.

[161] Awang M, Mohammadpour E, Muhammad I. *Finite Element Modeling of Nanotube Structures: Linear and Non-linear Models*. Engineering Materials. Springer Cham Heidelberg New York Dordrecht London. 2015.

[162] Nakano A, Vashishta P, Kalia RK. Parallel multiple-time-step molecular dynamics with three-body interaction. *Computer Physics Communications*. 1993; 77(3):303–312.

[163] Metropolis N, Rosenbluth AW, Rosenbluth MN, Teller AH, Teller E. Equation of State Calculations by Fast Computing Machines. *Journal of Chemical Physics*. 1953;21(6):1087–1092.

[164] Ustinov EA, Do D. Simulation of gas adsorption on a surface and in slit pores with grand canonical and canonical kinetic Monte Carlo methods. *Physical Chemistry Chemical Physics*. 2012;14(31):11112–11118.

[165] Ustinov E, Gorbunov V, Akimenko S. From Simulation to Thermodynamics of Orientational Transitions in Molecular Layers: Nitrogen Contact Layer on Solids. *Journal of Physical Chemistry C*. 2018;122(5):2897–2908.

[166] Fan C, Do D, Nicholson D, Ustinov E. Chemical potential, Helmholtz free energy and entropy of argon with kinetic Monte Carlo simulation. *Molecular Physics*. 2014;112(1):60–73.

[167] Nejahi Y, Barhaghi MS, Mick J, Jackman B, Rushaidat K, Li Y, Schwiebert L, Potoff J. GOMC: GPU Optimized Monte Carlo for the simulation of phase equilibria and physical properties of complex fluids. *SoftwareX*. 2019;9:20–27.

[168] Hillis WD, Steele Jr GL. Data parallel algorithms. *Communications of the ACM*. 1986;29(12):1170–1183.

[169] Martin MG, Siepmann JI. Transferable Potentials for Phase Equilibria. 1. United-Atom Description of n-Alkanes. *Journal of Physical Chemistry B*. 1998; 102(14):2569–2577.

[170] Fan C, Do D, Nicholson D, Ustinov E. A novel application of kinetic Monte Carlo method in the description of N_2 vapour–liquid equilibria and adsorption. *Chemical Engineering Science*. 2013;90:161–169.

[171] Siepmann JI, Karaborni S, Smit B. Simulating the critical behaviour of complex fluids. *Nature*. 1993;365(6444):330.